Measurement of branching fractions, isospin and *CP*-violating asymmetries for exclusive $\boldsymbol{b \to d\gamma}$ modes

Nanae Taniguchi

September, 2008

Department of Physics, Graduate School of Science
Kyoto University

Dissertation Committee:

Noboru Sasao
Tsuyoshi Nakaya
Tomofumi Nagae
Tetsuya Onogi
Hiroyuki Hata

Abstract

The $b \to d\gamma$ process, which proceeds via a loop diagram in the Standard Model (SM), provides a sensitive probe to search for physics beyond the SM (BSM), since the loop diagram may also be formed by postulated heavy BSM particles. Branching fractions of this process have been used to constrain the ratio of Cabibbo-Kobayashi-Maskawa (CKM) matrix elements $|V_{td}/V_{ts}|$ which is also constrained by recently measured B_s^0-$\overline{B}_s^0$ mixing; a BSM effect may be observed as a deviation of $|V_{td}/V_{ts}|$ from the SM value. An additional contribution from an annihilation diagram may induce direct *CP* asymmetry in $B^+ \to \rho^+\gamma$ and isospin asymmetry between $B \to \rho\gamma$ modes; the latter can be used to constrain the CKM angle ϕ_3.
We report improved measurements of the $B \to \rho\gamma$ and $B \to \omega\gamma$ processes using a sample of $(657 \pm 9) \times 10^6$ B meson pairs accumulated at the $\Upsilon(4S)$ resonance. With a larger data sample and an improved analysis procedure, the results supersede those of our previous publication. The data are produced in e^+e^- annihilation at the KEKB energy-asymmetric (3.5 on 8 GeV) collider and collected with the Belle detector. We reconstruct three signal modes, $B^+ \to \rho^+\gamma$, $B^0 \to \rho^0\gamma$ and $B^0 \to \omega\gamma$, and two control samples, $B^+ \to K^{*+}\gamma$ and $B^0 \to K^{*0}\gamma$. and measure branching fractions $\mathcal{B}(B^+ \to \rho^+\gamma)$, $\mathcal{B}(B^0 \to \rho^0\gamma)$ and $\mathcal{B}(B^0 \to \omega\gamma)$; an isospin asymmetry $\Delta(\rho\gamma)$; and a direct *CP*-violating asymmetry $A_{CP}(B^+ \to \rho^+\gamma)$.

We obtain the results as follows;

$$\begin{aligned}
\mathcal{B}(B^+ \to \rho^+\gamma) &= (0.87\,^{+0.29}_{-0.27}\,^{+0.09}_{-0.11}) \times 10^{-6} \\
\mathcal{B}(B^0 \to \rho^0\gamma) &= (0.78\,^{+0.17}_{-0.16}\,^{+0.09}_{-0.10}) \times 10^{-6} \\
\mathcal{B}(B^0 \to \omega\gamma) &= (0.40\,^{+0.19}_{-0.17} \pm 0.13) \times 10^{-6} \\
\\
\Delta(\rho\gamma) &= -0.48\,^{+0.21}_{-0.19}\,^{+0.08}_{-0.09} \\
A_{CP}(B^+ \to \rho^+\gamma) &= -0.11 \pm 0.32 \pm 0.09
\end{aligned}$$

where the first error term is the statistical error and the second is the systematic error.

In conclusion, we present a new measurement of branching fractions for $B \to \rho\gamma$ and $B \to \omega\gamma$, a measurement of the isospin asymmetry, and the first measurement of the direct *CP*-violating asymmetry for $B^+ \to \rho^+\gamma$. The results are consistent with SM predictions.

The ratios of the branching fractions of the $B \to \rho\gamma/\omega\gamma$ modes to those of the $B \to K^*\gamma$ modes can be related to $|V_{td}/V_{ts}|$. We calculate the ratios and find,

$$\begin{aligned}
\frac{\mathcal{B}(B^0 \to \rho^0\gamma)}{\mathcal{B}(B^0 \to K^{*0}\gamma)} &= 0.0206\,^{+0.0045}_{-0.0043}\,^{+0.0014}_{-0.0016}, \\
\frac{\mathcal{B}(B \to \rho\gamma)}{\mathcal{B}(B \to K^*\gamma)} &= 0.0302\,^{+0.0060}_{-0.0055}\,^{+0.0026}_{-0.0028}, \\
\frac{\mathcal{B}(B \to (\rho,\omega)\gamma)}{\mathcal{B}(B \to K^*\gamma)} &= 0.0284 \pm 0.0050\,^{+0.0027}_{-0.0029},
\end{aligned}$$

where the first and second errors are statistical and systematic, respectively. We extract $|V_{td}/V_{ts}|$ from the ratio of the branching fractions taken from $\frac{\mathcal{B}(B \to (\rho,\omega)\gamma)}{\mathcal{B}(B \to K^*\gamma)} = 0.0284 \pm 0.0050\,^{+0.0027}_{-0.0029}$. The result is $|V_{td}/V_{ts}| = 0.195\,^{+0.020}_{-0.019} \pm 0.015$.

We improve the experimental precision on $|V_{td}/V_{ts}|$ determined from penguin loops, finding good agreement with the value determined from box diagrams.

Acknowledgments

First of all, I would particularly like to thank Prof. Y. Sakai of KEK. However, words can't describe how grateful I am. I could have never finished my thesis without his supervision. I have been deeply impressed by his sincere attitude to physics, experiment and people and encouraged by care and kind thought from his guidance in not so many words. He has kindly made so much time for discussion and listening to my talk.

My deeply appreciation goes to Dr. M. Nakao. I received generous support from him. I have learned a lot of things for analysis and physics. His advice made a breakthrough in difficult situation.

I would like to thank Dr. S. Nishida with whom I worked closely over the years. He taught me everything for Belle analysis, how to write a code, submit a job, use analysis tools and many other things. He also gave me constructive comments and warm encouragement.

I am deeply grateful to the internal referees, Y.J. Kwon, S. Eidelman and A.J. Schwartz, who gave insightful comments and suggestions for this analysis. It was a great pleasure to have the opportunity to discuss with them. I also appreciate T.E. Browder who helped me to complete the journal paper for this analysis and brushed up the paper.

I acknowledge the help and supports of all the members of the DCPV/rare analysis group. I would like to thank people at Tsukuba-hall for their friendship. I also thank Ms. C. Imai of Belle secretary for many help to my KEK life.

I would like to express my gratitude to my supervisor Prof. N. Sasao of Kyoto university, for teaching me pleasure and severeness of physics. Our first conversation was about a classical music. He was a supervisor when I next saw him. My foothold of research had moved to KEK from Kyoto, but I have always felt I was under the wing of him. My heart is filled with gratefulness.

I am thankful to Dr. T. Nomura, Dr. T. Nakaya, Dr. H. Nanjo and Dr. M. Yokoyama of Kyoto university. We could not have so many communication because we have been working for different experiments. However, they gave me some invaluable advice at perfect moment.

I would like to address thanks to the secretary Ms. A. Nakao, Ms. K. Nakagawa, Ms. M. Hiraoka and the other secretaries of Kyoto university for taking care of every official/private businesses, while I was not in Kyoto.

I am deeply thank to K.Takezawa, T. Shirai, K. Hiraide and J. Kubota who have worked hard together. Their kindness and friendship motivated me for the research. I also thank all the members of High Energy Group of Kyoto University.

Special thanks to M. Hasegawa, K. Sakashita, T. Sumida and H. Watanabe who are indispensable people for my Tsukuba life and enriched my life at Tsukuba. They often calm down, encourage and give me many advice.

I would like to say '*Danke*' to wonderful fellows also friends at Kyoto university, J. Zenihiro, M. Tanabe, Y. Izumi and Y. Kobayashi, for their warm and constant friendship which is a treasure through my life.

FINALLY, I would like to express hearty thanks to my family, my grandparents, Masao and Tatsuko Watanabe, parents, Jiro and Yanagi Taniguchi, and Kaori and Tomohiro for their endless support. We always share joy and sorrow. I wish you are delighted with the attainment together.

Contents

List of Figures

List of Tables

1 Introduction

In this thesis, we present the study of the radiative penguin $B^+ \to \rho^+\gamma$, $B^0 \to \rho^0\gamma$ and $B^0 \to \omega\gamma$ decays using the data recorded by KEKB and Belle detector.

The interest of the nature science covers from the ultimate elements of matter to the universe. Scientists have made every effort to establish the fundamental law for the origin of the nature. The goal of the elementary physics is to understand the origin of the matter and the interaction between them, and the reason why the universe is brought into existence as it is. At present, quarks and leptons are considered as the elemental particle which consist in the matter, and the gauge boson are considered as the mediator between quarks and leptons. The Standard Model describes the interactions between these particles very well. Almost all the experimental phenomena could have been predicted by the Standard Model. In the Standard Model, one of the issue not solved is the *CP* violation mechanism. A *CP* violating phenomena were observed in a *K*-meson system. In 1973, Kobayashi and Maskawa proposed a model for *CP* violation mechanism within the Standard Model framework as an irreducible phase in the quark mixing matrix, called as the Cabibbo-Kobayashi-Maskawa matrix. Although even charm quark were not discovered yet, this model predicts the existence of the quarks of three generation. The discoveries of the *b* and *t* quarks suggested the quark mixing model was the origin of *CP* violation.

In the Standard Model, Flavor changing neutral currents, such as $b \to (s, d)$ transition, are forbidden at the tree level. As the lowest order of diagram, these transitions are possible proceeding with a loop. Instead of a virtual *W*, a charged Higgs or non-Standard Model particles can mediate the loop. It is the sensitive probe to new physics. Experimentally, for example, $b \to s$ and $b \to d$ transitions with real photon are observed in measurements for $B \to K^*\gamma$ and $B \to \rho\gamma, \omega\gamma$, respectively by *B*-factories.

In the following sections, first, we introduce the theoretical framework and physics motivation. The penguin decays and a detail for radiative penguin decays are described in the Standard Model framework. We also consider the physics beyond the Standard Model as a SUSY model. In Section 3, we describe the Experimental Apparatus of the KEK *B* factory. The KEKB accelerator and each part for the Belle detector are presented in this section. We describe Signal Reconstruction and Background Suppression in Section 4. The selection criteria and reconstruction for signal are described. We also mention background sources and how to suppress each background. In Section 5, we describe Signal Extraction which is performed by unbinned extended maximum likelihood fit and Probability Density Functions (PDFs) for each component using the fit. We present how to determine and calibrate the PDF for signal modes. In Section 6, the results are presented. We measure the branching fraction of $B^+ \to \rho^+\gamma$, $B^0 \to \rho^0\gamma$ and $B^0 \to \omega\gamma$ decays. Using the results of the branching fractions, we calculate the combined branching fraction for extraction of $|V_{td}/V_{ts}|$. We also measure the direct *CP*-violating and isospin asymmetries.

Finally, we discuss about the results and summarize. $|V_{td}/V_{ts}|$ is extracted using the results of the branching fractions. We compare the experimental results and theoretical calculations.

2 Theoretical Framework and Physics Motivation

2.1 The CKM matrix

In the Standard Model, the couplings of the quarks in the charged current weak interactions are given by a 3×3 complex unitary matrix, called as the Cabibbo-Kobayashi-Maskawa (CKM) matrix [1],

$$V_{CKM} = \begin{pmatrix} V_{ud} & V_{us} & V_{ub} \\ V_{cd} & V_{cs} & V_{cb} \\ V_{td} & V_{ts} & V_{tb} \end{pmatrix} \tag{1}$$

The CKM matrix can be described completely by the Euler-type angles and a complex phase. In the Wolfenstein parameterization [2], the CKM matrix is approximated in terms of four real independent parameters (λ, A, ρ, η), which makes clear the hierarchical structure of the elements:

$$V_{CKM} \approx \begin{pmatrix} 1-\frac{1}{2}\lambda^2 & \lambda & A\lambda^3(\rho - i\eta) \\ -\lambda & 1-\frac{1}{2}\lambda^2 & A\lambda^2 \\ A\lambda^3(1-\rho-i\eta) & -A\lambda^2 & 1 \end{pmatrix} + \mathcal{O}(\lambda^4) \tag{2}$$

Since $\lambda = \sin\theta_C$ (θ_C: Cabbibo angle) is small ($\lambda \approx 0.22$), this parameterization shows that the off-diagonal elements are small and the diagonal elements are close to unity. The complex phase, which is responsible for CP violation in the Standard Model, has been assigned to the corner elements in this parameterization.

2.2 Penguin B decays

Flavor changing neutral currents (FCNC) are forbidden at the tree level in the Standard Model. However, loop-induced FCNC (called penguin decays) are possible. For B meson, two penguin transitions are possible, $b \to d$ and $b \to s$, proceeding with a loop where a W and an up-type quark are involved (top quark is dominant). Figure 1 shows the loop diagram for the $b \to t \to (s,d)$ transition. These loop diagrams with combinations of CKM matrix elements give insightful view into the Standard Model. In addition, they are quite sensitive to new physics. In order to conserve energy and momentum, an additional particle has to be emitted in the transition. The particle defines the type of penguin transitions and can be categorized as

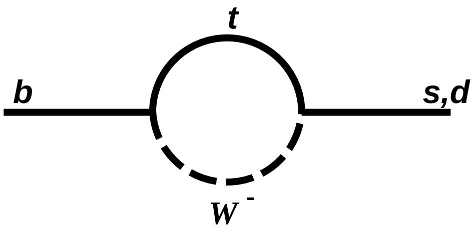

Figure 1: $b \to (s,d)$ loop(penguin) diagram.

- Radiative Penguin (A charged particle emits an external real photon),
- Electroweak Penguin (An emitted virtual photon or Z^0 produces a pair of leptons),
- Vertical (or Annihilation) Penguin (Penguin loop connects the two quarks in the B meson),
- Gluonic Penguin (A gluon is emitted from the penguin loop),

and these diagrams are shown in Figure 2. Examples of radiative penguin decays are the $B \rightarrow K^*\gamma$, $B \rightarrow \rho\gamma$ and $B \rightarrow \omega\gamma$ modes studied in this thesis. Examples of electroweak, annihilation and gluonic penguin decays are $B \rightarrow K^{(*)}l\bar{l}$, $B_{(s,d)} \rightarrow l\bar{l}$ and $B \rightarrow \phi K, K^0\bar{K}^0$, respectively.

Penguin processes are also possible in c and t decays, but these quarks can proceed with the CKM-favored $c \rightarrow s$ and $t \rightarrow b$ transitions. Since the b quark has no kinematically allowed CKM-favored decays, the relative importance of the penguin decays is greater. The mass of the top quark, the main contributor to the loop, is large and the coupling of the b quark to the t quark, $|V_{td}|$, is very close to unity, both of which strengthen the effect of the penguin. The $b \rightarrow (s,d)$ penguin transition is sensitive to $|V_{t(s,d)}|$ which are rather difficult to measure in top decay. Information on $|V_{ts}|$ and $|V_{td}|$ from the penguin decay will complement that from $B_s - \bar{B}_s$ and $B^0 - \bar{B}^0$ mixing. Since the Standard Model loops involve the heaviest known particles (t, W), decay rates for these processes are sensitive to non-Standard Model extensions with heavy charged Higgs or supersymmetric particles. Therefore, measurements of loop processes constitute the most sensitive low energy probes for such extensions to the Standard Modes.

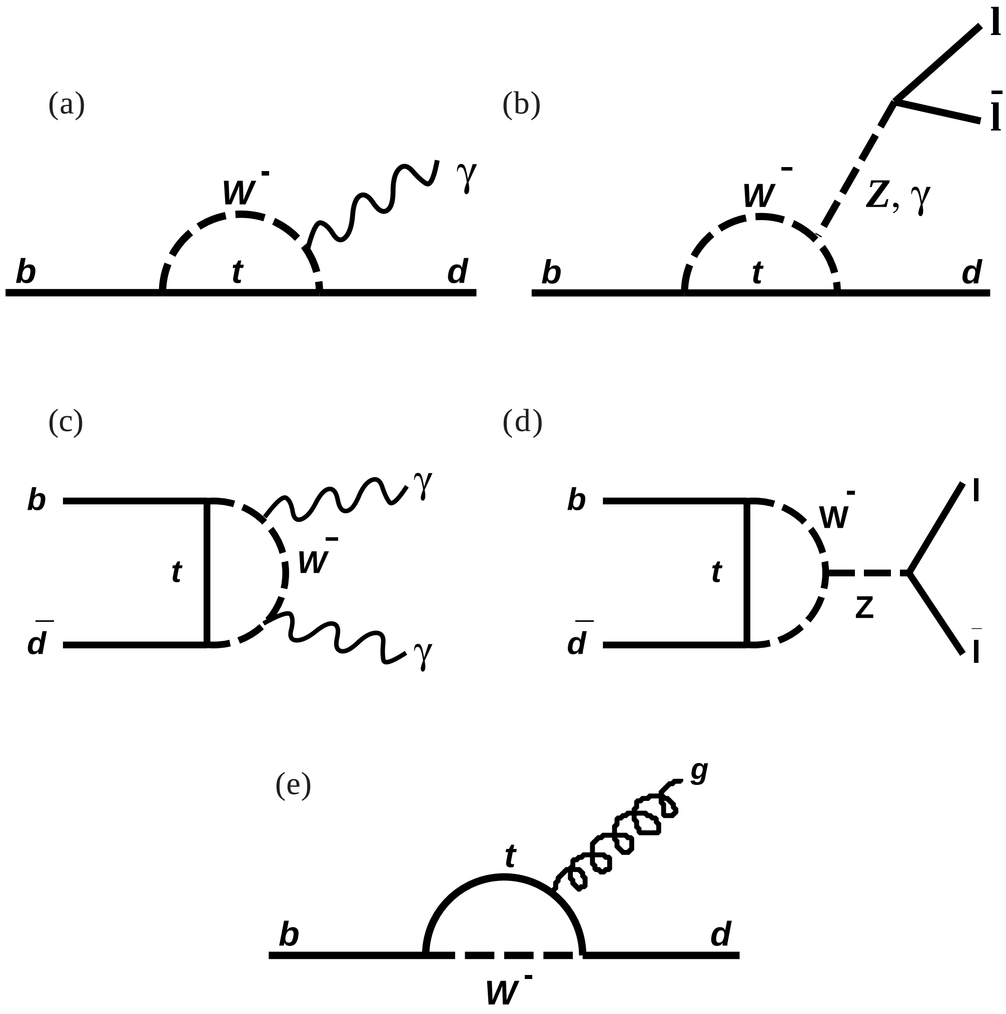

Figure 2: Penguin diagrams. (a) Radiative penguin (b) Electroweak penguin (c)(d) Vertical (annihilation) penguins (e) Gluonic penguin.

2.3 Radiative Penguins

In radiative penguin decays (such as $b \to s\gamma$), a charged particle emits an external real photon. The high energy photon is an excellent experimental signature. The inclusive decay rate is dominated by short distance interactions and can be calculated. The Standard Model predicts $\mathcal{B}(b \to s\gamma) = (3.15 \pm 0.23) \times 10^{-4}$(for $E_\gamma > 1.6$GeV) [3]. Experimental result reported by Belle is $\mathcal{B}(b \to s\gamma) = (3.32 \pm 0.19 \pm 0.37 \pm 0.01) \times 10^{-4}$ (for $E_\gamma >$1.7 GeV) [4]. Branching fraction extrapolated for E_γ cut to 1.6 GeV is $\mathcal{B}(b \to s\gamma) = (3.37 \pm 0.16 \pm 0.38 \pm 0.01) \times 10^{-4}$ [5]. Unfortunately, uncertainties in the hadronization process limit the ability to predict individual exclusive rates [6, 7].

The $b \to d\gamma$ process is further suppressed by $|V_{td}/V_{ts}|^2$ and give an alternative to $B^0 - \bar{B}^0$ mixing for extracting $|V_{td}|$. Experimentally, inclusive measurement has large background from the dominant $b \to s\gamma$ decays which must be rejected using excellent particle identification or kinematic separation. As this process is suppressed in the

Standard Model, they provide a good opportunity to look for non-Standard Model effects.

In the Standard Model predictions, the direct *CP* asymmetries of the inclusive $b \to s\gamma$ and $b \to d\gamma$ are [8]

$$A_{CP}^{b\to s\gamma} = (+0.0044^{+0.0024}_{-0.0014}) \tag{3}$$
$$A_{CP}^{b\to d\gamma} = (-0.102^{+0.0033}_{-0.0058}) \tag{4}$$

$A_{CP}^{b\to s\gamma}$ is potentially a sensitive probe of non-Standard physics, since its value within the Standard Model is so tiny. Finding an experimental value larger than a few percent would be a strong indication of new physics. For $b \to d\gamma$, $A_{CP}^{b\to d\gamma}$ is already large within the Standard Model; in this case, contributions due to non-standard physics might be more difficult to disentangle from the Standard Model contribution.

2.4 The $B \to (\rho, \omega)\gamma$ Decays

2.4.1 The $B \to (\rho, \omega)\gamma$ Decays in the Standard Model

The $B \to (\rho, \omega)\gamma$ mode is a radiative process described within the Standard Model by a $b \to d\gamma$ penguin diagram and observed by Belle [9] and Babar [10]. In the Standard Model, the branching fractions of these modes are predicted with 20-30% uncertainty, These large uncertainties of theoretical calculations are due to difficulties in calculating the hadronization of the final state mesons. Also QCD corrections to the penguin loop itself are hard to compute. Table 1 shows the calculations of branching fractions in the QCD factorization. The QCD factorization approach [11] provides a satisfactory theoretical basis for calculations of two-body radiative *B*-meson decays [12] and has been applied to the $B \to K^*\gamma$ and $B \to \rho\gamma$ modes [13]. In this framework, we can separate pertubatively calculable contributions from the nonpertubative form factors and meson light-cone distribution amplitudes. The information on various input hadronic quantities is taken from the Light-Cone Sum Rules [6, 14]. The calculation of Ref.[6] includes QCD factorization results and also the dominant contributions beyond QCD factorization, namely, long-distance photon emission [15] and soft-gluon emission [16] from quark loops.

The pertubative QCD approach [17, 18] is another theoretical approach which have also been used to study two-body radiative *B*-meson decays. In this framework, at least in the leading order, all nonpertubative effects can be included in the definition of the *B* meson and the vector meson wave functions, and the hard part of the amplitude can be computed in the pertubative theory.

The isospin asymmetry for the $B \to (\rho^0, \rho^+)\gamma$ decays is defined as

$$\Delta(\rho\gamma) = \frac{\tau_{B^0}}{2\tau_{B^+}} \frac{\mathcal{B}(B^+ \to \rho^+\gamma)}{\mathcal{B}(B^0 \to \rho^0\gamma)} - 1, \tag{5}$$

where $\frac{\tau_{B^+}}{\tau_{B^0}}$ is the ratio of the lifetime of B^+ and B^0. An weak annihilation diagram shown in Figure 3 and the penguin diagrams contribute to the $B^+ \to \rho^+\gamma$. $\Delta(\rho\gamma)$ is not zero

Table 1: NLO predictions for the $B \to (\rho, \omega)\gamma$ modes. All branching fractions are in units of 10^{-6}.

Calculation	$\mathcal{B}(B^+ \to \rho^+\gamma)$	$\mathcal{B}(B^0 \to \rho^0\gamma)$	$\mathcal{B}(B^0 \to \omega\gamma)$
Ali & Parkhomenko [19]	1.37 ± 0.28	0.65 ± 0.12	0.53 ± 0.12
Bosch & Buchalla [20]	$1.58\,^{+0.53}_{-0.46}$	-	-
Ball, Jones & Zwicky [6]	1.16 ± 0.26	0.55 ± 0.13	0.44 ± 0.10

because of the additional contribution from the weak annihilation. $\Delta(\rho\gamma)$ is correlated with the angle $\phi_2(\alpha)$ of the Unitarity Triangle and it can be used to provide supplement information on this angle. The CKM angle $\phi_2(\alpha)$ is defined as

$$\phi_2 \equiv arg\left[-\frac{V_{td}V_{tb}^*}{V_{ud}V_{ub}^*}\right]. \tag{6}$$

Since the weak annihilation diagram is proportional to $V_{ud}V_{ub}^*$ and the top quark dominated penguin diagram is proportional to $V_{td}V_{tb}^*$, the ratio of these two diagrams is proportional to

$$\lambda_u = \frac{V_{ub}V_{ud}^*}{V_{tb}V_{td}^*} = \left|\frac{V_{ub}V_{ud}^*}{V_{tb}V_{td}^*}\right| e^{i\phi_2}, \tag{7}$$

In the LO [19], the ratio of the branching fractions for the charged and neutral modes can be written as

$$\frac{\mathcal{B}(B^+ \to \rho^+\gamma)}{2\mathcal{B}(B^0 \to \rho^0\gamma)} \sim |1 + \epsilon_A \lambda_u|^2 , \tag{8}$$

where $\epsilon_A = -0.30 \pm 0.07$ [21] is the factor which lumps together the dominant W-annihilation and possible sub-dominant long-distance contributions.

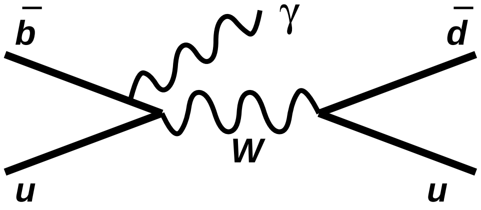

Figure 3: The weak annihilation contribution to the charged B decay.

The direct CP-violating asymmetry of $B \to \rho\gamma$ is defined as

$$A_{CP}(\rho\gamma) = \frac{\mathcal{B}(\bar{B} \to \bar{\rho}\gamma) - \mathcal{B}(B \to \rho\gamma)}{\mathcal{B}(B \to \rho\gamma) + \mathcal{B}(\bar{B} \to \bar{\rho}\gamma)}. \tag{9}$$

The Standard Model predictions with NLO calculation [22] are

$$A_{CP}(\rho^0\gamma) = (-8.4^{+4.4}_{-3.2}) \times 10^{-2} \tag{10}$$
$$A_{CP}(\rho^+\gamma) = (-10.4^{+6.0}_{-3.8}) \times 10^{-2}. \tag{11}$$

The predictions obtained with the pertubative QCD approach [23] are

$$A_{CP}(\rho^0\gamma) = (17.6 \pm 15.0) \times 10^{-2} \quad (12)$$
$$A_{CP}(\rho^+\gamma) = (17.7 \pm 15.0) \times 10^{-2}. \quad (13)$$

The $A_{CP}(\rho^+\gamma)$ is first analysis in this thesis.

Other decays related to $B \to (\rho,\omega)\gamma$ There are other decays related to $B \to (\rho,\omega)\gamma$. Two of these decays are $B^0 \to \phi\gamma$ and $B^0 \to J/\psi\gamma$. As shown in Figure 4, the dominant mechanism is the penguin annihilation process and the exchange of a W-boson process for the $B \to \phi\gamma$ and $B \to J/\psi\gamma$, respectively. In radiative B decays, no process of this kind has yet been observed. In the Standard Model, they are expected to be $\mathcal{B}(B \to \phi\gamma) = 3.6\times10^{-12}$ [24] and $\mathcal{B}(B \to J/\psi\gamma) = 7.65\times10^{-9}$ [25]. However, contributions to the $B \to \phi\gamma$ amplitude are possible from physics beyond the Standard Model if new heavy particles enter the loop. For example, some models of supersymmetry predict an enhancement of the $\mathcal{B}(B \to \phi\gamma)$ by up to $\sim 10^4$ [24]. Model of a right-handed charged current estimated to be $\mathcal{B}(B \to J/\psi\gamma) \sim 10^{-8}$ [25]. Experimentally, an upper limit is set on the branching fraction of $\mathcal{B}(B \to \phi\gamma) < 8.5 \times 10^{-7}$ [26] and $\mathcal{B}(B \to J/\psi\gamma) < 1.6 \times 10^{-6}$ [27] at the 90% confidence level by Babar.

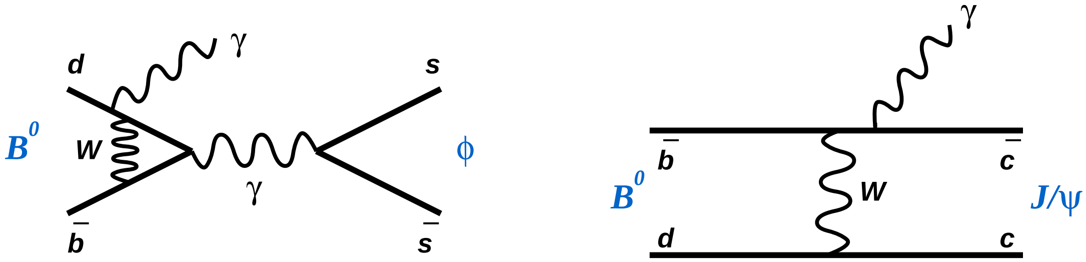

Figure 4: One of the leading order Feynman diagram contributing to the decay $B^0 \to \phi\gamma$ (left) and $B^0 \to J/\psi\gamma$ (right) in the Standard Model.

2.4.2 $B \to \rho\gamma$ decays in SUSY model

We consider two SUSY models, which are variants of the Minimal Supersymmetric Standard Model (MSSM), called the Minimal Flavour Violation (MFV) [28]and extended-MFV models [29]. In MFV models, all the flavor-changing sources are originated from the CKM matrix and included parameters are common mass of the heavy squarks other than the lightest stop ($M_{\tilde{q}}$), the mass of the lightest stop ($M_{\tilde{t}}$), the stop mixing angle ($\theta_{\tilde{t}}$), the ratio of the vacuum expectation value of the two Higgs bosons (tanβ_S), the two parameters of the chargino mass matrix (μ, M_2) and the charged Higgs mass ($M_{H^\pm}$).

Figures 5 shows constraints on $\Delta(\rho\gamma)$-$R(\rho\gamma/K^*\gamma)$ and the $A_{CP}(\rho\gamma)$-$R(\rho\gamma/K^*\gamma)$ planes from the Standard Model, MFV, and EMFV. $R(\rho\gamma/K^*\gamma)$ is the ratio of the branching fraction of $B \to \rho\gamma$ and $B \to K^*\gamma$. In Section 7, we calculate $R(\rho\gamma/K^*\gamma)$ to constrain on $|V_{td}/V_{ts}|$. $\Delta(\rho\gamma)$ is the isospin asymmetry. In the MFV case, parameters are in the following range:

$$M_{\tilde{t}} = [0.1, 1]\text{TeV}, \tag{14}$$

$$\theta_{\tilde{t}} = [-\pi, \pi], \tag{15}$$

$$\tan\beta_S = [3, 50], \tag{16}$$

$$M_2 = [0.1, 1]\text{TeV}, \tag{17}$$

$$M_{H^\pm} = [0.1, 1]\text{TeV}. \tag{18}$$

$M_{\tilde{q}}$ is set to 1 TeV.

EMFV differs from the Standard Model and the MFV due to an additional flavor changing structure beyond the CKM matrix. The source is the mixing of left-handed up-squark ($\tilde{q}_L^U$) and stop (denoted by $\delta_{\tilde{q}_L^U\tilde{t}}$). In the EMFV case, the range of the stop mixing angle $\theta_{\tilde{t}}$ is limited to [-0.3,0.3] and the parameter$\delta_{\tilde{q}_L^U\tilde{t}}$ is in the region;$|\delta_{\tilde{q}_L^U\tilde{t}}|$ = [0,1] and arg$\delta_{\tilde{q}_L^U\tilde{t}} = [-\pi, \pi]$. In the MFV case, there are two distinct regions corresponding to negative and positive C_7^s, where C_7^s is the Wilson coefficient for the magnetic moment operator (for $b \to s\gamma$). For $C_7^s < 0$, since the allowed region in MFV almost coincide with Standard Model, the region is not drawn. For $C_7^s > 0$, the allowed region is different from Standard Model one and sign of charge is opposite. In the EMFV case, both asymmetries tend to increase for smaller branching fraction ratio and the ratio is allowed to be large.

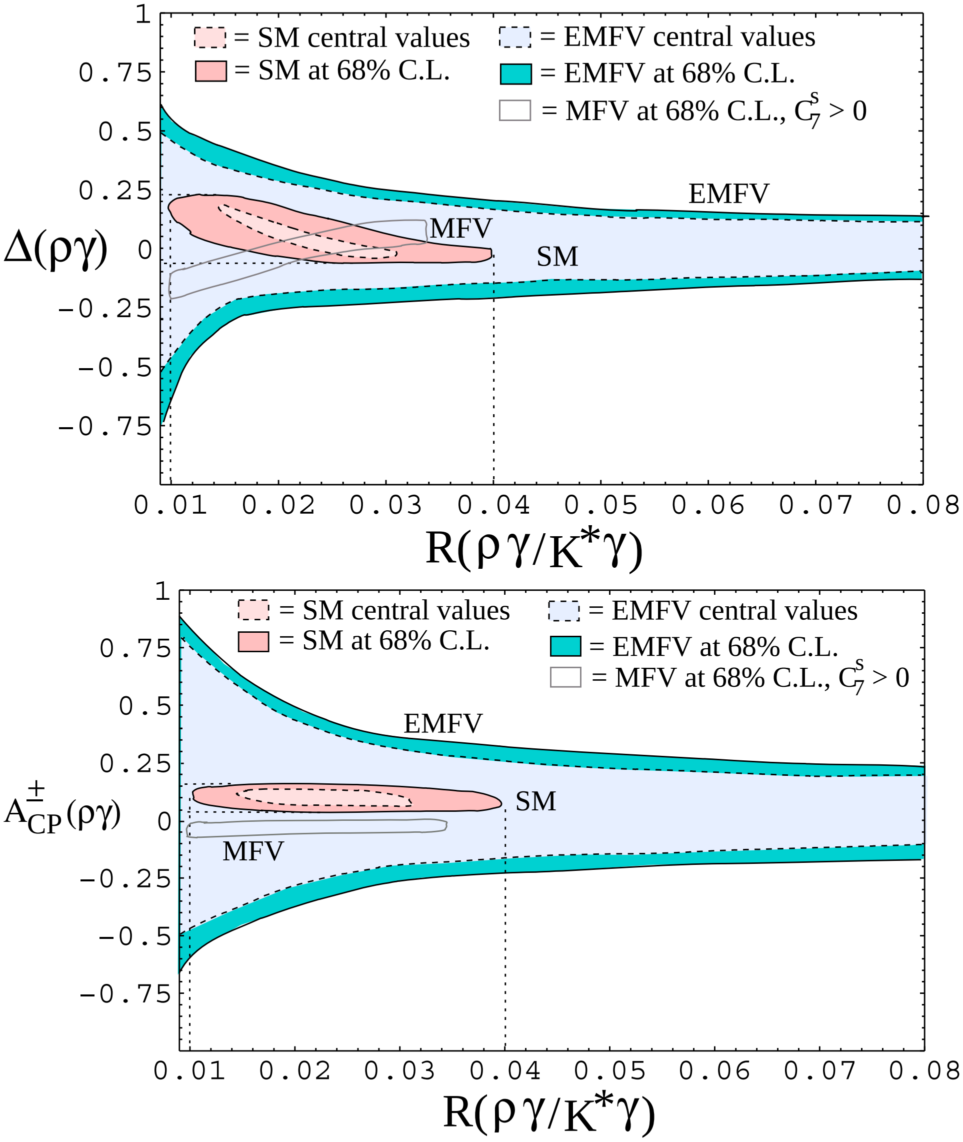

Figure 5: Correlation between $R(\rho\gamma/K^*\gamma)$ and $\Delta(\rho\gamma)$ (isospin asymmetry) (top) or A_{CP} (direct CP asymmetry) (bottom) in the Standard Model and the MFV and EMFV models. [30].

3 Experimental Apparatus

In this section, we describe the experimental apparatus of the KEK B factory which consists of the KEKB accelerator and the Belle detector. The experiment is located at High Energy Accelerator Research Organization (KEK) in Tsukuba-city, Japan.

3.1 KEKB Accelerator

KEKB [31] is a two-ring energy-asymmetric electron positron collider and produces B meson pairs as in a factory. Figure 6 shows a schematic layout of KEKB. It consists of two storage rings with circumference of 3.012 km, 8 GeV electrons ring (High Energy Ring, HER) and 3.5 GeV positrons ring (Low Energy Ring; LER). The two rings cross at the interaction point (IP) where electrons and positrons collide with a crossing angle of ±11 mrad. The center-of-mass energy is 10.58 GeV which corresponds to the mass of the $\Upsilon(4S)$ resonance. The $\Upsilon(4S)$ dominantly decay to $B^0\overline{B}^0$ and B^+B^- pairs which are created with a Lorentz boost of ($\beta\gamma$=0.425) due to the energy asymmetry. For measurement of time dependent asymmetry, the distance of the decay vertices (Δz) of the B meson pairs is measured instead of the difference of the decay time (Δt) from the relation $\Delta z \sim c\beta\gamma\Delta t$. The average flight length of B mesons is $c\tau_B\beta\gamma \sim 200\mu$m.

The design Luminosity of KEKB is 10^{34} cm^{-2}s^{-1}. KEKB achieved the world highest peak luminosity of 1.7×10^{34} cm^{-2}s^{-1}. The data collected by the Belle detector and KEKB until summer in 2007 is $604.5 fb^{-1}$[1].

---

[1] This only includes data taken at $\Upsilon(4S)$. About 1/10 of data are taken at 60 MeV below $\Upsilon(4S)$ and some data are taken at other energies.

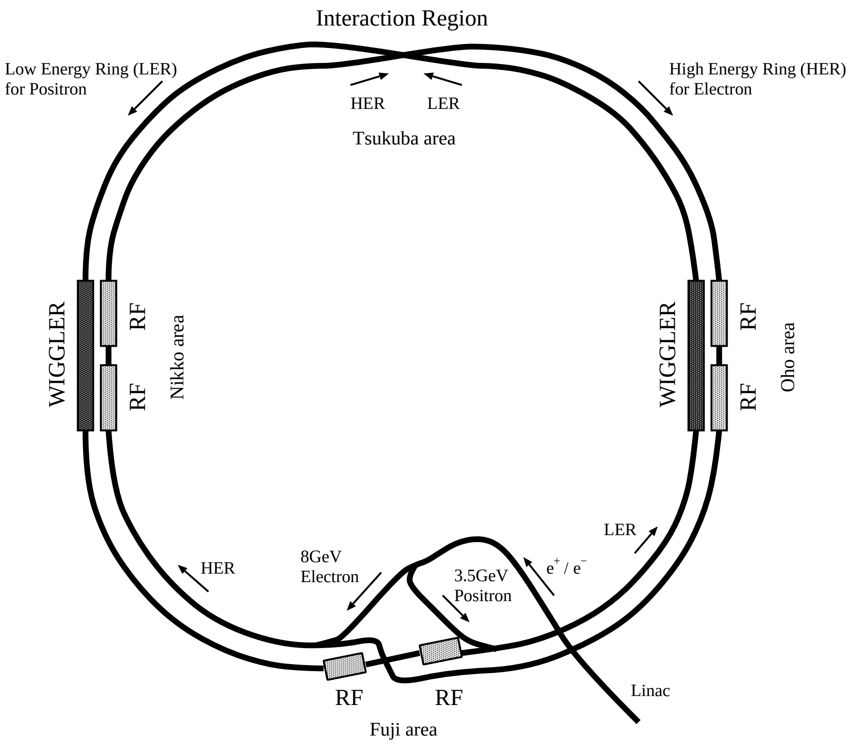

Figure 6: Schematic view of the layout of KEKB.

3.2 Belle Detector

Belle detector [32] is designed to surround interaction point covering a solid angle close to 4π. Figure 7 shows the configuration of the Belle detector. The detector is configured around a 1.5 T superconducting solenoid and iron structure surrounding the KEKB beam. B-meson decay vertices are measured by a silicon vertex detector (SVD) situated out side of a cylindrical beryllium beam-pipe. Charged particle tracking is provided by a wire drift chamber (CDC) together with the SVD. Particle identification (PID) is provided by dE/dx measured in CDC, aerogel Cherenkov counters (ACC) and time-of-flight counters (TOF) situated radially outside of the CDC. Electromagnetic particles are detected by an array of CsI(Tl) crystals (ECL) located inside the solenoid coil. The outermost detector is the K_L and muon detector (KLM), layers of resistive plate counters instrumented in the iron flux return. A pair of BGO crystal arrays (EFC), which is placed on the surfaces of the QCS (Quadrupole Collision Superconducting magnet) cryostat, covers forward and backward regions uncovered by the other detectors. Two inner detector configurations are used; A 3-layer SVD with a 2cm radius beam-pipe is used until the summer of 2003, while a 4-layer SVD, a 1.5cm radius beam-pipe, and a small-cell inner drift chamber are installed in the summer of 2003. A data sample of 140 fb^{-1} (DS-I) and 466 fb^{-1} (DS-II) are collected before and after the installation, respectively.

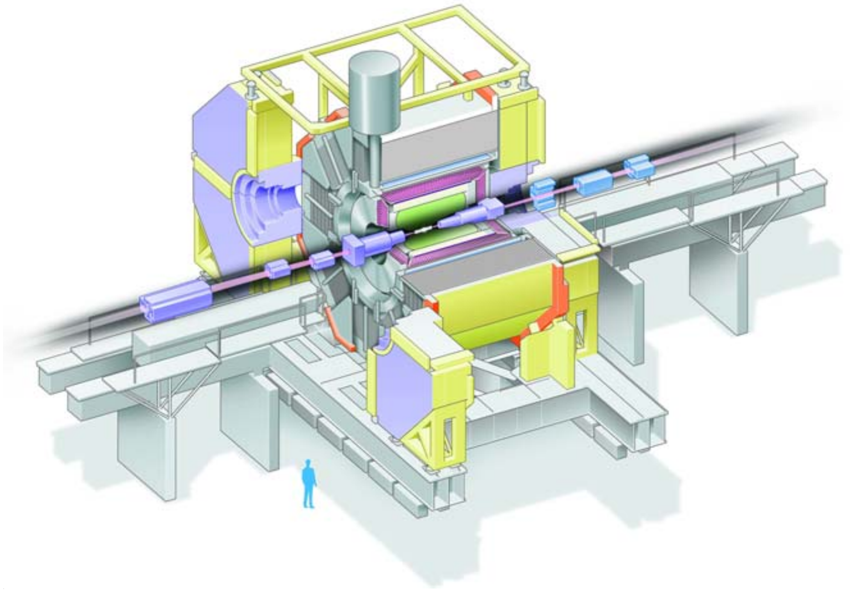

Figure 7: Overview of the Belle detector.

3.2.1 Silicon Vertex Detector (SVD)

Figure 8 shows side and end views of SVD for DS-I (SVD1). SVD1 consists of three concentric cylindrical layers arranged in a barrel and covers the angle range $23^\circ < \theta < 139^\circ$ (θ is the angle from the z axis defined opposite to the positron beam) which corresponds to 86% of the full solid angle in the center-of-mass frame. The three layers at 30.0mm, 45.5mm and 65.5mm radii surround the beam pipe that has a double-wall beryllium cylinder of 2.3 cm radius and 1mm thickness. There are 8/10/14 ladders along ϕ in layers 1/2/3, respectively, where ϕ is the azimuthal angle around the z axis. Each ladder consists of double-sided silicon strip detectors (DSSDs) reinforced by boron-nitride support ribs.We use DSSDs fabricated by Hamamatsu Photonics (HPK). These detectors were originally developed for DELPHI micro-vertex detectors. Each DSSD consists of 1280 sense strips and 640 readout pads on each side. The z-strip pitch is 42μm and the ϕ-strip pitch is 25μm. The size of the DSSD is 57.5×33.5 mm^2 with 300 μm thickness, where the active area is 53.3×32.0 (54.5×32.0) mm^2 on the z-side (ϕ-side). We use 102 DSSDs in total. For the z-coordinate measurement, a double-metal structure running parallel to z is employed to route the signals from orthogonal z-sense strips to the ends of the detector. Adjacent strips are connected to a single readout trace on the second metal layer which gives an effective strip pitch of 84μm. A *p*-stop structure is employed to isolate the z-sense strips. A relatively large thermal noise (600 e^-) is observed due to the common-*p*-stop design. On the ϕ side, every other sense strip is connected to a readout channel. Charge collected by the floating strips (the strips unconnected to readout channel) in between is read from adjacent strips by means of capacitive charge devision. The readout chain of DSSDs is based on the VA1 integrated circuit [33]. The VA1 chip is a 128-channel CMOS integrated circuit produced by IDEAS [2]. It is specially designed for the readout of silicon vertex

---

[2] http://www.ideas.no/

detectors and other small-signal devices. The VA1 has excellent noise performance and reasonably good radiation tolerance of 200kRad thanks to VA1 fabricated in the Austrian Micro Systems(AMS) 1.2 μm process [34]

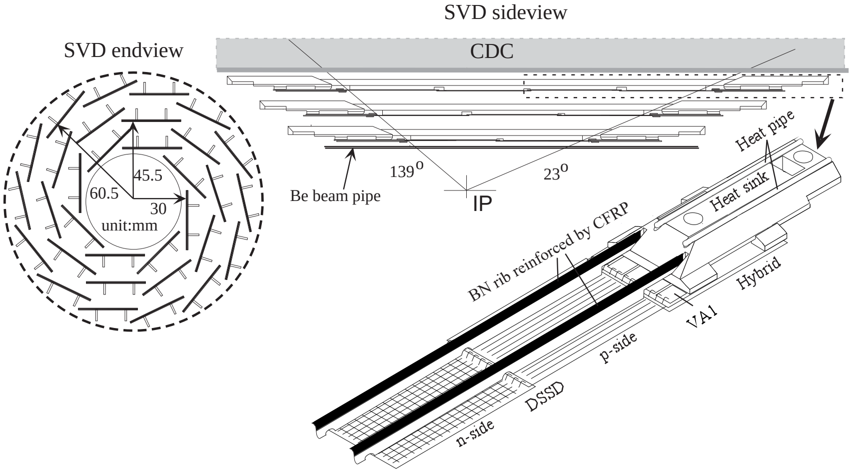

Figure 8: Detector configuration of SVD1.

SVD2 [35], a new vertex detector, was installed in the summer of 2003. Figure 9 shows configuration of SVD2. SVD2 has four detector layers of 20.0mm, 43.5 mm, 70.0mm and 88.0mm radii. There are 6/12/18/18 ladders in layers 1/2/3/4, respectively. The polar angle coverage is expanded to $17^\circ < \theta < 150^\circ$, which is the same as that of the CDC and corresponds to the 92% of the full solid angle. The DSSDs are fabricated by HPK. The size of the DSSD for the layers 1-3/4 is 28.4×79.2 mm^2/34.9×76.4 mm^2 with 300 μm thickness. Each DSSD has 1024 and 512 sense strips in z(p)-side and ϕ(n)-side, respectively. For the inner three layers, the z-strip(ϕ-strip) pitch is 74 μm(50 μm). For the fourth layer, the z-strip(ϕ-strip) pitch is 73 μm(65 μm). Every ϕ-strip for each DSSD is read out, while every other strip is read out in z-side. In total, 246 DSSDs are used and the number of readout channels is 110,592. Instead of double-metal structure, flex circuits are used to read out the z-strips, which reduces the capacitance compared with the double-metal layer. The read out chain for DSSDs is based on the VA1TA integrated circuit. The VA1TA chip is a 128-channel CMOS integrated circuit, produced by IDEAS, having a trigger capability in addition to the preamplifier function. It is fabricated with AMS 0.35 μm process and has an excellent radiation tolerance of 20Mrad[34]. The impact parameter resolution for reconstructed tracks is measured as a function of the track momentum p (unit in GeV/c) and the polar angle θ. It can be fitted by a function of

$$\sigma = \sqrt{\sigma_1^2 + \left(\frac{\sigma_2}{\tilde{p}}\right)} \tag{19}$$

and is presented as

$$\sigma = \sigma_1 \oplus \sigma_2/\tilde{p} \tag{20}$$

where $\tilde{p}$ is the pseudo-momentum defined as

$$\tilde{p} \equiv \begin{cases} p\beta\sin^{3/2}\theta & \text{for } r-\phi \text{ side,} \\ p\beta\sin^{5/2}\theta & \text{for } z \text{ side} \end{cases} \tag{21}$$

The impact parameter resolutions measured with the cosmic ray events are

$$\sigma_{r\phi}(\mu\mathrm{m}) = 19.2 \oplus 54.0/\tilde{p}, \sigma_z(\mu\mathrm{m}) = 42.2 \oplus 44.3/\tilde{p}, \tag{22}$$

for SVD1, and

$$\sigma_{r\phi}(\mu\mathrm{m}) = 21.9 \oplus 35.5/\tilde{p}, \sigma_z(\mu\mathrm{m}) = 27.8 \oplus 31.9/\tilde{p}, \tag{23}$$

for SVD2.

The impact parameter resolutions of SVD2 are better than those of SVD1 due to the smaller radius of the first layer.

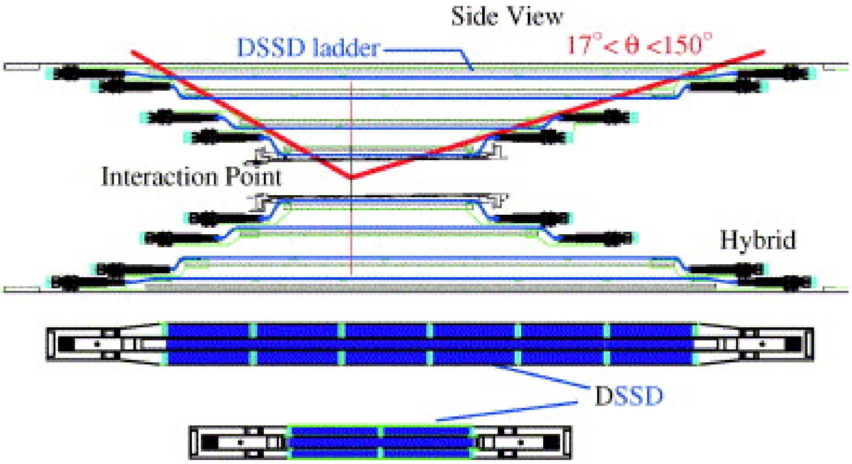

Figure 9: Detector configuration of SVD2.

3.2.2 Central Drift Chamber (CDC)

Efficient reconstruction of charged particle tracks and precise determination of their momenta are essential for almost all of the measurements in the Belle experiment. CDC determines trajectories for charged particles, which provides the measurement of momenta for charged particles. In addition, the charged particle tracking system is expected to provide important information for the trigger system and PID information by the precise dE/dx measurements.

The CDC [36] is designed and constructed to meet the requirements for the central tracking system. Since the majority of the decay particles of B meson have momenta lower than 1 GeV/c, the minimization of multiple scattering is important for improvement of the momentum resolution. Therefore, the use of a low-Z gas is desirable, while a good dE/dx resolution must be retained.

Figure 10 shows the structure of the CDC. It is asymmetric in the z direction in order to cover the angle region of $17^\circ \leq \theta \leq 150^\circ$. The longest wires are 2400mm long. The inner radius is 83 mm and the outer radius is 880 mm.

The original CDC has 50 cylindrical layers, consisting of six axial super-layers (32 layers) and five stereo super-layers (18 layers), where innermost three layers have cathode strip readout (cathode part). In the summer of 2003, the inner part of CDC has modified with the installation of SVD2. The cathode part was replaced with two layers of small-cell CDC (sCDC). Axial wires are parallel to the z axis, while stereo wires slant to the z axis in order to provide z position information. A total number of drift cells is 8400 (8464) for SVD1 (SVD2) configuration. The cathode part provides a z position measurement for the particles enter CDC and also information for the trigger. A low-Z gas, a 50% helim-50% ethane mixture, is used to minimize multiple Coulomb scattering contributions to the momentum resolution. Since low-Z gases have a smaller photo-electric cross section than argon-based gases, they have an additional advantage of reduced background from synchrotron radiation. Even though the gas mixture has a low-Z, a good dE/dx resolution is provided by the large ethane component.
The measured spatial resolution is $\sim$ 120-150μm with a dependence on the incident angles and layers. The p_t resolution obtained by the using cosmic ray is

$$\frac{\sigma_{p_t}}{p_t}(\%) = \sqrt{(0.28p_t)^2 + (0.35/\beta)^2} \quad (p_t \ \mathrm{GeV}/c) \tag{24}$$

without the SVD information, and

$$\frac{\sigma_{p_t}}{p_t}(\%) = \sqrt{(0.19p_t)^2 + (0.30/\beta)^2} \quad (p_t \ \mathrm{GeV}/c) \tag{25}$$

with the SVD information.

The dE/dx measurement in CDC provides information for PID. A scatter plot of measured dE/dx and particle momentum is shown in Figure 11. Populations of pions, kaons, protons and electrons can be clearly seen. The dE/dx resolution is measured to be 7.8% in the momentum range from 0.4 to 0.6 GeV/c.

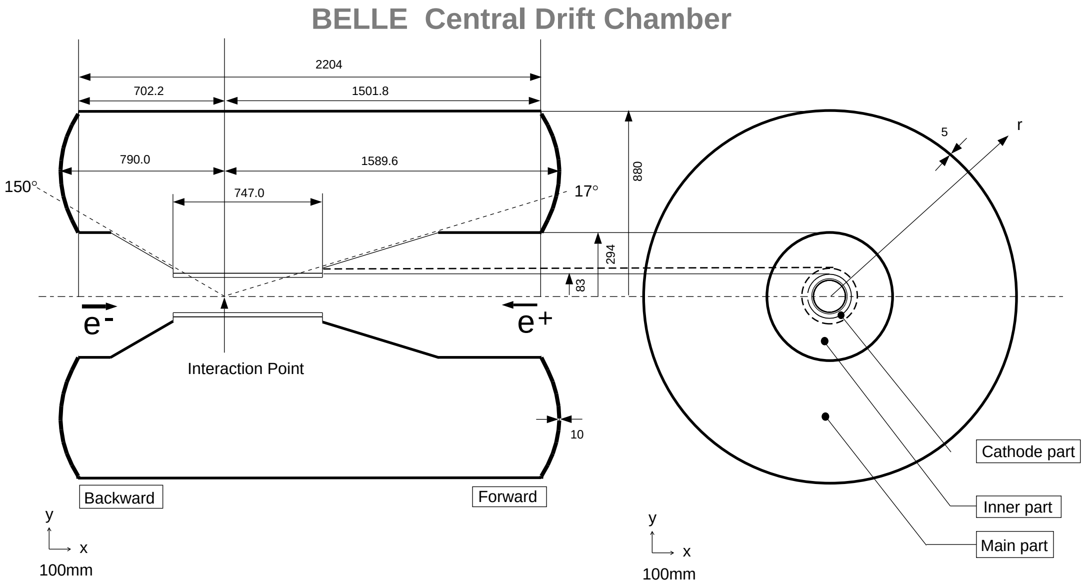

Figure 10: Overview of the CDC structure

3.2.3 Aerogel Cherenkov Counter (ACC)

Particle identification, specifically the discrimination of charged pions from charged kaon, is important for the many analyses of B decays. An array of silica aerogel threshold Cherenkov counters has been selected as part of the Belle PID system to extend the momentum coverage beyond the reach of dE/dx measurements by CDC and time-of-flight measurements by TOF. The configuration of ACC is shown in Figure 12. The ACC consists of 960 counter modules segmented into 60 cells in the ϕ direction for the barrel part and 228 modules arranged in five concentric layers for the forward end-cap part of the detector [37]. The barrel ACC has a momentum coverage of $1.2-3.6$ GeV/c and end-cap 0.8 – 2.2 GeV/c with $\sim 3\sigma$ K/π separation [38]. All the counters are arranged in a semi-tower geometry, pointing to the IP. In order to obtain good π/K separation for the whole kinematical range, the refractive indices of aerogels are selected to be between 1.01 and 1.03, depending on their polar angle region. The choice of the refractive index for the barrel ACC is optimized for separation of high momentum pions and kaons from the two-body B decays, such as $B \to \pi\pi$ and πK. For the end-cap ACC, n = 1.030 has been chosen to cover the flavor tagging region. A typical single ACC module is shown in Figure 13 for the barrel and the end-cap ACC. Five aerogel tiles are stacked in thin (0.2 mm thick) aluminum box of approximate dimensions $12\times12\times12\text{cm}^3$. In order to detect Cherenkov lights effectively, one or two fine mesh-type photomultiplier tubes (FM-PMTs), which are operated in a magnetic field of 1.5 T, are attached directly to the aerogel at the sides of the box. The performance of ACC is confirmed using the charm decay, $D^{*+} \to D^0\pi^+(D^0 \to K^-\pi^+)$. The slow π^+ from D^{*0} allows to identify the daughter K and π from the D^0 directly by their relative charges with respect to the slow pion. Figure 14 shows the number of photo-electron distribution of π^+ and K^- in this decay, where the K/π separation is good and consistent

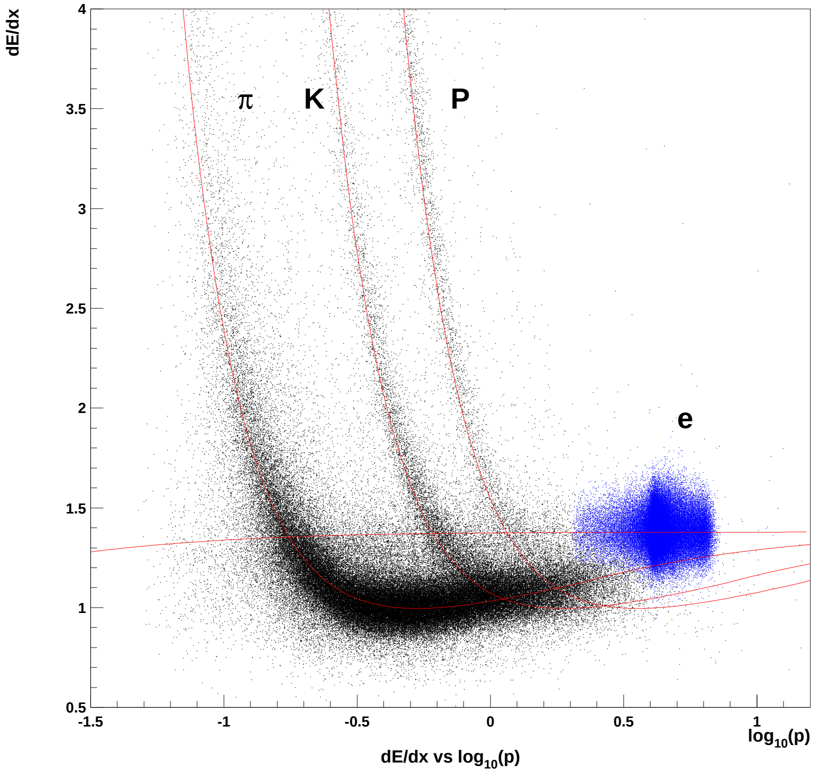

Figure 11: dE/dx versus charged track momentum observed in collision data. Black dots are from hadronic events and blue dots are from (radiative) Bhabha events. Solid curves show the expected mean energy losses for different particle types π, K, proton and electron.

with MC.

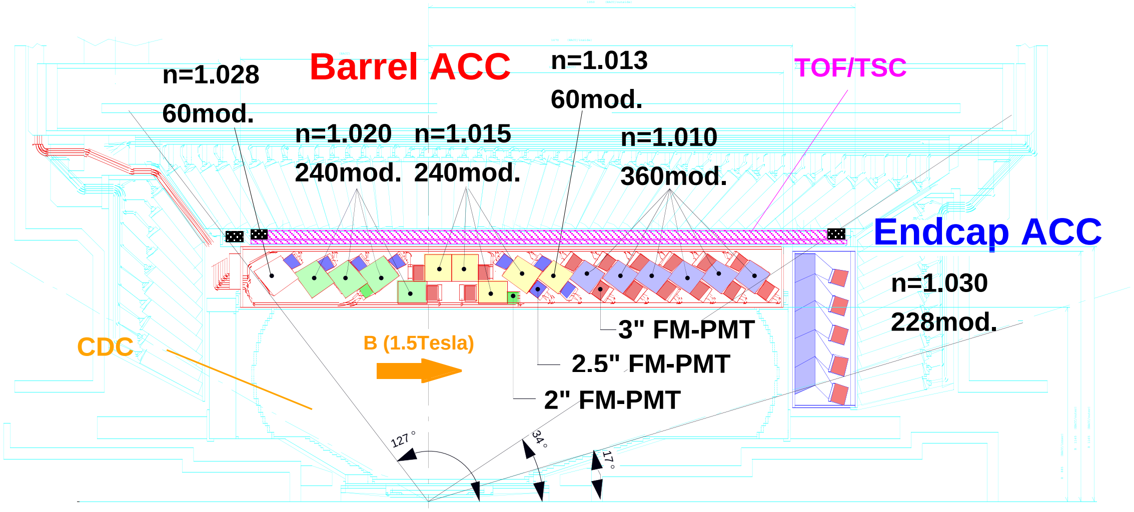

Figure 12: Arrangement of ACC in the Belle detector

a) Barrel ACC Module

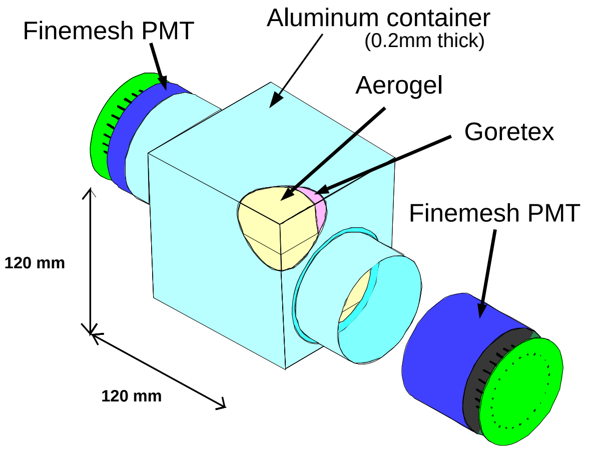

b) Endcap ACC Module

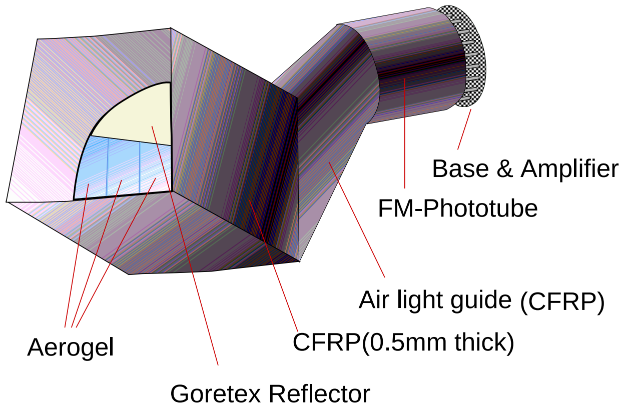

Figure 13: Schematic drawing of a typical ACC counter:

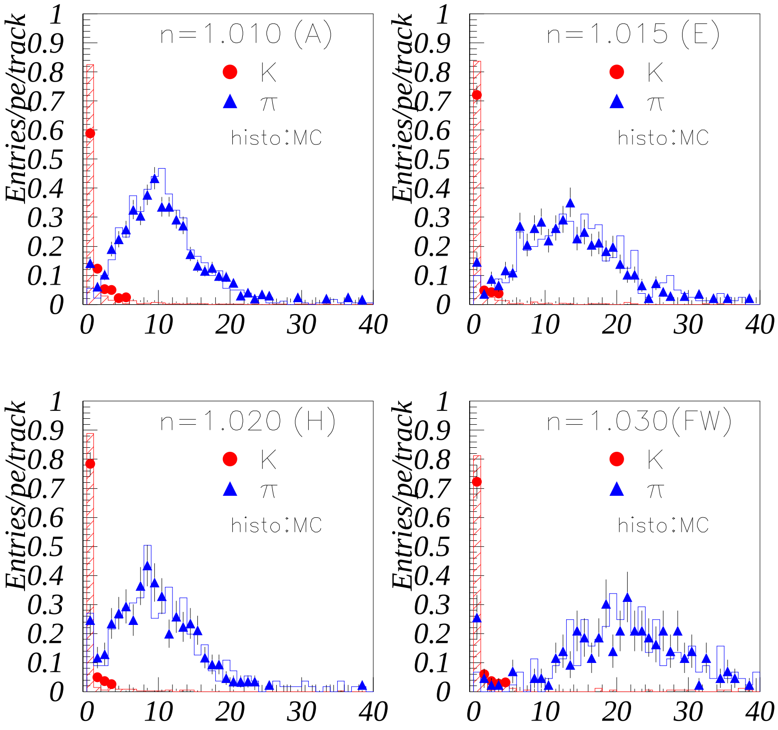

Figure 14: Distribution of photo-electron measured by the ACC in $D^{*+} \to D^0\pi^+(D^0 \to K^-\pi^+)$ decays.

3.2.4 Time-Of-Flight (TOF)

A time-of-flight (TOF) detector system using plastic scintillator counters [39] is very powerful for particle identification in e^+e^- collider detectors. For a 1.2 m flight path, the TOF system with 100 ps time resolution is effective for particle momenta below 1.2 GeV/c. This momentum region encompasses 90% of the particles produced in Υ(4S) decays. It plays an essential role in b-flavor tagging. In addition to particle identification, the TOF counters provide fast timing signals for the trigger system. To avoid pile-up in the trigger queue, the rate of the TOF trigger signal must be kept below 70kHz. Simulation studies indicate that to keep the fast trigger rate below 70kHz in any beam conditions, it needs thin trigger scintillation counters (TSC) which make up for the TOF counters. The TOF system consist of 128 TOF counters and 64 TSC counters. Two trapezoidal shaped TOF counters and one TSC counter, with a 1.5-cm intervening radial gap, form one module. In total 64 TOF/TSC modules located at a radius of 1.2 m from the IP cover a polar angle range from 34° to 120°. The minimum transverse momentum to reach the TOF counters is about 0.28 GeV/c. Figure 15 shows the module dimensions. These modules are individually mounted on the inner wall of the barrel ECL container. The 1.5 cm gap between the TOF counters and TSC counters is introduced to isolate TOF from photon conversion background by taking the coincidence between the TOF and TSC counters. Electron and positrons created in the TSC layer are prevented from reaching the TOF counters due to this gap in a 1.5 T magnetic field. FM-PMTs are attached to the TOF counter ends with an air gap of ~ 0.1 mm, which selectively passes earlier arrival photons and reduces a gain saturation effect of FM-PMTs due to large pulses at very high rate. As the time resolution is determined by the rising edge of the time profile of arrival photons at PMT, the air gap hardly affects the time resolution. In the case of the TSC counters the tubes are glued to the light guides at the backward ends. Figure 16 shows time resolutions for forward and backward PMTs and for the wighted average time as a function of z. The resolution for the weighted average time is about 100 ps with a small z dependence. Figure 17 shows the mass distribution for each track in hadron events, calculated using the equation

$$mass = p\sqrt{\left(\frac{cT}{L}\right)^2 - 1} \quad (T\text{: Time of flight}) \tag{26}$$

where p and L are the momentum and path length of the particle determined from the CDC track fit assuming the muon mass, respectively with the time-of-flight(T) measured by the TOF system. Clear peaks corresponding to pion, kaon and proton are seen. The data points well agree with a Monte Carlo prediction (histogram) obtained by assuming resolution of TOF $\sigma_{TOF} = 100$ps.

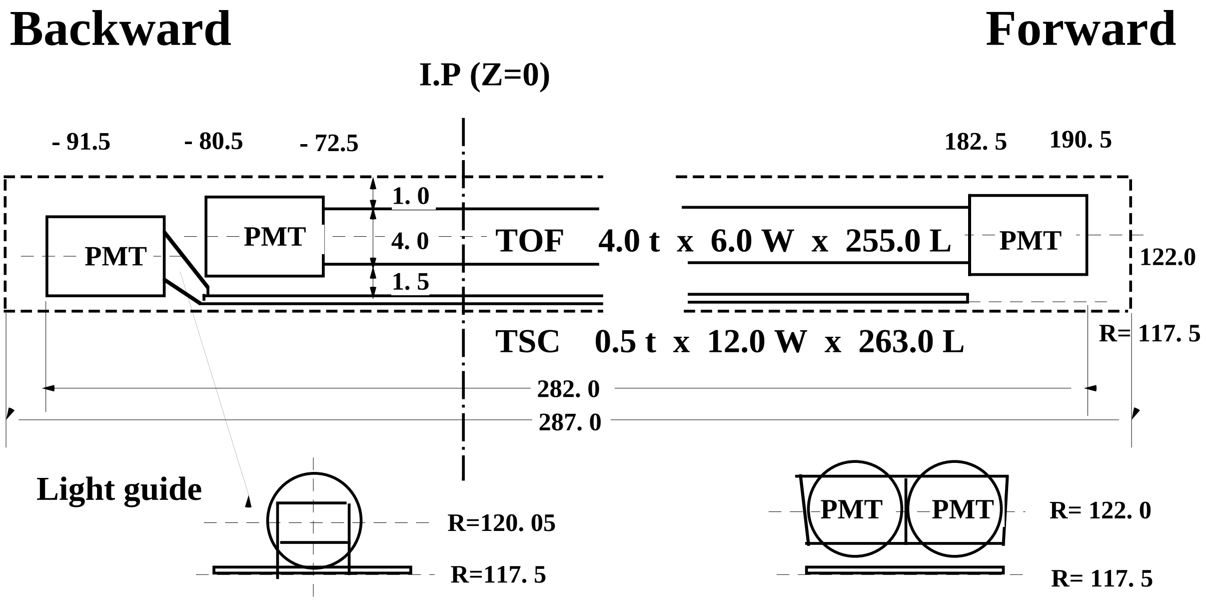

Figure 15: Dimensions of a TOF/TSC module

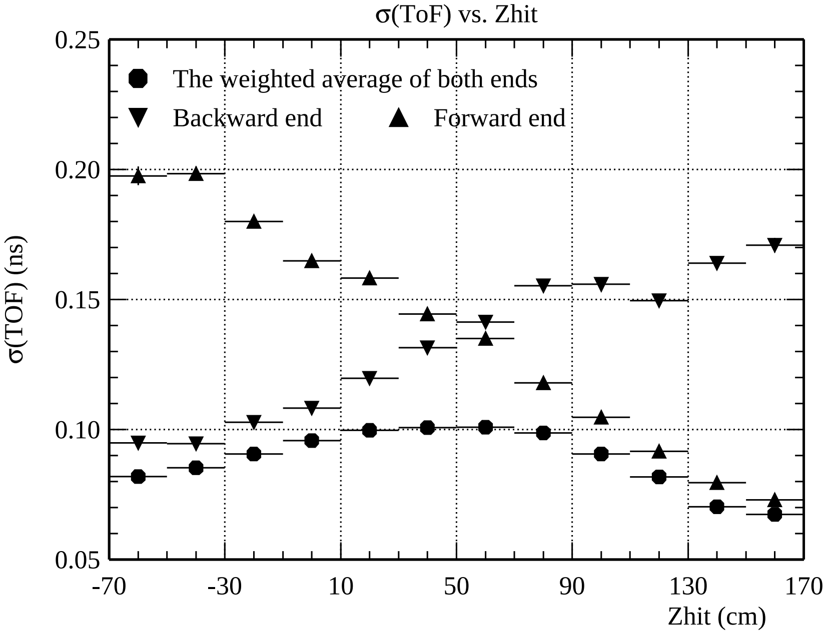

Figure 16: Time resolution of TOF for μ-pair event ($e^+e^- \rightarrow \mu^+\mu^-$).

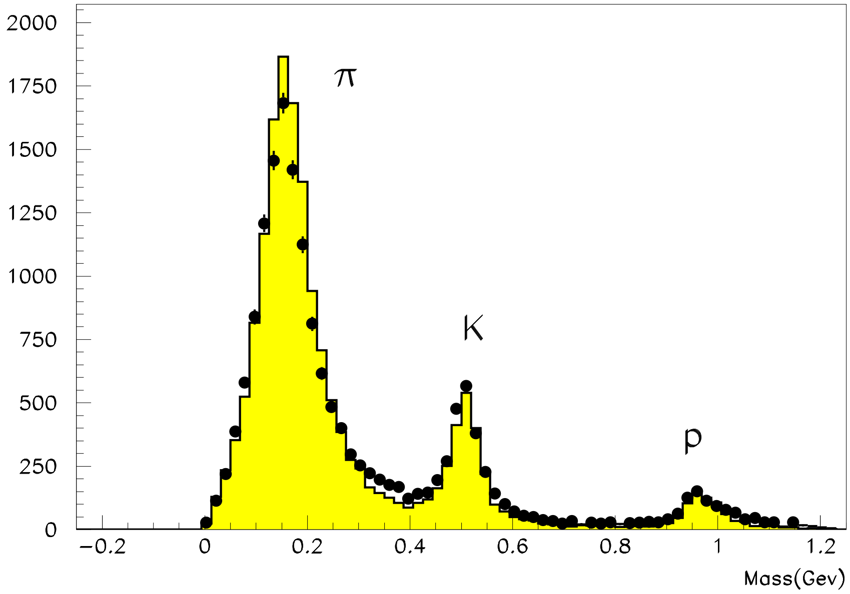

Figure 17: Mass distribution from TOF measurements for particle momenta below 1.2 GeV/c. The histogram corresponds to MC.

3.2.5 Electromagnetic Calorimeter (ECL)

The main purpose of the electromagnetic calorimeter is to detect photons from B meson decays with high efficiency and good resolution in energy and position. Since most of these photons are end products of cascade decay, they have relatively low energies and, thus, good performance below 500 MeV is especially important. On the other hand, since important two-body decay modes, such as $B \rightarrow K^{*}\gamma$ and $B^0 \rightarrow \pi^0\pi^0$, produce photons energies up to 4 GeV, good resolution for high momentum region is also needed to reduce backgrounds for these modes. Electron identification in Belle relies primarily on comparison of the charged particle momentum and the energy deposits in the electromagnetic calorimeter. Good electromagnetic energy resolution results in better hadron rejection. High momentum π^0 detection requires the separation of two nearby photons and precise determination of their opening angle. This requires a fine-grained segmentation in the calorimeter.

In order to satisfy the above requirements, we have decided to use a highly segmented array of CsI(Tl) crystals with silicon photo-diode readout installed in a magnetic field of 1.5 T inside a super-conducting solenoid magnet. CsI(Tl) crystals have various nice features such as a large photon yield, weak hygroscopicity, mechanical stability and moderate price.

Figure 18 shows the overall configuration of the Belle electromagnetic calorimeter system, ECL [40]. The ECL consists of the barrel section of 3.0 m in length with the inner radius of 1.25 m and the annular end-caps at z = +2.0 m and z = -1.0 m from the interaction point. Each crystal has a tower-like shape and is arranged to point almost to IP. There is a small tilt angle of 1.3° in the θ and ϕ directions in the barrel section to avoid photons escaping through the gap of the crystals. End-cap crystals are tilted by $\sim 1.5^\circ$ and $\sim 4^\circ$ in the θ direction in the forward and back-forward sections, respectively. The ECL cover the polar angle region of $17.0^\circ < \theta < 150.0^\circ$, corresponding to a total solid-angle coverage of 92% of 4π. Small gaps between the barrel and end-cap crystals provide a pathway for cables and room for supporting members of the inner detectors. The loss of solid angle associated with these gaps is $\sim$ 3% of the total acceptance. The entire system contains 8736 CsI(Tl) counters and weighs 43 tons. The size of each CsI(Tl) crystal is determined so that a crystal contains approximately 80% of the total energy deposited by a photon injected at the center of the its face. The typical dimension of a crystal is 55 mm × 55 mm at front face and 65 mm × 65 mm at rear face for the barrel part. For the end-cap part, the dimension of the front and rear surfaces vary from 44.5 mm to 70.8 mm and from 54 mm to 82 mm, respectively. The length, 30 cm, corresponds to $16.2X_0$ (radiation length) which is determined to avoid deterioration of the energy resolution at high energies due to the fluctuations of shower leakage from rear of the counter.

The energy resolution given by beam test as shown below.

$$\frac{\sigma_E}{E}(\%) = \sqrt{\left(\frac{0.066}{E}\right)^2 + \left(\frac{0.81}{\sqrt[4]{E}}\right)^2 + 1.34^2} \quad (E \text{ in GeV}) \tag{27}$$

This is consistent with the collision data calibrated by $e^+e^- \rightarrow e^+e^-$ (Bhabha) events, where the energy resolution are 1.5%, 1.9% and 2.5% for the barrel, forward and backward ECL, respectively.

The energy dependence of the average position resolution is measured by the beam test and can be approximated by

$$\sigma(mm) = 0.27 + \frac{3.4}{\sqrt{(E)}} + \frac{1.8}{\sqrt[4]{(E)}} \quad (E \text{ in GeV}) \tag{28}$$

which is shown in Figure 19. As can be seen in the figure, the result of the beam test is well consistent with MC estimation.

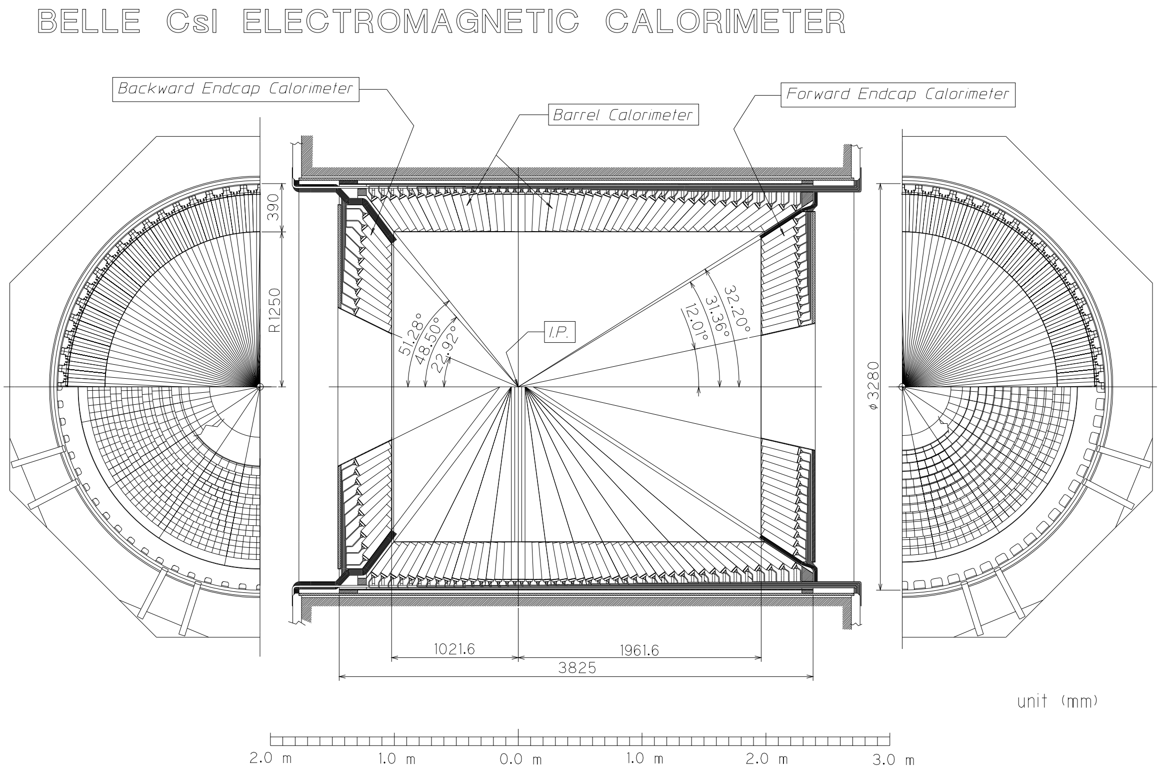

Figure 18: Overall configuration of ECL.

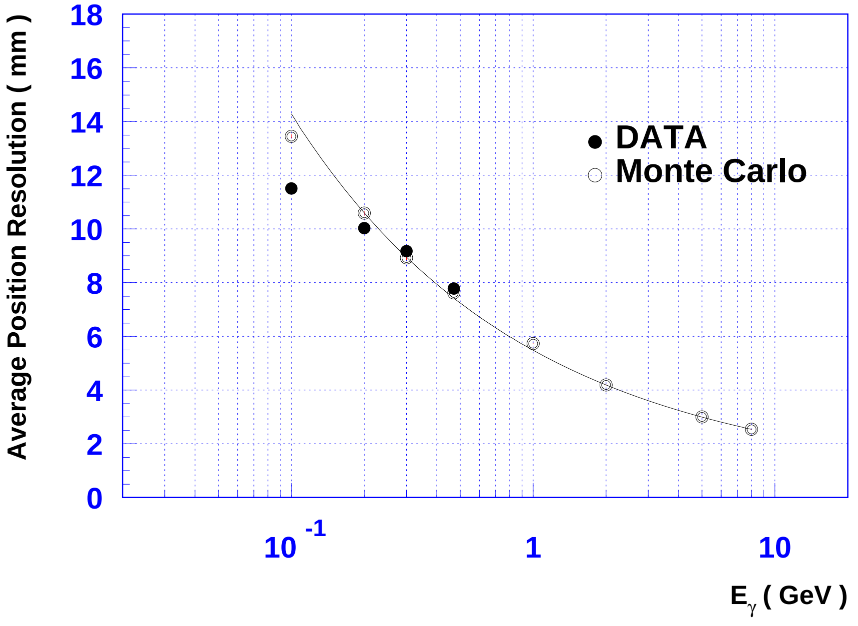

Figure 19: Energy dependence of the average position resolution, The solid curve is a fit to MC.

3.2.6 K_L^0 and Muon Detector (KLM)

The KLM detection system [41] is designed to identify K_L^0 and muons with high efficiency over a broad momentum range greater than 600 MeV/c. KLM consists of alternating layers of charged particle detectors and 4.7 cm-thick iron plates. There are 15 detector layers and 14 iron layers in the octagonal barrel region and 14 detector layers in each of the forward and backward end-cap. The iron plates provide a total of 3.9 interaction lengths of material for a particle traveling normal to the detector plates. In addition, ECL provides another 0.8 interaction length of material. K_L^0 that interacts in the iron or ECL produces a shower of ionizing particles. The location of this shower determines the direction of K_L^0, but fluctuations in the size of the shower do not allow a useful measurement of the K_L^0 energy. The multiple layers of charged particle detectors and iron allow the discrimination between muons and charged hadrons ($\pi^\pm$ or $K^\pm$) based on their range and transverse scattering. Muons travel much farther with smaller deflections on average than strongly interaction hadrons.

The detection of charged particles is provided by glass-electrode resistive plate counters (RPC) [42]. RPC have two parallel plate electrodes with high bulk resistivity ($\geq 10^{10}\Omega$ cm) separated by a gas-filled gap. In the streamer mode, an ionizing particle traversing the gap initiates a streamer in the gas that results in a local discharge of the plates. This discharge is limited by the high resistivity of the plates and the quenching characteristics of the gas. The discharge induces a signal on external pickup strips, which can be used to record the location and the time of the ionization. Figure 20 shows the cross section of a super-layer, in which two RPCs are sandwiched between the orthogonal θ and ϕ pickup-strips with the ground planes for signal reference and proper impedance. The unit structure of two RPCs and two readout-planes is enclosed in an aluminum box and is less than 3.7 cm thick. Each RPC is electrically insulated with a double layer of 0.125 mm thick mylar. Signals from both RPCs are picked up by copper strips above and below the pair of RPCs, providing a three-dimensional space point for particle tracking. Each barrel module has two rectangular RPCs with 48 z pickup strips perpendicular to the beam direction. The smaller 7 super-layers closest to the IP have 36 ϕ strips and the outer 8 super-layers have 48 ϕ strips orthogonal to the z strips. Each end-cap super-layer module contains 10-π-shaped RPCs and have the 96 ϕ and 46 θ pickup-strips. In order to identify K_L, tracks of charged particles measured in CDC are extrapolated into KLM. Clusters within 15 degrees of an extrapolated charged particle track are excluded from K_L cluster candidates. For an isolated cluster, the center of gravity of the hits is calculated and used to determine the direction of the cluster from the IP. Figure 21 shows a histogram of the difference between the direction of the K_L cluster candidate and the missing momentum. The missing momentum direction is calculated using all the other measured particles in the event. The histogram shows a clear peak where the direction of the neutral cluster measured in KLM is consistent with the missing momentum in the event. The flat-component in the histogram is mainly due to undetected neutrinos and particles escaping the detector acceptance.

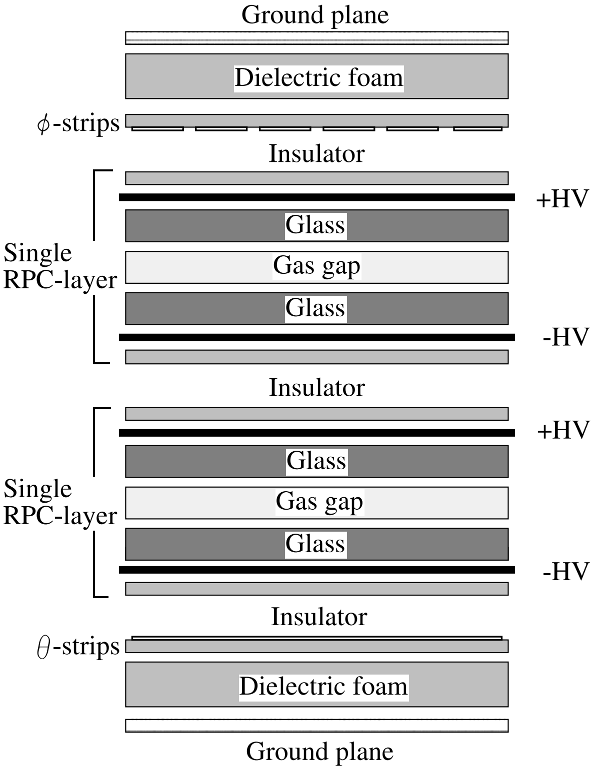

Figure 20: Cross section of a KLM super-layer.

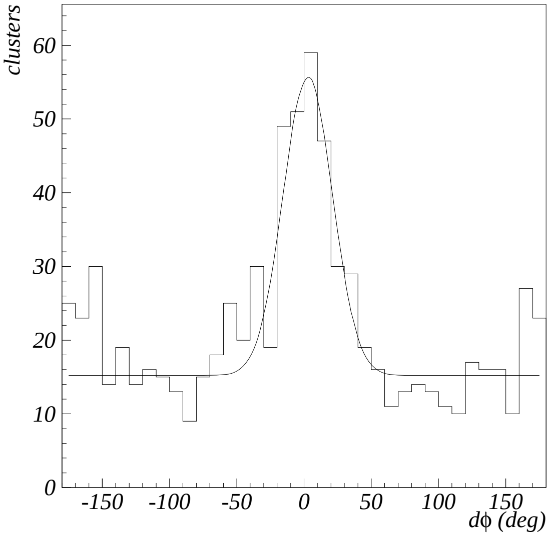

Figure 21: Difference the direction between the neutral cluster and the missing momentum.

3.2.7 Extreme Forward Calorimeter (EFC)

EFC extend the polar angle coverage by ECL, $17^\circ < \theta < 150^\circ$. EFC covers the angle range from 6.4° to 11.5° in the forward direction and from 163.3° to 171.2° in the backward direction. EFC is required to function as a beam mask to reduce background for CDC. In addition, EFC is used for a beam monitor for KEKB control and a luminosity monitor for the Belle experiment. It can also be used a tagging device for two-photon physics.

Since EFC is placed in the very high radiation level area around the beam pipe near the interaction point, it is required to be radiation hard. Therefore, we use a radiation hard BGO (Bismuth Germante, $Bi_4Ge_3O_{12}$) crystal calorimeter with silicon photo-diodes for readout [43]. Figure 22 shows a view of the crystal arrangements. The detector is segmented into 32 in ϕ and 5 in θ for both the forward and backward detectors. The radiation lengths of the forward and backward crystals are 12 and 11, respectively.

The energy sum spectra for Bhabha events show a expected correlation between the forward and backward EFC detectors. A clear peak at 8 GeV with and rms resolution of 7.3% is seen for the forward EFC, while a clear peak at 3.5 GeV with an rms resolution of 5.8% for the backward EFC.

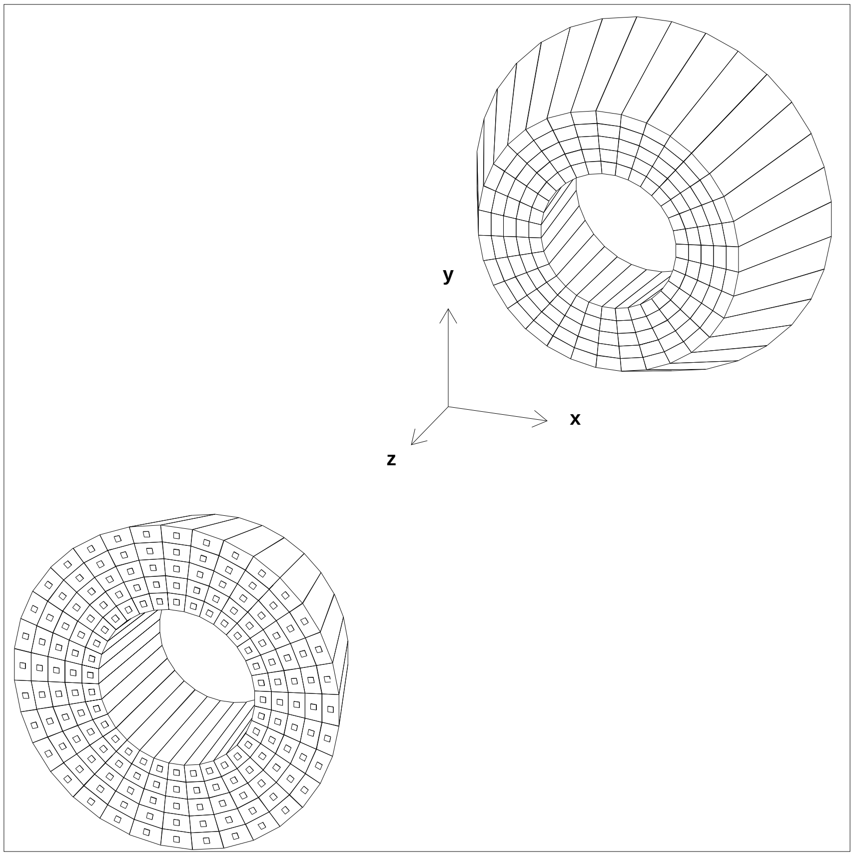

Figure 22: An isometric view of the BGO crystals of the forward and backward EFC detectors.

3.2.8 Solenoid Magnet

A superconducting solenoid provides a magnetic field of 1.5 T in a cylindrical volume of 3.4 m in diameter and 4.4 m in length [44]. The coil is surrounded by a multi-layer structure consisting of iron plates and RPCs as described in previous section. The iron structure of the Belle detector serves the return path of magnetic flux and an absorber material form KLM. It also provides the overall support for all of the detector components.

3.2.9 Trigger System (TRG)

The purpose of the trigger system is to reduce uninteresting events and to forward interesting ones to the Data Acquisition system. Many events seen by the detector are not the result of e^+e^- collision and should be ignored to save storage space and to reduce dead time. At an instantaneous luminosity of $10^{34}\text{cm}^{-2}s^{-1}$, the event rate of physical interest is around 100 Hz and the total rate is about 220 Hz as listed in Table 2. The rate of beam background events depends on the accelerator condition. The trigger now operates at around 400 Hz The background events come from interactions between the beams and the residual gas, interactions in the beam pipe, a synchrotron radiation and scattering of electrons (positrons) in beam bunch.

Table 2: Trigger rates expected from various sources at $\Upsilon(4S)$ and luminosity of 10^{34} $\text{cm}^{-2}s^{-1}$ [45, 46].

Source	Rate (Hz)
$\Upsilon(4S) \to B\bar{B}$	12
Hadron production from continuum	28
$e^+e^- \to \mu^+\mu^-$ and $e^+e^- \to \tau^+\tau^-$	16
$e^+e^- \to e^+e^-$ and $e^+e^- \to \gamma\gamma$ (prescaled by 100)	5
Two-photon process ($P_t > 0.3$ GeV/c)	35
Beam background	100
Cosmic ray	20

The Belle trigger system consists of the Level-1 hardware trigger and the Level-3 and Level-4 software trigger. (No Level-2 trigger.) The overall trigger efficiency for hadronic events from e^+e^- collisions is more than 99.5%.

Level-1 Trigger Figure 23 shows a schematic layout of the Level-1 trigger. This trigger consists of subdetector triggers governed by a central trigger system called Global Decision Logic (GDL) [46] which issues the Level-1 decision. The GDL receives subdetector triggers within 1.85 μs after the collision and issues a decision 2.2 μs after the collision. Subdetector triggers are based on tracking or energy information; the CDC and TOF trigger on charged particles; the ECL triggers on the energy deposit and the number of and timing of ECL cluster hits; the KLM triggers on muon hits; the EFC triggers on Bhabha ($e^+e^- \to e^+e^-$) and two photon ($e^+e^- \to \gamma\gamma$) events.

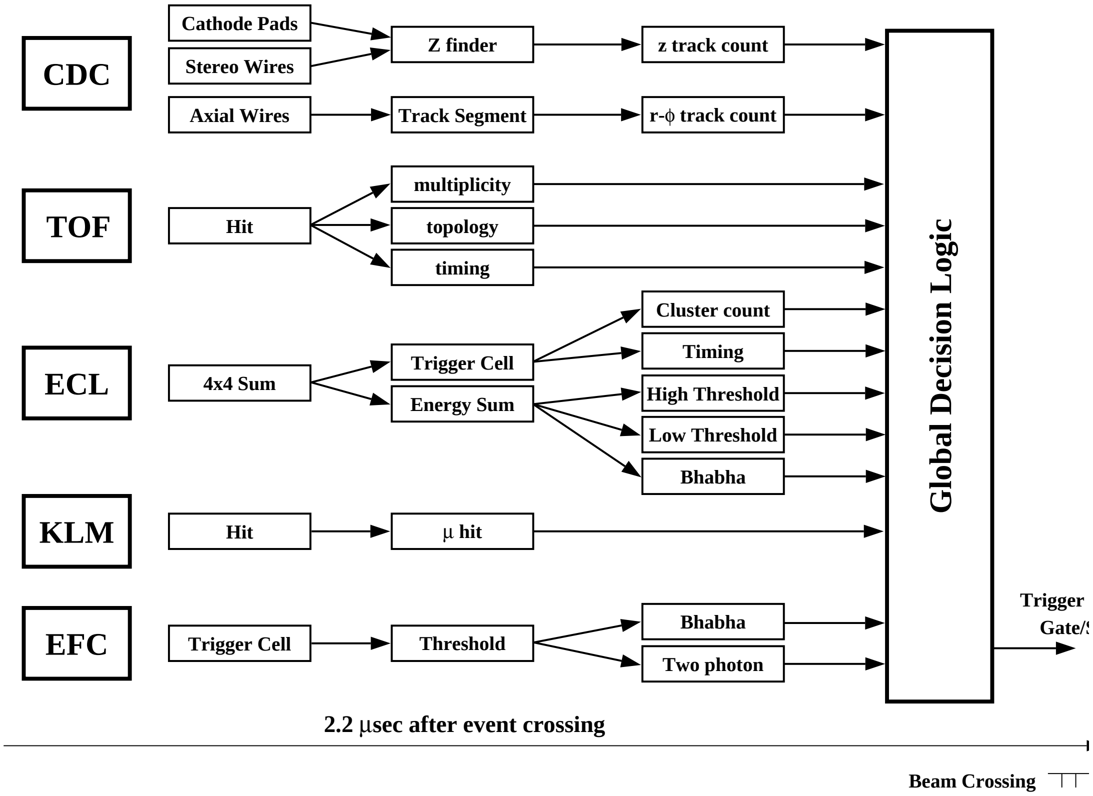

Figure 23: Schematic layout of the Level-1 trigger.

3.2.10 Data Acquisition System (DAQ)

When a Level-1 trigger is issued, the Data Acquisition system (DAQ) collects signal data from subdetectors and record them on the data storage system. As shown in Figure 24, the DAQ is a system running in parallel segmented in to 7 subsystems corresponding to the different subdetectors. The DAQ system [47] can work at ~ 600 Hz and now operate with ~ 2% deat time at 400 Hz of the Level-1 trigger. The main components of the DAQ are described in the following.

Digitizer The signal charges are converted to pulse width by Q-to-T converter modules and these timings are digitized by time-to-digital converters (TDC). For the KLM, only the timing information of the hits is recorded, hence a Q-to-T converter is not needed. For the SVD, the DSSDs are read out by on-bord chips and passed to Flash Analog-to-Digital Converters (FADC).

Readout sequence control system The sequence control system (SEQ) receives a timing signal from the GDL and distributes it to time distributer module located at the master VME crate of each detector readout system. The SEQ starts a readout sequence and digitized data are sent to event builder.

Event builder (EFARM) The event builder combines parallel data from all subdetetors into event-by-event data. The event is then sent to the online PC farm, which performs the Level-3 trigger. The Level-3 trigger system is a software trigger running on a Linux PC farm. It uses fast reconstruction and rejects events having no track with an impact parameter in z lower than 5 cm and less than 3 GeV energy deposit in the ECL. The event rate is reduced by about 50%.

Online computer farm (RFARM) The role of the online computer farm (RFARM) is to perform the event reconstruction at the same time as the data taking. The event filter (Level-4 trigger) is applied for background reduction before the full event reconstruction. The fully reconstructed data are stored in Data Summary Tapes (DST). The Level-4 filter requires events with more than 4 GeV of energy deposit in the ECL or with at least one track with a transverse momentum larger than 300 MeV/c and impact parameter less than 1cm in r and 4 cm in z. DST files are further filtered for specific physics purposes in a process called ’skimming’ and skimmed data are stored in Mini-DST (MDST) files which contain reduced information needed for analysis. The analysis presented in this thesis uses the Hadronic selection skims obtained with loose requirements to select B meson events (described in 4.3.1). The software for MDST production and the analysis is based on a C++ framework.

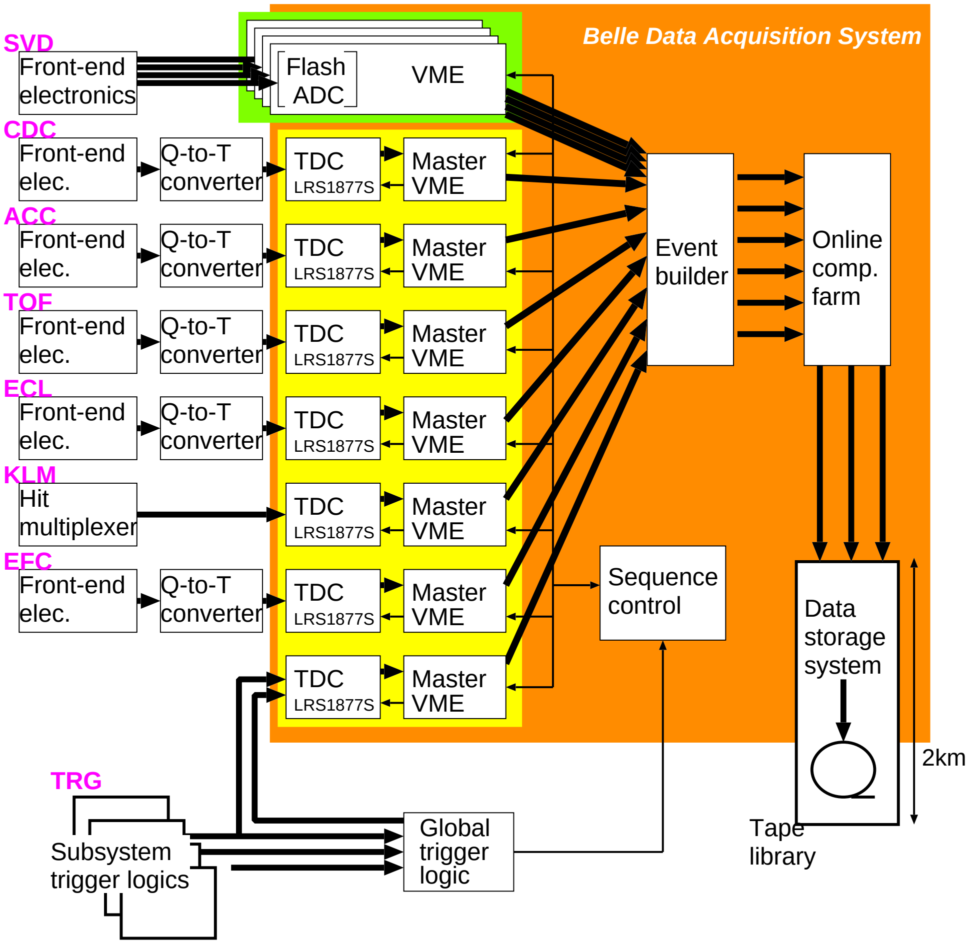

Figure 24: Overview of the Belle DAQ system.

4 Signal Reconstruction and Background Suppression

4.1 Analysis Overview

In this analysis, We reconstruct three signal modes $B^0 \to \rho^0\gamma$, $B^+ \to \rho^+\gamma$ and $B^0 \to \omega\gamma$, and two control samples $B \to K^{*0}\gamma$ and $B \to K^{*+}\gamma$. Charge conjugate modes are implicitly included unless otherwise stated. The following decay modes are used to reconstruct the intermediate states: $\rho^+ \to \pi^+\pi^0$, $\rho^0 \to \pi^+\pi^-$, $\omega \to \pi^+\pi^-\pi^0$, $K^{*+} \to K^+\pi^0$, $K^{*0} \to K^+\pi^-$, and $\pi^0 \to \gamma\gamma$. We start the analysis from the event passing the selection criteria for hadronic events ($B\bar{B}$ and continuum events). First, we select events including a high energy photon candidate which deposit large energy in ECL. We then form the ρ, ω and K^* candidates selecting charged pions and kaons and neutral pions. Charged pions and kaons are selected from charged tracks and separated by the particle identification based on information from dE/dx (CDC) and time of flight (TOF) and the number of photo electron of Cherenkov light (ACC). Neutral pions are formed from photon pairs. Then we combine a ρ, ω or K^* candidate with the high energy photon candidate to form a B candidate.

The main background source for this analysis comes from continuum events ($e^+e^- \to q\bar{q}(\gamma)$, $q = u, d, s, c$). To suppress the continuum background, we use a selection criteria making use of the difference of the event topology between B decays and continuum events. Events from $B\bar{B}$ decays containing K, π and photon are potential background to signal. We consider the following background from B decays: $b \to c$ decays, $b \to s\gamma$ modes (such as $B \to K^*\gamma$) and charmless rare B decays (including $B \to \rho\pi^0$,$\omega\pi^0$, $\rho\eta$ and $\omega\eta$). $B \to K^*\gamma$ modes are serious background source to $\rho\gamma$ modes because they are kinematicaly same as $\rho\gamma$ modes. Details of signal reconstruction and background suppression are described in this section. To estimate efficiencies for each event, we use Monte Carlo simulations described in this section. After reconstructing the signal candidates, we estimate signal yields and branching fractions. These procedures are described in section 5 and 6.

We improve the analysis compared with previous results [9]. In the previous analysis, a primary photon in the only barrel region of ECL was used. In this analysis, the barrel and end-cap photon are used. We then obtain 10% higher efficiency. We also improve the continuum suppression using additional information of ω meson for $B \to \omega\gamma$ mode. In addition, we improve the fitting procedure for $\rho^0\gamma$ and obtain 20(12)% higher efficiency(significance). The systematic error for these improvements are studied in this analysis.

4.2 Data set

The analysis is based on an on-resonance data sample of 606.5 fb^{-1} collected with the Belle detector by the end of 2006. The number of $B\bar{B}$ events ($N_{B\bar{B}}$) included in the data sample is estimated using the relation

$$N_{B\bar{B}} = N_{\text{on}} - \frac{\epsilon_{\text{on}}}{\epsilon_{\text{off}}}\frac{\mathcal{L}_{\text{on}}}{\mathcal{L}_{\text{off}}}N_{\text{off}}, \tag{29}$$

where N_{on} (N_{off}), ϵ_{on} (ϵ_{off}) and $\mathcal{L}_{\text{on}}$ ($\mathcal{L}_{\text{off}}$) are the number of hadronic events, the hadronic selection efficiency for $q\bar{q}$ event and the luminosity in the on-resonance (off-resonance) data, respectively. $N_{B\bar{B}}$ is evaluated to be

$$N_{B\bar{B}} = (657 \pm 9) \times 10^6 \tag{30}$$

We use Monte Carlo (MC) simulation for the study of the signal reconstruction, background estimation and so on. MC events are generated using an event generator called EvtGen. EvtGen is an event generator designed for the simulation of the physics processes of B decays. It is initially created by CLEO, and further developed and maintained by Babar. In MC samples for the specific B decays, the other B follow 'generic B decays', i.e. they decay through all possible $b \to c$ transition decays according to the branching fractions based on the PDG [48].

For the background study, we use continuum ($e^+e^- \to q\bar{q}; q = u, d, s, c$), $B^0\bar{B}^0$ and B^+B^- MC samples generated using an event generator PYTHIA [49]. We divide background from B decays to three categories; inclusive $b \to s\gamma$ modes, $b \to c$ decay modes and charmless rare B decays. The inclusive $b \to s\gamma$ MC samples are generated as an equal mixture of $s\bar{d}$ and $s\bar{u}$ quark pairs that are hadronized by PYTHIA. The mass spectrum of the X_s system follows the prediction by Kagan and Neubert [50]. In the $b \to c$ decay modes, both B mesons of $B^0\bar{B}^0$ and B^+B^- pairs follow 'generic B decays'. The charmless rare B decay MC contains $B \to PP, PV, VV$ and PS and $B \to p\bar{p}h$ ($h = K, \pi$), where P (pseudo-scaler) is either of π, K, η and η', V (vector) is either of ρ, K^*, ω and ϕ, and S (scaler) is either of $K_0^*(1430)$, $f_0(980)$, $f_0(1370)$ and $f_0(1500)$. The branching fractions are based on the central value or upper limit given in PDG [48].

For signal and control samples, we use $B \to \rho\gamma$, $B \to \omega\gamma$ and $B \to K^*\gamma$ MC samples. Table 3 shows the number of MC events or corresponding integrated luminosity for each components.

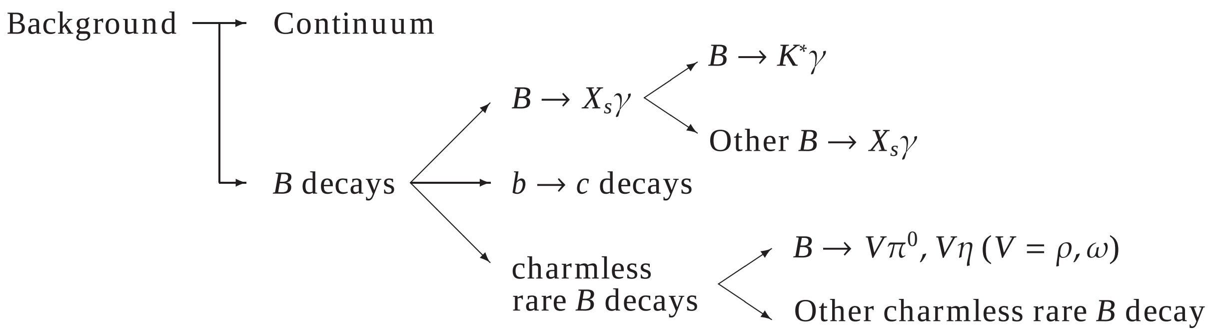

Table 3: The size of MC sample for each components.

Mode	size of MC sample	
$B^+ \to \rho^+\gamma$	0.8×10^6	Signal MC
$B^0 \to \rho^0\gamma$	0.8×10^6	
$B^0 \to \omega\gamma$	0.8×10^6	
$B^+ \to K^{*+}\gamma$	0.8×10^6	
$B^0 \to K^{*0}\gamma$	0.8×10^6	
$B \to X_s\gamma$	4.1×10^6	B decay background MC
$b \to c$ decay	1.8×10^3 fb^{-1}	
charmless rare B decays	12.5×10^3 fb^{-1}	
continuum	1.8×10^3 fb^{-1}	

4.3 Signal reconstruction

4.3.1 Hadronic event selection

Hadronic event selection is based on the variables constructed with ’good’ tracks, ’good’ clusters and ’good’ photons. ’Good’ tracks are defined as tracks with $p_t > 100$MeV/c which satisfy dr <2cm and $|dz|$ <4cm; where dr is the distance of closest approach to the nominal interaction point in the transverse (r-ϕ) plane and dz is a z-position of the closest point. The interaction point are determined using information of hadronic or Bhabha events by every 10000 events. ’Good’ clusters are defined as clusters in the ECL with energy greater than 100 MeV. ’Good’ photons are defined as good clusters that do not have associated tracks in the CDC. With these variables, we construct the following variables;

Track multiplicity:

$$N_{trk}$$

N_{trk} is the multiplicity of good tracks in an event.

z momentum balance:

$$P_z = (\sum_{goodtracks} \vec{p}_{\text{c.m.}} \sum_{goodphotons} \vec{p}_{\text{c.m.}}) \cdot \frac{\vec{z}}{|z|}$$

Visible energy:

$$E_{\text{vis}} = \sum_{goodtracks} \sqrt{p_{\text{c.m.}}^2 + m_\pi^2} + \sum_{goodphotons} E_{\text{c.m.}} \qquad (m_\pi \text{ is a pion mass.})$$

Calorimeter energy sum:

$$E_{\rm sum} = \sum_{goodclusters} E_{\rm c.m.} \qquad (17^\circ < \theta < 150^\circ)$$

where $p_{\rm c.m.}$ and $E_{c.m.}$ are the center-of-mass momentum and energy of particles. All tracks are boosted to the $\Upsilon(4S)$ rest frame assuming a pion mass and all clusters are boosted assuming zero mass.

The selection criteria for the hadronic events are as follows;

- An event has at least three tracks. $N_{trk} \geq 3$.
- $E_{\rm vis} \geq 0.2\sqrt{s}$, where $\sqrt{s}$ is the center-of-mass energy ($\sqrt{s} = 10.58$ GeV).
- The sum of the z components of each track's and photon's momenta is required to be balanced around zero: $|P_z| < 0.5\sqrt{s}$.
- $0.1 < E_{\rm sum}/\sqrt{s} < 0.8$, where $E_{\rm sum}$ is the sum of the energy of good clusters in the azimuthal region $17^\circ < \theta < 150^\circ$.
- Event primary vertex must be near the nominal IP for reduction of beam gas events: $r < 1.5$ cm and $|z| < 3.5$ cm.
- At least two good clusters are in the barrel region of ECL.
- Average good cluster energy is less than 1 GeV.
- Another energy sum cut $E'_{\rm sum} > 0.18\sqrt{s}$ is applied. In contrast to the $E_{\rm sum}$ used in 4th criterion, $E'_{\rm sum}$ includes all the clusters (barrel and end-cap) in the ECL.

4.3.2 Photon reconstruction

Photon candidates are reconstructed from isolated clusters in the ECL that have no corresponding charged track, and a shower shape that is consistent with that of photon. A photon with a center-of-mass (c.m.) energy in the range 1.8 GeV $< E^*_\gamma <$ 3.4 GeV is selected as the primary photon candidate. For the primary photon, we sum the energy deposited in arrays of 3×3 and 5×5 ECL cells around the maximum energy cell; if their ratio (E_9/E_{25}) is less than 0.95, the event is rejected. For hight energy π^0 produced by charge exchange ($n\pi^+ \to p\pi^0$), the two photon cluster sometimes overlap to each other and then E_9/E_{25} becomes small. Figure 25 shows the distributions of the E^*_γ and the E_9/E_{25} for signal and continuum MC events. To veto contributions from $\pi^0 \to \gamma\gamma$ and $\eta \to \gamma\gamma$, we calculate the invariant mass ($m_{\gamma_1\gamma_2}$) of primary photon (γ_1) and another photon (γ_2). The veto is applied on the likelihood ratio based on the $m_{\gamma_1\gamma_2}$ and energy of another photon The π^0 (η) veto criteria reject 49 (7)% of continuum background while retaining 96 (99)% of the signals.

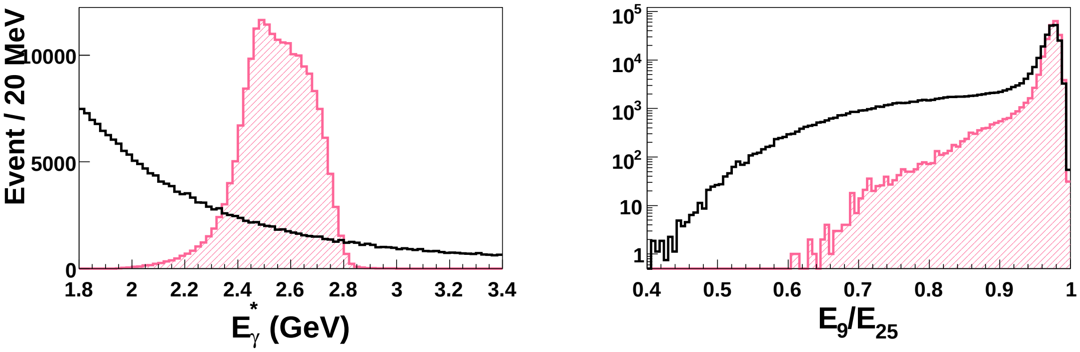

Figure 25: Distribution of E^*_γ (left) and E_9/E_{25}(right) for signal MC (hatched histogram) and $q\overline{q}$ MC (open histogram). Histogram for $q\overline{q}$ is normalized to have the same total number of events as signal histogram.

4.3.3 Neutral pion reconstruction

Neutral pions are formed from photon pairs with invariant masses within ± 16 MeV/c^2 of the nominal π^0 mass, corresponding to a $\sim$ 3 σ windows. The photon momenta are then recalculated with a π^0 mass constraint. We require the energy of each photon to be greater than 50 MeV in the ECL. We also require the cosine of the laboratory frame angle between the two photons (cos$\theta_{\gamma\gamma}$) to be greater than 0.58 (0.40) for the $B^+ \to \rho^+\gamma$ ($B^0 \to \omega\gamma$) mode in order to suppress combination with soft photons from backgrounds. Since π^0 from signal is boosted, $\theta_{\gamma\gamma}$ tends to be small.

4.3.4 Charged track reconstruction

Charged tracks are reconstructed using the CDC and SVD information. In order to reduce bad quality tracks and electrons from photon conversion in beam background event, we require that charged track for the signal reconstruction should satisfy dr <0.5 cm and $|dz|$ < 3cm. We also require their transverse momenta to be greater than 100 MeV/c. To separate pion and kaon, we use information from the number of photoelectrons(ACC), time-of-flight(TOF) and dE/dx(CDC). We determine the pion and kaon likelihood (L_π and L_K) based on the ACC, TOF and CDC information. We select pion and kaon by calculating likelihood ratio $\mathcal{R}_{PID} = L_K/(L_\pi + L_K)$. Pions are selected using criteria ($\mathcal{R}_{PID} < 0.3$) which have efficiencies of 86%, 87% and 89% for a pion from $B^+ \to \rho^+\gamma$, $B^0 \to \rho^0\gamma$ and $B^0 \to \omega\gamma$ modes, respectively. With these conditions, 8.3% and 8.5% of kaons are misidentified as pions in the $B^+ \to \rho^+\gamma$ and $B^0 \to \rho^0\gamma$ modes, respectively. In the $K^*\gamma$ modes, we select kaons ($\mathcal{R}_{PID} > 0.6$) with an efficiency of 85%.

4.3.5 ρ, ω reconstruction

We reconstruct ρ,ω and K^* in $\rho^+ \to \pi^+\pi^0$, $\rho^0 \to \pi^+\pi^-$, $\omega \to \pi^+\pi^-\pi^0$, $K^{*+} \to K^+\pi^0$ and $K^{*0} \to K^-\pi^+$ channels. Invariant masses for ρ, ω and K^* candidates are required to be within the windows of [0.64,0.89] GeV/c^2,[0.76,0.80] GeV/c^2 and [0.82,0.97] GeV/c^2 respectively. Figure 26 shows the invariant mass distributions for ρ, ω and K^*, respectively.

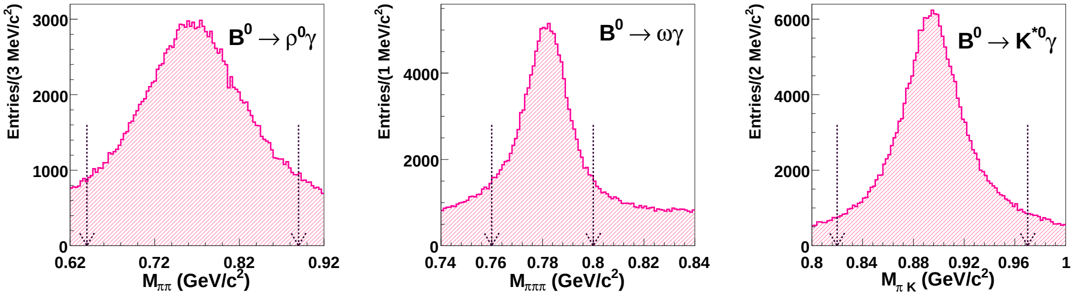

Figure 26: Invariant mass distributions of signal MC samples for ρ(left), ω(center) and K^*(right).

4.3.6 B reconstruction

We reconstruct B meson candidates by combining a ρ or ω candidate with the primary photon using two variables; the energy difference ΔE and the beam constrained mass $M_{\rm bc}$. These kinematic variables are defined in the c.m. frame as

$$M_{\rm bc} = \sqrt{(E^*_{\rm beam}/c^2)^2 - |\vec{p}^{\,*}_B/c|^2} \tag{31}$$

$$\Delta E = E^*_B - E^*_{\rm beam} \tag{32}$$

Here, $\vec{p}^{\,*}_B$ and E^*_B are the c.m. momentum and energy of the B candidate, and $E^*_{\rm beam}$ is the c.m. beam energy. To improve resolution, the magnitude of the photon momentum is replaced by $(E^*_{\rm beam} - E^*_{\rho/\omega})/c$ when the momentum $\vec{p}^{\,*}_B$ is calculated, because the momentum of charged particles and the beam energy are more precisely measured than the photon energy. Figure 27 and 28 show $M_{\rm bc}$ vs. ΔE scatter plot and their projections to $M_{\rm bc}$ and ΔE for signal and continuum MC samples. Signal events populate around $M_{\rm bc} = 5.28$ GeV/c^2 and $\Delta E = 0$ GeV, while continuum events distribute almost uniformly in $M_{\rm bc} < 5.29$ GeV/c^2. The signal region is defined as $|\Delta E| < 0.1$ GeV and 5.273 GeV/$c^2 < M_{\rm bc} < 5.285$ GeV/c^2; the wide region is defined as $|\Delta E| < 0.5$ GeV and 5.2 GeV/$c^2 < M_{\rm bc} < 5.3$ GeV/c^2. The wide region is used to determine the shape of the continuum events, because the signal and B decays background contribution is negligible in the region (except the signal region).

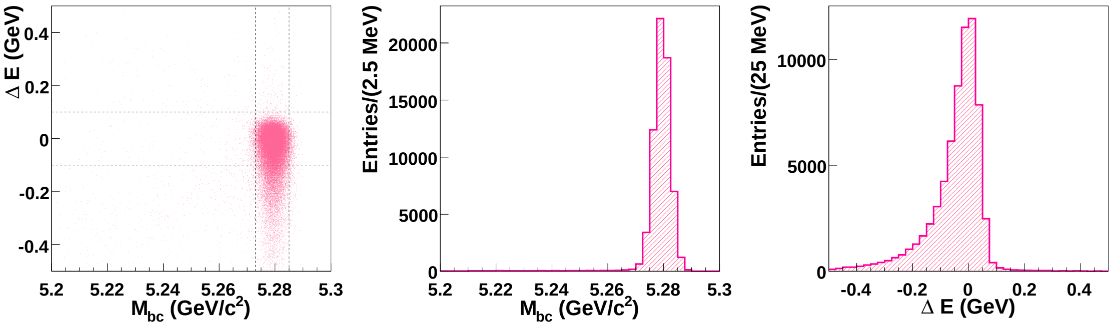

Figure 27: $M_{\rm bc}$ vs. ΔE scatter plot and their projections to $M_{\rm bc}$ and ΔE for signal MC samples. Lines show the signal region.

4.4 Background suppression

4.4.1 Continuum background

We reduce the continuum background events by exploiting the event topology; *i.e.* a continuum event is jet-like in the c.m. while $B\overline{B}$ event has a spherical topology due to the heavy mass of the B meson. To characterize the event topology, we use a

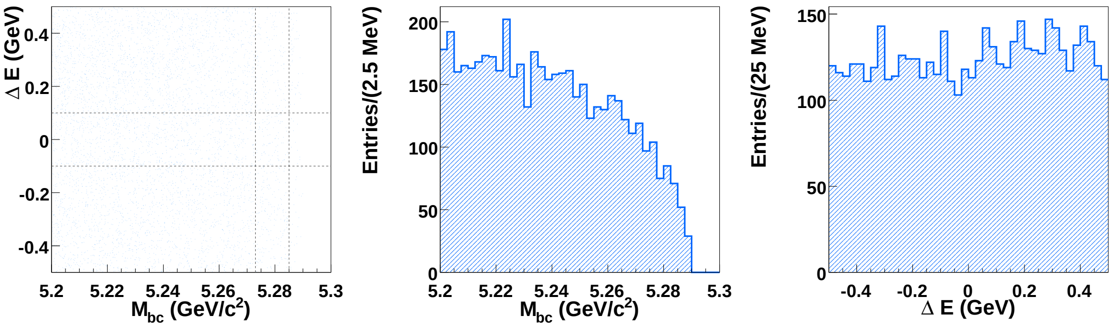

Figure 28: M_{bc} vs. ΔE scatter plot and their projections to M_{bc} and ΔE for continuum MC samples. Lines show the signal region.

variable calculated from modified Fox-Wolfram moments [51], called as KSFW [52]. The KSFW is a extension of a Fisher discriminant Super Fox-Wolfram [53] using more information such as missing mass. More detailed description on the KSFW can be found at Appendix A. In addition to the KSFW, we also use the variables; the cosine of the polar angle of the B meson direction in the c.m. frame ($\cos\theta_B^*$) and, for $B^0 \to \rho^0\gamma$, $B^0 \to \omega\gamma$ and $B^0 \to K^{*0}\gamma$ modes, the distance along z-axis (Δz) between the vertex of the signal candidate and that of the rest of the event. The B meson direction has the distribution with a dependence of $\sin^2\theta_B^*$, while continuum background events have a uniform distribution because of random combinations. Figure29 shows the Δz and $\cos\theta_B^*$ distributions for the signal MC and continuum background MC events. Two vertex points are coincident for the continuum background events. On the other hand, they are somewhat separated for the $B\overline{B}$ events in the laboratory frame along the z axis. For $B^0 \to \omega\gamma$, we calculate additional likelihood for the $\pi^+\pi^-\pi^0$ invariant mass ($M_{\pi^+\pi^-\pi^0}$) and the probability density from the $\pi^+\pi^-\pi^0$ Dalitz plot. Further descriptions are given in Appendix B. We use signal MC and background MC samples to determine the distributions of likelihood for these variables. To make use of full information, we calculate a likelihood ratio $\mathcal{R}$, defined as

$$\mathcal{R} = \frac{\mathcal{L}_S}{\mathcal{L}_S + \mathcal{L}_B} \quad (33)$$

$$\mathcal{L}_{S(B)} = \mathcal{L}_{S(B)}(KSFW) \times \mathcal{L}_{S(B)}(\cos\theta_B^*)[\times\mathcal{L}_{S(B)}^{1,2}(\Delta z)][\times\mathcal{L}_{S(B)}(M_{\pi^+\pi^-\pi^0}) \times \mathcal{L}_{S(B)}(\mathrm{Dalitz})] \quad (34)$$

where $\mathcal{L}_{S(B)}$ is the likelihood for signal(background), and calculated as a product of the likelihood for the KSFW, $\cos\theta_B^*$, Δz, $M_{\pi^+\pi^-\pi^0}$ and Dalitz probability density. For the Δz distribution, we calculate the likelihood ($\mathcal{L}_{S(B)}^1(\Delta z)$ and $\mathcal{L}_{S(B)}^2(\Delta z)$) separately for the SVD1 and SVD2 datasets, respectively, from the corresponding signal MC samples. The Δz likelihood is used if vertex information is available and $|\Delta z|$ is less than 0.2 cm. In addition, we use a tagging quality variable r that indicates the level of confidence in the B-flavor determination as described in Ref. [54]. Figure 30 shows the distribution of r and $\mathcal{R}$ for signal MC and $q\overline{q}$ MC events.

In the $(r, \mathcal{R})$ plane, signal tends to populate the region at $\mathcal{R} = 1$, while continuum background events populates the edges at $r = 0$ and $\mathcal{R} = 0$ as described in Figure 31. We divide the events into the six bins of r ([0,0.25], [0.25,0.5], [0.5,0.625], [0.625,0.75], [0.75,0.825], [0.825,1.0]) and determine the minimum $\mathcal{R}$ requirement for each bin. In the B^+ mode, if the tagging-side gives the same charge of the signal side, the events are assigned to the lowest bin [0,0.25] i.e. poor tagging quality.

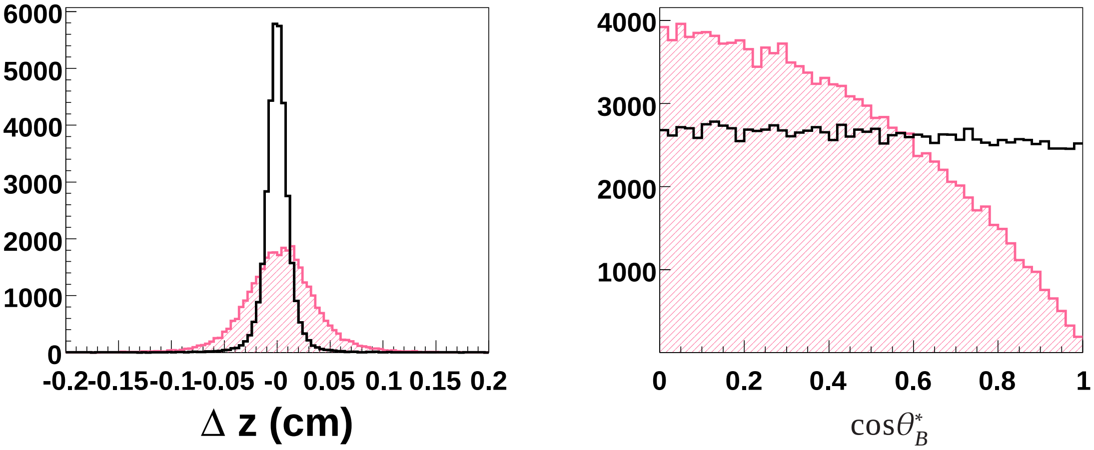

Figure 29: Distribution of Δz (left) and $\cos\theta^*_B$ (right) for signal MC (hatched histogram) and $q\overline{q}$ MC events (open histogram). Histogram for $q\overline{q}$ are normalized to have the same total number of events as signal histogram.

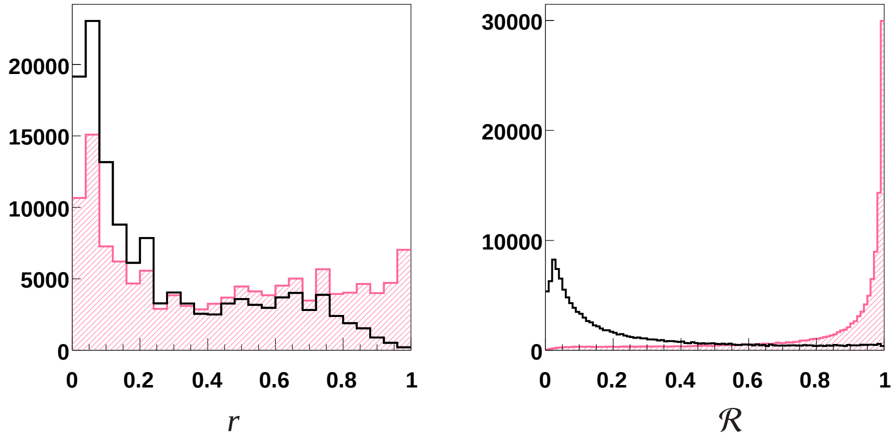

Figure 30: Distribution of r and R for signal MC (hatched histogram) and $q\overline{q}$ MC events (open histogram). Histogram for $q\overline{q}$ are normalized to have the same total number of events as signal histogram.

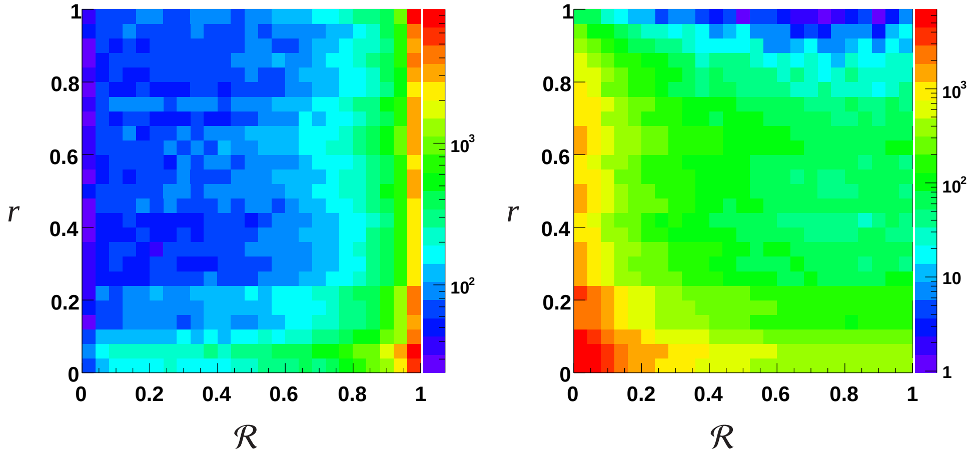

Figure 31: Signal(left) and continuum(right) populations of r vs $\mathcal{R}$.

4.4.2 B decay background

$K^*\gamma$ background
When the charged kaon is misidentified as a charged pion, $B^+ \to K^{*+}\gamma$ and $B^0 \to K^{*0}\gamma$ become serious background sources to $B^+ \to \rho^+\gamma$ and $B^0 \to \rho^0\gamma$, respectively. In this analysis, mainly charged particles have $\sim$ 1 GeV/c. ACC cover this momentum range. Charged kaon is misidentified as a pion, when kaon, having lower momentum than threshold, hits the ACC due to knock-on electron. $K^*\gamma$ events largely overlap with the corresponding signal events in the $M_{\rm bc}$-ΔE space. They also overlap in the $\pi\pi$ invariant mass distribution; here instead of using $M_{\pi\pi}$ a better $B \to K^*\gamma$ suppression can be achieved by using a "K"π mass ($M_{K\pi}$), which is the invariant mass of the $\pi\pi$ system when the kaon mass is assigned to (one of) the charged pion(s). The $B^0 \to \rho^0\gamma$ events are more severely affected than $B^+ \to \rho^+\gamma$ since the relative branching fraction ratio of $B \to \rho\gamma$ to $B \to K^*\gamma$ is smaller. For the $B^0 \to \rho^0\gamma$ mode, $M_{K\pi}$ is defined as the smaller invariant mass value of the two "K"π combinations. Figure32 shows the $M_{K\pi}$ distributions for signal and $K^*\gamma$ MC for B^0 and B^+.

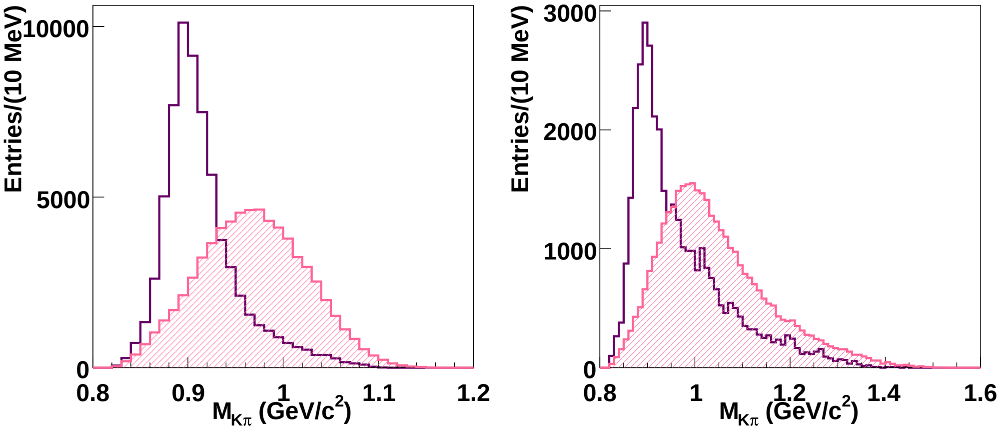

Figure 32: $M_{K\pi}$ distributions of signal MC (hatched histogram) and $K^*\gamma$ MC (open histogram) for B^0 (left) and B^+ (right). Histogram for $K^*\gamma$ is normalized to have the same total number of events as signal histogram.

There are also 'broken' $B \to K^*\gamma$ background where one of the pion is randomly picked up from the rest of the event instead of the kaon. To model the $B \to K^*\gamma$ background, we use an MC histogram which is normalized to the expected number of events based on the observed $B \to K^*\gamma$ branching fraction and the measured kaon to pion misidentification rate. The dominant part has a similar distribution as the $B \to \rho\gamma$ signal with a shifted ΔE, but the tail part is probably not identical. Contributions from $B^+ \to K^{*+}\gamma$ to $B^0 \to \rho^0\gamma$ and $B^0 \to \omega\gamma$, and those from $B^0 \to K^{*0}\gamma$ to $B^+ \to \rho^+\gamma$ are included in the other $B \to X_s\gamma$ background.

Other $X_s\gamma$ background

Similarly to the broken $B \to K^*\gamma$ background, other $B \to X_s\gamma$ events have a high energy photon, and it is rather easy to pick up pions that may form a ρ or ω. To avoid double counting, we removed the $B \to K^*\gamma$ component from an inclusive $B \to X_s\gamma$ sample, and form an MC histogram to model the background. The size is normalized according to the PDG branching fraction [48] ($B \to K^*\gamma$ contribution is subtracted) and the broken $K^*\gamma$ background as described above is added.

$B \to V\pi^0$ and $B \to V\eta$ background

The $B \to V\pi^0$ and $B \to V\eta$ modes, where V (vector meson) stands for either ρ^+, ρ^0 or ω, are serious background sources to the corresponding $B \to V\gamma$ signal modes when one of the photon from $\pi^0 \to \gamma\gamma$ or $\eta \to \gamma\gamma$ is unobserved or too soft to be rejected by the π^0/η veto condition. Since V ($J = 1$) decays to the spinless pions, V has the $\cos^2\theta_{\rm hel}$ helicity angle distribution in these backgrounds ($L_z = 0$) as oppose to the $1-\cos^2\theta_{\rm hel}$ for the signal ($L_z = 1$). Therefore the helicity angle requirement is very efficient. The $\theta_{\rm hel}$ is defined as the angle between the daughter π^+ direction and the B meson direction in the ρ meson rest frame; for $B \to \omega\gamma$ events, $\theta_{\rm hel}$ is defined as the angle between the normal to their decay plane and the B meson direction in the ω meson rest frame [48]. More detailed description on the $\theta_{\rm hel}$ can be found at Appendix C.

Furthermore, the ΔE peak is shifted to the negative side due to the missing photon. These backgrounds are modeled as histograms and normalized to the HFAG [55] branching fractions (or upper limits). Contributions from $B^+ \to V^+\pi^0$ and $B^+ \to V^+\eta$ to $B^0 \to \rho^0\gamma$ and $B^0 \to \omega\gamma$, and from $B^0 \to V^0\pi^0$ and $B^0 \to V^0\eta$ to $B^+ \to \rho^+\gamma$ are included in the other rare B decays.

Other Rare B Decays

The other rare decays (charmless B background) are in general small. To model this background for each of the signal modes, we form an MC histogram from the rare B MC sample, from which aforementioned decay modes are excluded.

Other B Decays

The generic ($b \to c$) B decay was neglected in the previous analysis [9] due to its small contribution. The contribution of this background is still small in this analysis, but becomes less negligible due to a looser set of $\mathcal{R}$ requirements. This background is also modeled by histograms with fixed normalizations.

4.5 Selection Optimization

We choose the selection criteria in Table 4 to maximize the figure of merit (FOM) defined as $N_S/\sqrt{N_S + N_B}$ in the signal region individually for each of the $B \to \rho\gamma$ and $B \to \omega\gamma$ modes. Here, N_S is the expected signal yield assuming the branching fractions based on 2006 Winter HFAG [55] and $N_{B\bar{B}} = 700 \times 10^6$, where we count the number of the signal MC events in the signal region after all the requirements are applied; N_B is the corresponding expected background yield from the number of counted MC events.

For the background yield, we use the sum of the background sources: continuum, $B \to K^*\gamma$, $B \to X_s\gamma$, and rare B decays: $B \to V(\pi^0, \eta)$ and other rare B. Other B decays are neglected. In the $\mathcal{R}$ optimization for the $B^0 \to \omega\gamma$ mode, only the continuum background is considered; other backgrounds are very small. Since the amount of the background MC events is limited when requirements are tightened, we use the number of background events in the wide region, and scale it by the fraction of events in the signal region calculated with no requirement on $\mathcal{R}$ and $q \cdot r$. We consider $\mathcal{R}_{PID}$, p_T of charged tracks, π^0/η veto, $\cos\theta_{\rm hel}$, $M_{\pi\pi}$, $M_{K\pi}$ and the likelihood ratio $\mathcal{R}$ in 6 r-bin in the optimization procedure. We first apply a loose set of requirements on the variables other than $\mathcal{R}$, and maximize FOM for $\mathcal{R}$. We apply this set of $\mathcal{R}$ requirements to optimize the variables other than $\mathcal{R}$ one by one as given in Table 4 (the $M_{K\pi}$ requirement for the $B^0 \to \rho^0\gamma$ mode is determined to be $M_{K\pi} > 0.92$ which is not used in the final selection criteria). Then we finalize the $\mathcal{R}$ requirements. The optimized set of 6 r-bin requirements are determined simultaneously to maximize the FOM using N_S and N_B summed over 6 bins. (Optimizing FOM for each bin does not always give the maximum for above quantity.)

The scanning points of $\mathcal{R}$ for the $q \cdot r$ bin are from 0.0 to 1.0 in a 0.01 step. The results of the optimization are listed in Table 5. The $\mathcal{R}$ criteria reject 98% of continuum background while retaining 35%, 51% and 43% of the $\rho^0\gamma$, $\rho^+\gamma$ and $\omega\gamma$ signals, respectively.

When the $B \to K^*\gamma$ modes are studied as the signal, we use the requirements for the corresponding $B \to \rho\gamma$ modes, except that we select a kaon instead of the pion, and we require that $M_{K\pi}$ is within the K^* resonance instead of vetoing them.

Table 4: Summary of the selection criteria.

Particle	Requirement
Photon	$1.8\ \mathrm{GeV} < E_\gamma < 3.4\ \mathrm{GeV}$
	π^0 veto: π^0 likelihood ratio < 0.40
	η veto: η likelihood ratio < 0.42
	$E_9/E_{25} > 0.95$
Charged tracks	$dr < 0.5$ cm
	$dz < 3$ cm
	$p_T > 100\ \mathrm{MeV}/c$
	$\mathcal{R}_{PID} < 0.3$ for π^- from ρ^-
	$\mathcal{R}_{PID} < 0.3$ for $\pi^\pm$ from ρ^0 and K^{*0}
	$\mathcal{R}_{PID} < 0.3$ for $\pi^\pm$ from ω
	$\mathcal{R}_{PID} \geq 0.6$ for $K^\pm$
π^0	Both $E_\gamma > 50$ MeV
	$\cos\theta(\gamma\gamma) > 0.58$ for π^0 from ρ^+
	$\cos\theta(\gamma\gamma) > 0.40$ for π^0 from ω
	$\lvert M(\gamma\gamma) - m_{\pi^0}\rvert < 16\ \mathrm{MeV}/c^2$
ρ^+	$M(\pi^+\pi^0)$ in $[0.64,\ 0.89]\ \mathrm{GeV}/c^2$
	$\lvert\cos\theta_{\mathrm{hel}}\rvert < 0.80$
	$M_{K\pi} > 0.92\ \mathrm{GeV}/c^2$
ρ^0	$M(\pi^+\pi^-)$ in $[0.64,\ 0.89]\ \mathrm{GeV}/c^2$
	$\lvert\cos\theta_{\mathrm{hel}}\rvert < 0.75$
	No $M_{K\pi}$ cut
ω	$M(\pi^-\pi^+\pi^0)$ in $[0.76,\ 0.80]\ \mathrm{GeV}/c^2$
	$\lvert\cos\theta_{\mathrm{hel}}\rvert < 0.83$
K^{*+}	$M(K^+\pi^0)$ in $[0.82,\ 0.97]\ \mathrm{GeV}/c^2$
	$\lvert\cos\theta_{\mathrm{hel}}\rvert < 0.70$
K^{*0}	$M(K^+\pi^-)$ in $[0.82, 0.97]\ \mathrm{GeV}/c^2$
	$\lvert\cos\theta_{\mathrm{hel}}\rvert < 0.70$
B signal region	$5.273\ \mathrm{GeV}/c^2 < M_{\mathrm{bc}} < 5.285\ \mathrm{GeV}/c^2$
	$-0.1\ \mathrm{GeV} < \Delta E < 0.1\ \mathrm{GeV}$
B wide region	$5.2\ \mathrm{GeV}/c^2 < M_{\mathrm{bc}}$
	$\lvert\Delta E\rvert < 0.5$ GeV
	$\mathcal{R}(\mathrm{KSFW}, \cos\theta^*_B(, \Delta z))$ for $\rho\gamma$
	$\mathcal{R}(\mathrm{KSFW}, \cos\theta^*_B(, \Delta z), M_{\pi^+\pi^-\pi^0}, \mathrm{Dalitz})$ for $\omega\gamma$
	$q \cdot r$ for B^+, modified standard six bins
	$\lvert q \cdot r\rvert$ for B^0, standard six bins

Table 5: Requirement on $\mathcal{R}$ for each $q \cdot r$ bin and yields for each component expected from MC simulation.

$q \cdot r$ (or $\lvert q \cdot r \rvert$)	$B^+ \to \rho^+\gamma$	$B^0 \to \rho^0\gamma$	$B^0 \to \omega\gamma$
-1 (0) — 0.250	0.99	0.97	0.99
$0.250 < q \cdot r \leq 0.500$	0.97	0.95	0.97
$0.500 < q \cdot r \leq 0.625$	0.95	0.92	0.97
$0.625 < q \cdot r \leq 0.750$	0.94	0.94	0.94
$0.750 < q \cdot r \leq 0.875$	0.89	0.91	0.94
$0.875 < q \cdot r \leq 1.000$	0.66	0.61	0.79
N_S	54.6	66.6	16.3
N_{cont}	74.9	91.8	29.6
$N_{K^*\gamma}$	17.9	38.7	ignored
$N_{X_s\gamma}$	2.0	2.3	ignored
N_{rare}	9.1	5.5	ignored
FOM	4.33	4.15	2.41

5 Signal Extraction

For the signal extraction, we perform a two-dimensional (three-dimensional for $\rho^0\gamma$) unbinned extended maximum likelihood fit to $M_{\rm bc}$ and ΔE ($M_{\rm bc}$, ΔE and $M_{K\pi}$) distribution using the probability density functions (PDF) described below. The likelihood is defined as

$$\mathcal{L} = \exp\left(-\sum_j N_j\right)\prod_i\left(\sum_j N_j P_j^i\right), \tag{35}$$

where i runs over all events, j runs over the possible event categories (signal and background), N_j is the number of events in each category and P_j is the corresponding PDF. For signal modes and continuum events, we use an analytic functions as PDFs described below. For the B decay backgrounds, PDFs are based on a MC histogram and normalizations are determined using measured branching fractions [48]. We calibrate the PDFs for signal modes using $K^*\gamma$ data sample. For $K^*\gamma$ modes, we carefully calibrate the PDFs using enriched $K^*\gamma$ background data sample because the distribution affects to signal yields. The normalization of $K^*\gamma$ background are carefully estimated using the $K^*\gamma$ control samples. The PID efficiency and misidentification probability for charged tracks are also studied using $D^{*+} \to D^0\pi^+(D^0 \to K^-\pi^+)$ data and MC samples (See Appendix F.2).

5.1 Signal modeling

5.1.1 Functions for signal modeling

For each of the signal modes $B^+ \to \rho^+\gamma$, $B^0 \to \rho^0\gamma$ and $B^0 \to \omega\gamma$, we model the signal component as the product of $M_{\rm bc}$ function and ΔE function over the $M_{\rm bc}$-ΔE space. We use a Gaussian function

$$f_G(x) = \frac{1}{\sqrt{2\pi}\sigma}\exp\left[-\frac{(x-\mu)^2}{2\sigma^2}\right] \tag{36}$$

to model $M_{\rm bc}$ distribution for $B^0 \to \rho^0\gamma$ and $B^0 \to K^{*0}\gamma$ (modes without π^0). For the modes with a π^0, we use a Crystal Ball function (CB) [56] in order to describe the tail in the lower side of the peak.

The Crystal Ball function has the following form,

$$f_{\rm CB}(x) = \begin{cases} A\exp\left[-\frac{1}{2}\frac{(x-\mu)^2}{\sigma^2}\right] & (\text{if } x \geq \mu + \alpha\sigma) \\ Ae^{-\frac{\alpha^2}{2}}\left[1-\frac{\alpha^2}{n}\left(1-\frac{x-\mu}{\alpha\sigma}\right)\right]^{-n} & (\text{if } x < \mu + \alpha\sigma) \end{cases} \tag{37}$$

where σ and μ correspond to the width and mean of a Gaussian function that is used to model the higher side, and α and n are empirical parameters to model the lower side. The Crystal Ball function is also used to model ΔE distributions for all modes.

Figure 33 shows the CB function distributions for each n and α, respectively, when (μ,σ) is fixed to (0.0, 1.0).

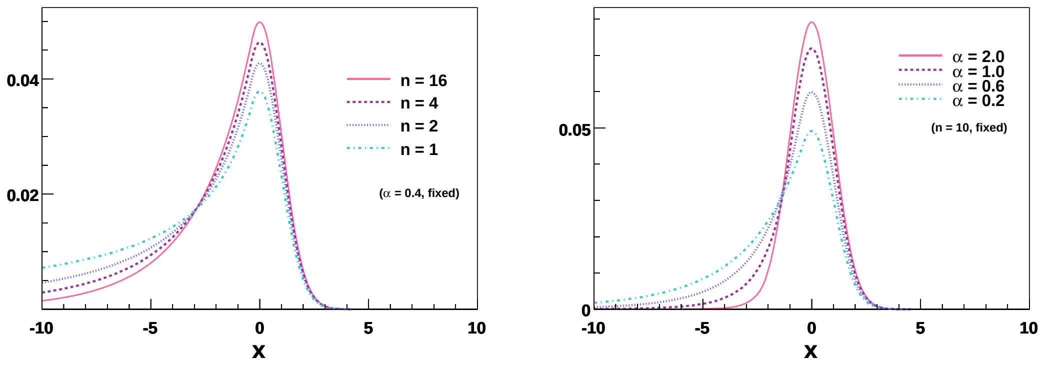

Figure 33: The CB function distributions for each n(left) and α(right).

5.1.2 Signal shape parameters

In advance of the fitting data for the signal yield extraction, we determine all the signal shape parameters in Eq. (36) and Eq. (37). There are six parameters for the $\rho^0\gamma$ mode, and eight parameters for each of the $\rho^+\gamma$ and $\omega\gamma$ modes. Before the determination of the parameters using MC and data samples, we study the effect of the photon energy shift in data taking periods. We have found measured photon energy shifted for the data taken after January 2004 (corresponding to 446 fb^{-1}) [3] In this analysis, it causes the shift in ΔE distribution in $B^0 \to K^{*0}\gamma$ control sample for the data taken after January 2004 with -6.7 ± 2.7 MeV. We shift the ΔE by -6.7 MeV for this data sample to correct the effect (referred to as 'energy-shift', See Appendix D for detail).

The parameters for the $B^0 \to \rho^0\gamma$ mode are determined from the $B^0 \to K^{*0}\gamma$ data sample. Those for the $B^+ \to \rho^+\gamma$ and $B^0 \to \omega\gamma$ modes are first determined by the signal MC samples and calibrated using $B^+ \to K^{*+}\gamma$ data and MC samples. The detailed procedure is described in Appendix E. Table 6 shows the parameter sets for the nominal fit.

---

[3] This could be caused by change of PMT gain or response of ECL.

Table 6: Shape parameters of the signal ΔE and $M_{\rm bc}$ for the nominal fit. A number in a bracket indicates that the corresponding parameters is determined using MC samples.

	n	α	μ (MeV/c^2)	σ (MeV/c^2)
[ΔE] for $\omega\gamma$	[14.1]	[0.49]	$2.8^{+3.0}_{-3.1}$	41.5 ± 2.1
[ΔE] for $\rho^+\gamma$	[14.8]	[0.52]	$0.1^{+2.9}_{-3.0}$	$43.7^{+2.2}_{-2.1}$
[ΔE] for $\rho^0\gamma$	$6.39^{+4.93}_{-2.03}$	$0.65^{+0.09}_{-0.08}$	4.1 ± 2.4	36.9 ± 1.8
[$M_{\rm bc}$] for $\omega\gamma$	[2.13]	[1.63]	5279.6 ± 0.14	$2.81^{+0.12}_{-0.11}$
[$M_{\rm bc}$] for $\rho^+\gamma$	[1.81]	[1.57]	5279.13 ± 0.14	2.82 ± 0.12
[$M_{\rm bc}$] for $\rho^0\gamma$	—	—	5279.7 ± 0.06	2.63 ± 0.04

5.2 Signal Extraction Procedure for $B^+ \to \rho^+\gamma$ and $B^0 \to \omega\gamma$

We use the two-dimensional unbinned extended maximum likelihood fit to extract the signal yield from $M_{\rm bc}$ and ΔE distributions for the $B^+ \to \rho^+\gamma$ and $B^0 \to \omega\gamma$ modes. For the $B^0 \to \rho^0\gamma$ mode, we use a three-dimensional fit which is described in the next section.

5.2.1 Probability Density Function for the 2D Fit

Table 7 summarizes PDFs used for the 2D fit. We use a Crystal Ball function to model both of the ΔE and $M_{\rm bc}$ shapes of the signal. The continuum background shape is modeled with the product of an ARGUS function [57] and a linear function. Figure 34 show distribution of $M_{\rm bc}$ and ΔE using sideband data. All the other distributions are modeled with 40×40 two-dimensional MC histograms.

Most dangerous background comes from $B \to K^*\gamma$ modes. We have to be careful to model the ΔE distribution of the $K^{*+}\gamma$ background component in the $B^+ \to \rho^+\gamma$ analysis, because ΔE is a main variable to discriminate the $\rho^+\gamma$ and $K^{*+}\gamma$ component and small gap of ΔE of $K^{*+}\gamma$ affect extraction of the $\rho^+\gamma$ signal, while, in general, we can use MC histograms to model the background component because small shift in $M_{\rm bc}$ or ΔE distribution between data and MC is expected to give negligible bias in the fit. Therefore, we calibrate the ΔE gap using a enriched $K^{*+}\gamma$ background data sample. To make this enriched $K^{*+}\gamma$ sample, we apply the opposite PID criterion to the charged particle in the $\rho^+\gamma$ reconstruction and positively select the K^* component by requiring $M_{K\pi} < 0.92$ GeV instead of $M_{K\pi} > 0.92$ GeV . To obtain the ΔE gap between data and

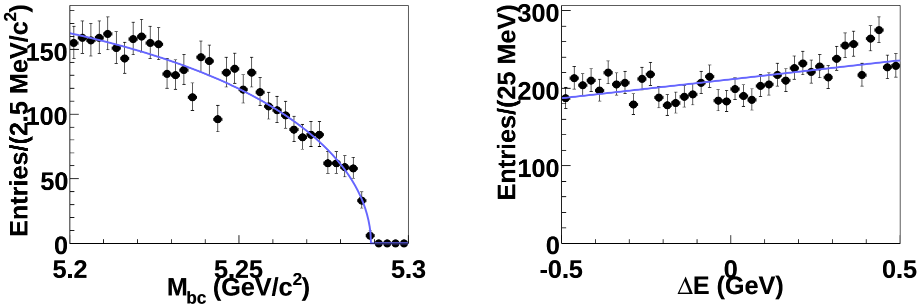

$$f_{\text{ARGUS}}(x) = x\sqrt{1-(\frac{x}{E_{\text{beam}}})}\exp(c(1-(\frac{x}{E_{\text{beam}}})^2)) \quad \text{(c: shape parameter)}$$

Figure 34: The M_{bc} distribution with $0.1 < \Delta E < 0.5$ (left) and the ΔE distribution with $5.2 < M_{\text{bc}} < 5.27$ (right). Solid line show ARGUS function for M_{bc} and linear function for ΔE.

Table 7: PDFs for each component in the 2D fit of $B^+ \to \rho^+\gamma$ and $B^0 \to \omega\gamma$.

Component	M_{bc}	ΔE
$B^+ \to \rho^+\gamma$ / $B^0 \to \omega\gamma$	Crystal Ball	Crystal Ball
$q\overline{q}$	ARGUS	1st order Chebyshev
$B^+ \to K^{*+}\gamma$ (for $B^+ \to \rho^+\gamma$)	2D histogram PDF	
$X_s\gamma$	2D histogram PDF	
$V\pi^0$	2D histogram PDF	
$V\eta$	2D histogram PDF	
Rare B	2D histogram PDF	
$B\overline{B}$	2D histogram PDF	

MC sample, we fit the ΔE distribution of this sample with the PDF from MC histograms where ΔE is shifted by some amount, and calculate the likelihood. From a scan of the likelihood as a function of the ΔE shift, we obtain the ΔE gap to be 5.1 ± 2.2 MeV, and we shift the ΔE value by 5.1 MeV when we produce two-dimensional histogram PDFs from $K^{*+}\gamma$ MC sample. Figure 35 shows the fit result of the enriched $K^{*+}\gamma$ background data sample.

In the fit, we fix the normalization of all B decay backgrounds. The floated parameters are the signal and continuum background yields, and shape parameter of $f_{\text{ARGUS}}(M_{\text{bc}})$ and slope of linear function (for ΔE) for the continuum PDF.

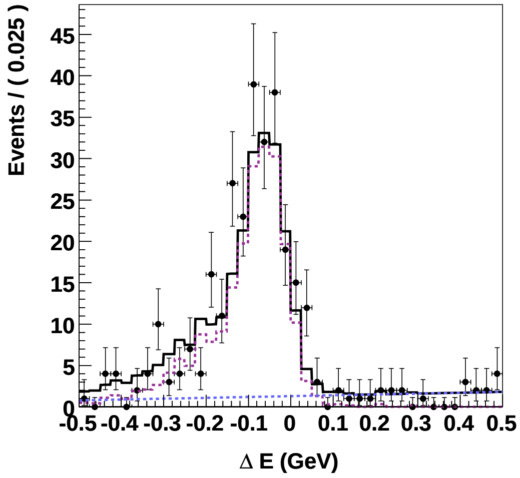

Figure 35: The ΔE distribution of the enriched $K^{*+}\gamma$ background data sample. Solid histogram shows fit results (Dotted histogram is a $K^{*+}\gamma$ background component and dotted line is other background).

5.3 Signal Extraction Procedure for $B^0 \to \rho^0\gamma$

Including more variable that separate the signal and the background in a fit, we can reduce the statistical error. One of the candidates of such variable is $M_{K\pi}$, which is useful to discriminate $B \to \rho\gamma$ signal from $B \to K^*\gamma$ background. We have studied the correlation between variables and bias in the fit results using MC samples. We have compared the input number of signal event with the number of fit results and found the correlation and bias are negligible. After the study, we decided to include $M_{K\pi}$ in the fit and perform three-dimensional fit to $M_{\rm bc}$-ΔE-$M_{K\pi}$ distribution for $B^0 \to \rho^0\gamma$, to effectively separate the large contamination from $B^0 \to K^{*0}\gamma$ background. The 3D fit gives about 20% higher efficiency than a 2D fit and increases significance by 12% according to MC study.

5.3.1 Probability Density Function for the 3D Fit

Table 8 summarizes the PDFs for all the components in the 3D fit. For the $B^0 \to \rho^0\gamma$ signal component, we use a Gaussian function to model the $M_{\rm bc}$ distribution and a Crystal Ball function to model ΔE distribution. The continuum background shape is modeled with the product of an ARGUS function and a linear function. All the other distributions are modeled with 40×40 two-dimensional MC histograms in the $M_{\rm bc}$-ΔE space. We use one-dimensional MC histogram to model $M_{K\pi}$ distribution. Histograms for $M_{K\pi}$ are smoothed to avoid null-entry at high $M_{K\pi}$ region.

Similar to the $B^+ \to \rho^+\gamma$ case, the ΔE PDF of the $K^{*0}\gamma$ background component is shifted by the amount determined using the enriched $K^{*0}\gamma$ background data sample. The shift is calculated to be 5.6 ± 1.5 MeV. Figure 36 shows the fit result of the enriched

Table 8: PDFs for each component in the 3D fit of $B^0 \to \rho^0\gamma$.

Component	$M_{\rm bc}$	ΔE	$M_{K\pi}$
$B^0 \to \rho^0\gamma$	Gaussian	Crystal Ball	Smoothed histogram PDF
$q\bar{q}$	ARGUS	Polynomial	Smoothed histogram PDF
$B^0 \to K^{*0}\gamma$	2D histogram PDF		Smoothed histogram PDF
$X_s\gamma$	2D histogram PDF		Smoothed histogram PDF
$V\pi^0$	2D histogram PDF		Smoothed histogram PDF
$V\eta$	2D histogram PDF		Smoothed histogram PDF
Rare B	2D histogram PDF		Smoothed histogram PDF
$B\bar{B}$	2D histogram PDF		Smoothed histogram PDF

$K^{*0}\gamma$ data sample.

The normalization of all B decay backgrounds are fixed according to the MC expectation. The floated parameters are the signal and continuum background yields, and two shape variables for the continuum PDF.

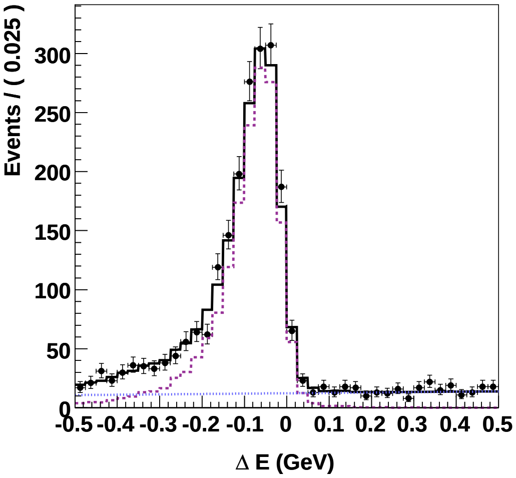

Figure 36: The ΔE distribution of the enriched $K^{*0}\gamma$ background data sample. Solid histogram shows fit results (Dotted histogram is a $K^{*0}\gamma$ background component and dotted line is other background).

5.4 Signal Efficiency

We estimate the reconstruction efficiencies for the signal ($B^+ \to \rho^+\gamma$, $B^0 \to \rho^0\gamma$ and $B^0 \to \omega\gamma$) and the control sample ($B^+ \to K^{*+}\gamma$ and $B^0 \to K^{*0}\gamma$) from corresponding MC samples. The MC efficiency for each mode is defined as the fraction of the signal remaining after all selection criteria are applied, where the signal yield is determined

Table 9: Summary of efficiencies and their systematic errors. The sub-decay $\mathcal{B}(\omega \to \pi^+\pi^-\pi^0)$ is included for the $\omega\gamma$ mode.

Source	Fractional error (%)		
	$\rho^+\gamma$	$\rho^0\gamma$	$\omega\gamma$
Photon detection	2.4	2.4	2.4
Track reconstruction	1.0	2.0	2.0
π^0 reconstruction	4.6	-	4.6
Particle-ID	0.5	1.1	1.1
π^0/η veto and $\mathcal{R}$	3.1	2.3	8.4
MC statistics	0.56	0.42	0.48
Fit Bias	4.5	5.1	5.4
$\mathcal{B}(\omega \to \pi^+\pi^-\pi^0)$	-	-	0.79
Total	7.3	6.4	11.5
Efficiency (%)	8.03 ± 0.59	14.81 ± 0.95	6.58 ± 0.76

from a fit to the sum of the signal and continuum MC samples and then corrected for the fitting bias that is described in Appendix F. For the particle identification, we also make corrections to the total reconstruction efficiency since we know that the data efficiency deviates from MC efficiency. Then, we calibrate the MC efficiency with control data sample and assign the systematic errors for categories. We use the Belle standard value for the photon detection, track reconstruction, π^0 reconstruction and particle-ID. In this analysis, we study systematic uncertainties for an end-cap photon detection, a π^0/η veto and $\mathcal{R}$ requirement and a fit bias. The systematic error on the photon detection efficiency is estimated in Ref. [66]. However, this study only considered photons in the barrel region. Because we include endcap photons for the primary photon candidates in this analysis, we perform additional study to estimate a systematic error for the endcap photons. We compare the yield ratio of the events with an endcap photon to those with a barrel photon between data and MC using the $B^0 \to K^{*0}\gamma$ control sample. (for detail, see Appendix G.3) For the combined efficiency for the π^0/η veto and $\mathcal{R}$ requirement, we use a $B \to D\pi$ control sample. We compare cut efficiency for data with those for MC sample. We also study a possible bias in the 2D(3D) fitting procedure using MC samples. The detail for each item is described in the Appendix G.

Here, we list the source of efficiency systematic errors in Table 9.

6 Results

6.1 Branching Fractions

Figure 37 shows the 2D fit results for $B^+ \to \rho^+\gamma$ and $B^0 \to \omega\gamma$, and Figure 38 shows the 3D fit result for $B^0 \to \rho^0\gamma$. We obtain the signal yields $45.8\,^{+15.2}_{-14.5}$, $75.7\,^{+16.8}_{-16.0}$ and $17.5\,^{+8.2}_{-7.4}$ for $\rho^+\gamma$, $\rho^0\gamma$ and $\omega\gamma$ respectively.

For $\rho\gamma$ modes, main source of systematic error is $K^*\gamma$ background. The systematic errors due to kaon fake rate and ΔE gap of $K^*\gamma$ background are dominant. The systematic error of normalization of $B \to V\pi^0$ ($V = \rho, \omega$) are also significance. For $\rho^+\gamma$ and $\omega\gamma$, systematic error due to the shape parameters of signal PDFs (Crystal Ball function) are not small. In order to estimate systematic errors in the fit procedure, we vary various fixed parameters one by one, and regard the deviation from the nominal value as an error. The signal shape parameters μ and σ for both $M_{\rm bc}$ and ΔE are varied by the amounts listed in Table 6. For n and α of the Crystal Ball function, we use alternative sets of (μ,σ,n,α) to estimate possible bias in n and α (See Appendix E). For ΔE, we also vary the amount of the energy-shift (see Appendix D) data on by $\pm 1\sigma$. For each new ΔE shift value, we recalculate the signal shape parameters and ΔE shift in $K^*\gamma$ PDF using the same procedure in the nominal case. Another test is about the amount of the shift of $K^*\gamma$ background PDF between MC and data. This is also varied by $\pm 1\sigma$ for $\rho\gamma$ modes. Fixed background normalizations are varied according to Table 10. In case only upper limit has been measured, we take a half of the upper limit value as the nominal value and assume 100% error. We assume 15% and 50% error for other rare B decays and $b \to c$ decays, respectively. Table 11 lists the deviation of the yield from the nominal value in each step. The positive (negative) deviations are summed up in quadrature to calculate the total systematic errors. The statistical significance without the effect of the systematic error is calculated by the formula $\sqrt{2(\ln\mathcal{L}_{\rm max} - \ln\mathcal{L}_0)}$, where $\mathcal{L}_{\rm max}$ and $\mathcal{L}_0$ are the maximum likelihood of the nominal fit and the fit when the signal yield is fixed to zero. In order to include the effect of the systematic error in the significance calculation, we use the convolution method. We convolve the likelihood function with a Gaussian as

$$\mathcal{L}'(x) = \frac{1}{\sqrt{2\pi}\sigma}\int_{-\infty}^{+\infty} \mathcal{L}(t)e^{-(t-x)^2/(2\sigma^2)}dt, \tag{38}$$

where x is the signal yield for which the likelihood is evaluated and σ is the systematic error. In the actual calculation, we use asymmetric Gaussian to treat different systematic error in positive and negative sides. We then calculate the significance including the systematic error by $\sqrt{2(\ln\mathcal{L}'_{\rm max} - \ln\mathcal{L}'_0)}$.

Figure 39 shows the distribution of the likelihood before and after the convolution. The significances of $B^+ \to \rho^+\gamma$, $B^0 \to \rho^0\gamma$, $B^0 \to \omega\gamma$ are calculated to be 3.2 , 4.9 and 2.6, respectively with the systematic error.

Using the efficiencies listed in Table 12, we obtain the branching fractions

$$\mathcal{B}(B^+ \to \rho^+\gamma) = (0.87\,^{+0.29}_{-0.27}\,^{+0.09}_{-0.11}) \times 10^{-6}, \tag{39}$$

$$\mathcal{B}(B^0 \to \rho^0\gamma) = (0.78\,^{+0.17}_{-0.16}\,^{+0.09}_{-0.10}) \times 10^{-6}, \tag{40}$$

$$\mathcal{B}(B^0 \to \omega\gamma) = (0.40\,^{+0.19}_{-0.17} \pm 0.13) \times 10^{-6}. \tag{41}$$

The branching fraction and the systematic error are calculated by the formula

$$\mathcal{B} = \frac{N_{sig}}{N_{B\bar{B}} \times \epsilon} \qquad \text{and} \qquad \sigma_{\mathcal{B}} = \mathcal{B}\sqrt{\left(\frac{\sigma_{N_{syst.}}}{N_{sig.}}\right)^2 + \left(\frac{\sigma_\epsilon}{\epsilon}\right)^2 + \left(\frac{\sigma_{N_{B\bar{B}}}}{N_{B\bar{B}}}\right)^2}, \tag{42}$$

where N_{sig} is the signal yield obtained by fit, ϵ is the efficiency and $\sigma_{N_{syst.}}$ is the fitting systematic error. We assume equal number of neutral and charged B pairs.

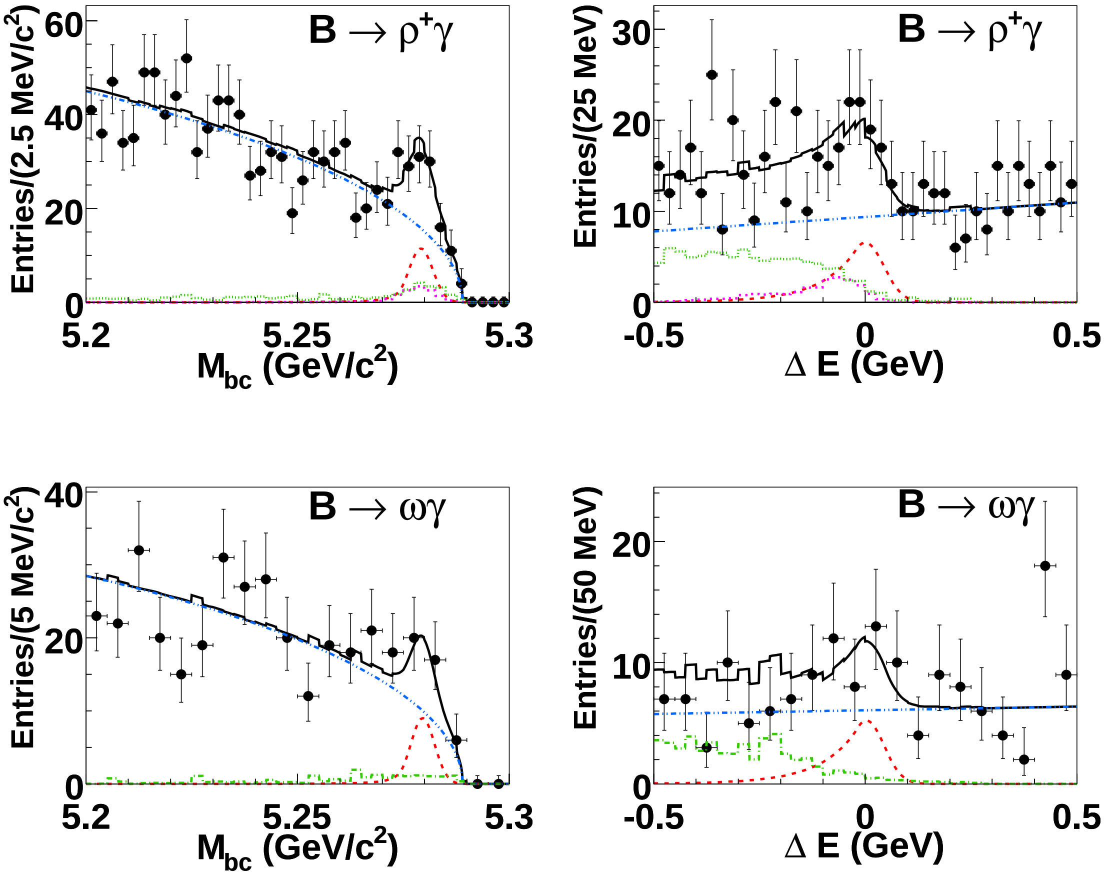

Figure 37: Projections of the fit results to $M_{\rm bc}$ (in $|\Delta E| < 0.1$ GeV) and ΔE (in $5.273\ {\rm GeV}/c^2 < M_{\rm bc} < 5.285\ {\rm GeV}/c^2$). Curves show the signal (dashed, red), continuum (dot-dot-dashed, blue), $B \to K^*\gamma$ (dotted, magenta), other backgrounds (dash-dotted, green), and the total fit result (solid).

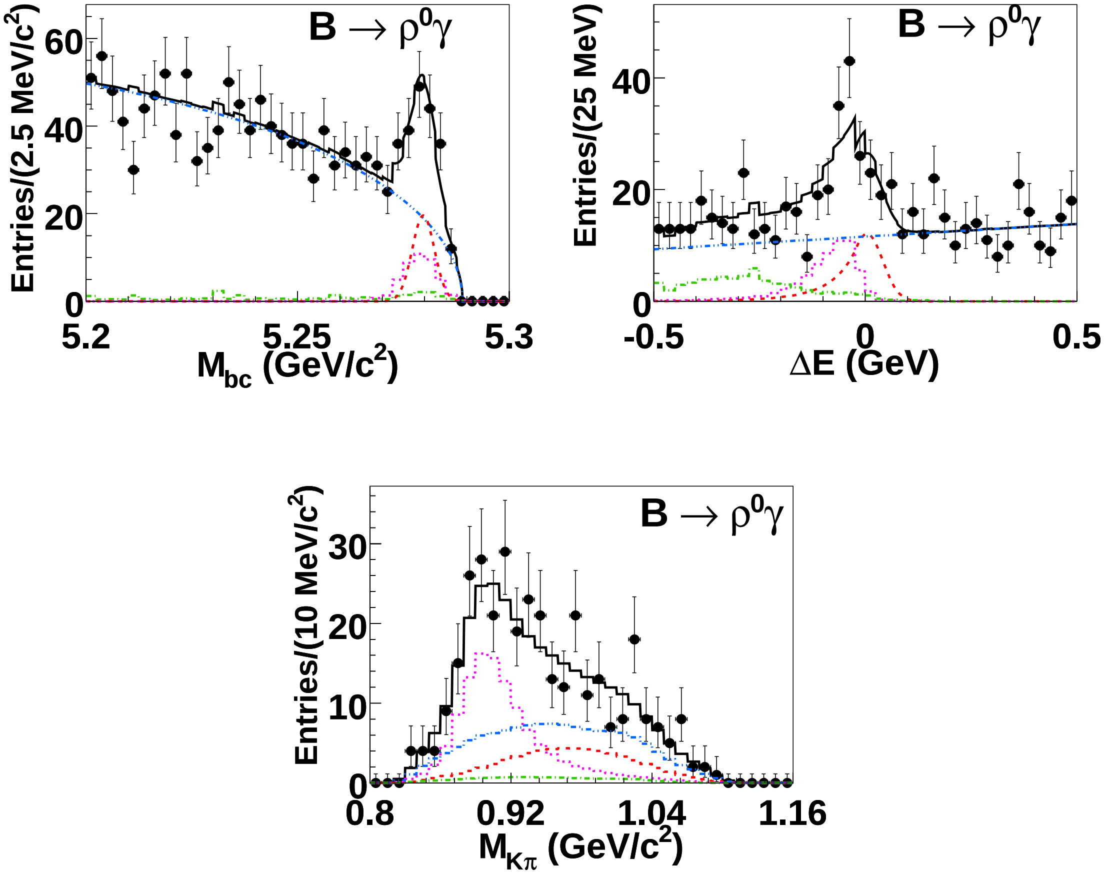

Figure 38: Projections of the fit results to $M_{\rm bc}$ (in $|\Delta E| < 0.1$ GeV and 0.92 GeV$/c^2 < M_{K\pi}$), ΔE (in 5.273 GeV$/c^2 < M_{\rm bc} < 5.285$ GeV$/c^2$ and 0.92 GeV$/c^2 < M_{K\pi}$), and $M_{K\pi}$. Curves show the signal (dashed, red), continuum (dot-dot-dashed, blue), $B \to K^*\gamma$ (dotted, magenta), other backgrounds (dash-dotted, green), and the total fit result (solid).

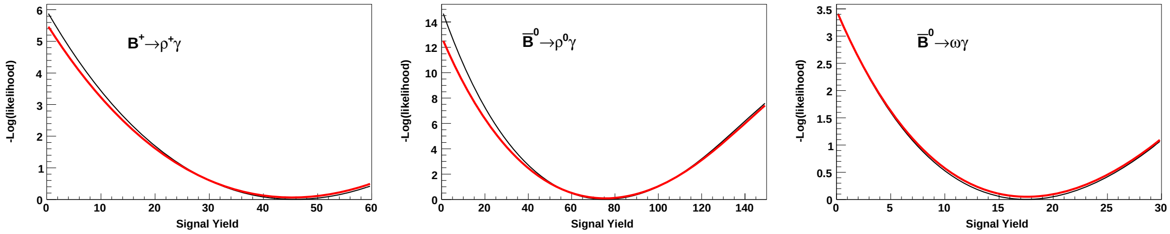

Figure 39: Negative log-likelihood as a function of signal yield before (black-thin) and after (red-thick) convolution of systematic errors.

Table 10: The number of B background components for each mode.

Mode	$\mathcal{B}$	Expected events		
	$(\times 10^{-6})$	$\rho^+\gamma$	$\rho^0\gamma$	$\omega\gamma$
$K^{*+}\gamma$	37.8 ± 0.8	56.4 ± 2.5	-	-
$K^{*0}\gamma$	38.4 ± 1.7	-	224.8 ± 17.5	-
$X_s\gamma$	355 ± 26	138.2 ± 20.7	259.6 ± 38.9	48.9 ± 7.3
$B^+ \to \rho^+\pi^0$	$10.8\,^{+1.4}_{-1.5}$	$31.9\,^{+4.0}_{-4.4}$	-	-
$B^+ \to \rho^+\eta$	$5.4\,^{+1.2}_{-1.1}$	22.3 ± 5.0	-	-
$B^0 \to \rho^0\pi^0$	$1.8\,^{+0.6}_{-0.5}$	-	$10.9\,^{+0.36}_{-0.30}$	-
$B^0 \to \rho^0\eta$	$< 1.5(0.75 \pm 0.75)$	-	$< 6.9(3.45 \pm 3.45)$	-
$B^0 \to \omega\pi^0$	$< 1.2(0.6 \pm 0.6)$	-	-	$< 3.9(1.95 \pm 1.95)$
$B^0 \to \omega\eta$	$< 1.9(0.95 \pm 0.95)$	-	-	$< 4.6(2.3 \pm 2.3)$
other rare B decays		59.7 ± 9.0	83.2 ± 12.5	31.4 ± 4.7
$b \to c$		111.6 ± 55.8	130.4 ± 65.2	20.3 ± 10.2

Table 11: Summary of the fitting systematic errors.

	$B^+ \to \rho^+\gamma$	$B^0 \to \rho^0\gamma$	$B^0 \to \omega\gamma$
ΔE $\mu - 1\sigma$	$+0.277$	$+0.480$	-0.418
ΔE $\mu + 1\sigma$	-0.444	-0.568	$+0.378$
ΔE $\sigma - 1\sigma$	-1.028	-1.331	-0.379
ΔE $\sigma + 1\sigma$	$+0.856$	$+1.196$	$+0.309$
ΔE alternative n, α, μ, σ (1)	-0.132	—	-0.004
ΔE alternative n, α, μ, σ (2)	-0.043	$+0.583$	-0.008
ΔE alternative n, α, μ, σ (3)	-0.243	-0.502	$+0.017$
energy-shift -1σ	$+0.497$	$+0.440$	$+0.113$
energy-shift $+1\sigma$	-0.406	-0.317	-0.076
$K^*\gamma$ PDF ΔE shift -1σ	$+0.335$	-1.286	—
$K^*\gamma$ PDF ΔE shift $+1\sigma$	-0.022	$+1.701$	—
$M_{\rm bc}$ $\mu - 1\sigma$	$+0.076$	$+0.127$	$+0.031$
$M_{\rm bc}$ $\mu + 1\sigma$	-0.134	-0.149	-0.048
$M_{\rm bc}$ $\sigma - 1\sigma$	-0.991	-0.357	-0.303
$M_{\rm bc}$ $\sigma + 1\sigma$	$+0.735$	$+0.335$	$+0.301$
$M_{\rm bc}$ alternative α, μ, σ (1)	-1.610	—	-0.308
$M_{\rm bc}$ alternative α, μ, σ (2)	-1.315	—	$+0.112$
$M_{\rm bc}$ alternative α, μ, σ (3)	-1.863	—	$+0.040$
$K^{*0}\gamma$ -1σ	—	$+1.163$	$+0.010$
$K^{*0}\gamma$ $+1\sigma$	—	-1.141	-0.004
$K^{*+}\gamma$ -1σ	$+0.612$	—	$+0.017$
$K^{*+}\gamma$ $+1\sigma$	-0.768	—	-0.026
K-id fake rate -1σ	$+1.017$	$+4.273$	—
K-id fake rate $+1\sigma$	-1.138	-4.033	—
$X_s\gamma$ -1σ	-0.067	-0.032	$+0.252$
$X_s\gamma$ $+1\sigma$	-0.164	$+0.027$	-0.248
$V\pi^0$ -1σ	$+1.501$	$+0.951$	$+0.805$
$V\pi^0$ $+1\sigma$	-1.491	-1.193	-0.447
$V\eta$ -1σ	$+0.709$	$+0.338$	$+0.235$
$V\eta$ $+1\sigma$	-0.817	-0.391	-0.419
rare -1σ	$+0.004$	$+0.120$	-0.016
rare $+1\sigma$	-0.353	-0.168	$+0.010$
$b \to c$ -1σ	$+0.004$	$+0.120$	-0.016
$b \to c$ $+1\sigma$	-0.353	-0.168	$+0.010$
$M_{K\pi}$		-3.58	
Total Syst. Error	$+2.62$	$+5.12$	$+1.06$
	-3.94	-6.05	-0.98
Signal yield	$45.8^{+15.2}_{-14.5}$	$75.7^{+16.8}_{-16.0}$	$17.5^{+8.2}_{-7.4}$

6.1.1 Combined Branching Fraction

We combine the $B^0 \to \rho^0\gamma$ and $B^+ \to \rho^+\gamma$ modes (referred to as $\rho\gamma$) and further combine the three $\rho\gamma$ and $\omega\gamma$ modes (referred to as $(\rho,\omega)\gamma$) assuming a single branching fraction $\mathcal{B}(B \to \rho\gamma) \equiv \mathcal{B}(B \to (\rho,\omega)\gamma) \equiv \mathcal{B}(B^+ \to \rho^+\gamma) = 2\times\frac{\tau_{B^+}}{\tau_{B^0}}\mathcal{B}(B^0 \to \rho^0\gamma) = 2\times\frac{\tau_{B^+}}{\tau_{B^0}}\mathcal{B}(B^0 \to \omega\gamma)$ where $\frac{\tau_{B^+}}{\tau_{B^0}} = 1.071\pm0.009$ [48] is the ratio of the lifetime of B^+ and B^0. They may be useful to reduce the statistical error for the $|V_{td}/V_{ts}|$ determination under an assumption that the error on the mode dependence (isospin violation) is smaller than the experimental error as estimated in theoretical calculations.

To calculate the combined branching fraction, we use the likelihood curves of the individual fit results for each mode. As a function of the branching fraction, we calculate a combined likelihood as the product of likelihood of the two (three) individual fits at the corresponding signal yields. The central value of the branching fraction is obtained from the maximum of the combined likelihood and its statistical error is obtained as the displacement where the logarithm of the likelihood is smaller by 0.5 than the maximum value. To estimate the systematic error, we prepare a modified likelihood curve for each case listed in Table 9 (efficiency) and Table 11 (fitting) and recalculate a new likelihood curve for the combined branching fraction whose maximum is shifted from the nominal case. For each systematic error item, we regard the deviation from the nominal value as its error and assign the quadratical sum of all positive (negative) deviations as the positive (negative) systematic error. The obtained combined branching fraction is listed in Table 12. The significance is calculated from the combined likelihood curve with convolution method described in the previous section.

Table 12: Summary of branching fractions. Significances with systematic error are also listed.

Mode	Yield	Efficiency (%)	B.F. ($\times10^{-6}$)	Significance
$B^+ \to \rho^+\gamma$	$45.8\,^{+15.2}_{-14.5}\,^{+2.62}_{-3.94}$	8.03 ± 0.59	$0.87\,^{+0.29}_{-0.27}\,^{+0.09}_{-0.11}$	3.3
$B^0 \to \rho^0\gamma$	$75.7\,^{+16.8}_{-16.0}\,^{+5.12}_{-6.05}$	14.81 ± 0.95	$0.78\,^{+0.17}_{-0.16}\,^{+0.09}_{-0.10}$	5.0
$B^0 \to \omega\gamma$	$17.5\,^{+8.2}_{-7.4}\,^{+1.06}_{-0.98}$	6.58 ± 0.76	$0.40\,^{+0.19}_{-0.17} \pm 0.13$	2.6
$B \to \rho\gamma$	—	—	$1.21\,^{+0.24}_{-0.22} \pm 0.12$	5.8
$B \to (\rho,\omega)\gamma$	—	—	$1.14 \pm 0.20\,^{+0.10}_{-0.12}$	6.2

6.1.2 Ratios of branching fractions to $B \to K^*\gamma$

A constraint on $|V_{td}/V_{ts}|$ can be derived from the ratio of branching fractions for $B \to \rho\gamma$ to $B \to K^*\gamma$. It is usually considered that the ratio is more immune than the branching fraction itself to uncertainties in theoretical calculations although the calculation of $|V_{td}/V_{ts}|$ need various perturbative and non-perturbative corrections. We provide three ratios: $\mathcal{B}(B^0 \to \rho^0\gamma)/\mathcal{B}(B^0 \to K^{*0}\gamma)$, $\mathcal{B}(B \to \rho\gamma)/\mathcal{B}(B \to K^*\gamma)$ and $\mathcal{B}(B \to (\rho.\omega)\gamma)/\mathcal{B}(B \to K^*\gamma)$.

Figures 40 and 41 show the 2D fit results for $B^0 \to K^{*0}\gamma$ and $B^+ \to K^{*+}\gamma$, respectively. PDFs for $K^*\gamma$ modes are same as that of $\rho\gamma$ modes. In the fit, shape parameters

(n, α) and normalization of B background are fixed. The parameter sets (n, α) for $K^{*+}\gamma$ are same as $\rho^+\gamma$. For $K^{*0}\gamma$, it is determined from fitting to $K^{*0}\gamma$ MC sample. We consider continuum, $B \to X_s\gamma$ and rare B backgrounds. The signal yields are calculated to be $2633.0\,^{+56.2}_{-54.7}$ and $692.9\,^{+31.2}_{-30.1}$. We obtain $\mathcal{B}(B^0 \to K^{*0}\gamma) = (37.8 \pm 0.8) \times 10^{-6}$ and $\mathcal{B}(B^+ \to K^{*+}\gamma) = (38.4 \pm 1.7) \times 10^{-6}$ (statistical error only), which are consistent with the world averages [48]. We calculate the combined branching fraction for $B \to K^*\gamma$ under the assumption

$$\mathcal{B}(B \to K^*\gamma) = \mathcal{B}(B^+ \to K^{*+}\gamma) = \frac{\tau_{B^+}}{\tau_{B^0}}\mathcal{B}(B^0 \to K^{*0}\gamma). \tag{43}$$

Using the likelihood curves of the fit results in similar way as $B \to \rho\gamma$, we obtain $\mathcal{B}(B \to K^*\gamma) = (40.1\,^{+0.71}_{-0.86}) \times 10^{-6}$ (statistical error only). The systematic errors for $B \to K^*\gamma$ can be estimated in the same way as $B \to \rho\gamma$. In the calculation of the systematic error of the ratio, systematic errors due to the efficiency for photon detection, tracking, π^0 reconstruction, π^0/η veto and $\mathcal{R}$ requirements and fit bias in Table 9, are considered to be common and to cancel. The particle identification systematic errors are listed in Table 23. Uncertainty due to the MC statistics is 0.40% (0.50%) for $B^0 \to K^{*0}\gamma$ ($B^+ \to K^{*+}\gamma$). The fitting systematic error for $B \to K^*\gamma$ is calculated using the same method as $B \to \rho\gamma$; Table 13 lists the individual and total fitting systematic error as the deviation from the nominal branching fraction. The ratio of branching fraction $\mathcal{B}(B^0 \to \rho^0\gamma)/\mathcal{B}(B^0 \to K^{*0}\gamma)$ is calculated as a simple ratio where both the statistical and systematic errors are calculated using error propagation. The relevant systematic errors on particle identification, MC statistics and fitting except energy-shift are treated to be independent in the error propagation. The ratio is calculated to be

$$\frac{1}{2}R^{\rho^0\gamma} = \frac{\mathcal{B}(B^0 \to \rho^0\gamma)}{\mathcal{B}(B^0 \to K^{*0}\gamma)} = 0.0206\,^{+0.0045}_{-0.0043}\,^{+0.0014}_{-0.0016}, \tag{44}$$

where the first and second errors are statistical and systematic, respectively. Note that an additional isospin factor 2 has to be multiplied to Eq. 44 to compare with the ratio from the charged mode or combined results.

Derivation of errors for the ratio of combined branching fractions is more complicated. The statistical error is calculated from those of the combined results, $\mathcal{B}(B \to \rho\gamma)$, $\mathcal{B}(B \to (\rho, \omega)\gamma)$ and $\mathcal{B}(B \to K^*\gamma)$. The systematic error is calculated using similar technique that is used to calculate the systematic error for the combined results. For each of the systematic error items in Table 14, the relevant branching fraction are simultaneously varied by $\pm 1\sigma$ and the individual and combined likelihood curves are recalculated for each variation of $\pm 1\sigma$. For example, the π^0 detection efficiency is only relevant for the $\rho^+\gamma$, $\omega\gamma$ and $K^{*+}\gamma$ modes. Therefore, their branching fractions are simultaneously varied by 4.6% (fractional error of π^0 detection efficiency) while those for $\rho^0\gamma$ and $K^{*0}\gamma$ are unchanged. The likelihood ratio, π^0/η veto and fit bias systematic error are considered to be common between $B^0 \to \rho^0\gamma$ and $B^0 \to K^{*0}\gamma$ and varied simultaneously for these two modes; those between $B^+ \to \rho^+\gamma$ and $B^+ \to K^{*+}\gamma$ are also simultaneously varied with a common amount, but independently from those for $B^0 \to \rho^0\gamma$ and $B^0 \to K^{*0}\gamma$. The fitting systematic errors are considered to be independent each other. Thus obtained results on the ratios are,

$$R^{\rho\gamma} = \frac{\mathcal{B}(B \to \rho\gamma)}{\mathcal{B}(B \to K^*\gamma)} = 0.0302\,^{+0.0060}_{-0.0055}\,^{+0.0026}_{-0.0028},, \tag{45}$$

$$R^{(\rho,\omega)\gamma} = \frac{\mathcal{B}(B \to (\rho,\omega)\gamma)}{\mathcal{B}(B \to K^{*}\gamma)} = 0.0284 \pm 0.0050\,^{+0.0027}_{-0.0029}, \tag{46}$$

where the first and second errors are statistical and systematic, respectively.

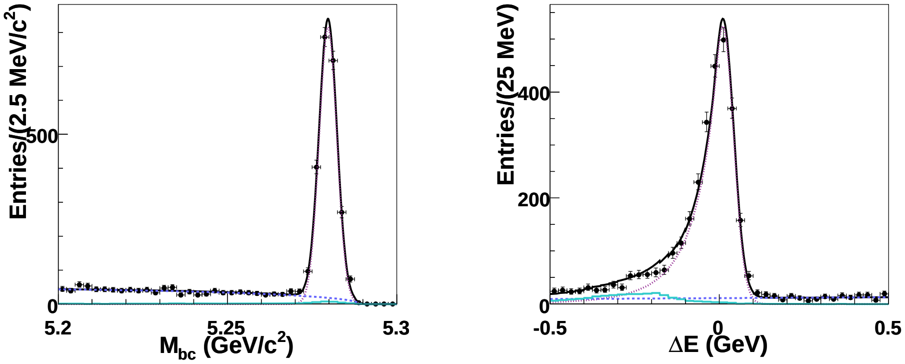

Figure 40: 2D fit results for $B^0 \to K^{*0}\gamma$. $M_{\rm bc}$ (left), ΔE (right) distributions for $B^0 \to K^{*0}\gamma$. These plots are after applying the selection of the signal region except for the displaying variable. Curves show the signal (dotted, magenta), continuum (dashed, blue), other backgrounds (histogram, cyan) and the total fit result (solid).

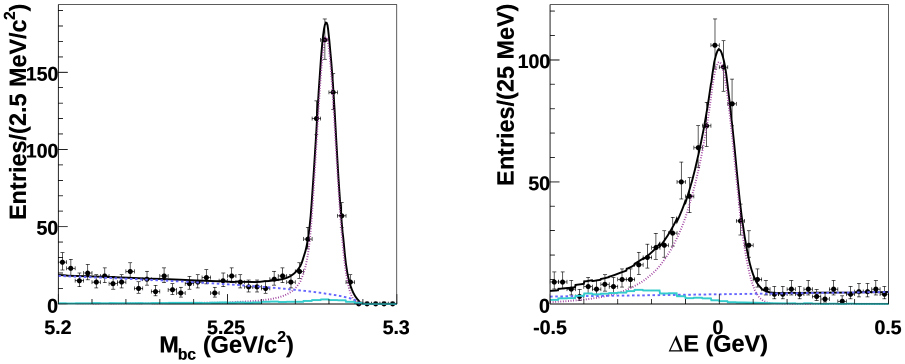

Figure 41: 2D fit results for $B^+ \to K^{*+}\gamma$. $M_{\rm bc}$ (left), ΔE (right) distributions for $B^+ \to K^{*+}\gamma$. These plots are after applying the selection of the signal region except for the displaying variable. Curves show the signal (dotted, magenta), continuum (dashed, blue), other backgrounds (histogram, cyan) and the total fit result (solid).

Table 13: Summary of the fitting systematic errors for $B \to K^{*}\gamma$.

	$\mathcal{B}(B^0 \to K^{*0}\gamma)$	$\mathcal{B}(B^+ \to K^{*+}\gamma)$
	$\delta\mathcal{B}$	$\delta\mathcal{B}$
$\Delta E n - 1\sigma$	+0.029	+0.044
$\Delta E n + 1\sigma$	−0.014	−0.048
$\Delta E \alpha - 1\sigma$	+0.020	+0.075
$\Delta E \alpha + 1\sigma$	−0.013	−0.11
energy-shift -1σ	+0.071	+0.070
energy-shift $+1\sigma$	−0.005	−0.008
$M_{\mathrm{bc}} n - 1\sigma$	−	+0.20
$M_{\mathrm{bc}} n + 1\sigma$	−	−0.12
$M_{\mathrm{bc}} \alpha - 1\sigma$	−	+0.13
$M_{\mathrm{bc}} \alpha + 1\sigma$	−	−0.15
$X_s\gamma$ -1σ	+0.128	+0.19
$X_s\gamma$ $+1\sigma$	−0.11	−0.19
rare -1σ	+0.09	+0.16
rare $+1\sigma$	−0.07	−0.14
Total Syst. Error	+0.18 −0.13	+0.36 −0.32

Table 14: The list of the systematic error for the ratio.

Source	Fractional error(%)	the deviation from the nominal value	
		$\delta\frac{\mathcal{B}(B\to\rho\gamma)}{\mathcal{B}(B\to K^{*}\gamma)}$	$\delta\frac{\mathcal{B}(B\to(\rho,\omega)\gamma)}{\mathcal{B}(B\to K^{*}\gamma)}$
1(2)-Track	1.0(2.0)	-0.00020 $+0.00039$	-0.00027 $+0.00019$
PID	1.1($\rho^0\gamma, \omega\gamma$) 0.5($\rho^+\gamma$) 1.3($K^{*0}\gamma$) 0.7($K^{*+}\gamma$)	-0.00007 $+0.00024$	-0.00013 $+0.00016$
LR and π^0/ηveto	2.3($\rho^0\gamma$)	$+0.00029$ -0.00024	$+0.00058$ -0.00062
	3.1($\rho^+\gamma$)	-0.00038 $+0.00034$	-0.00052 -0.00003
	8.4($\omega\gamma$)	-	-0.00092 $+0.00017$
π^0	4.6	$+0.00029$ -0.0010	$+0.00004$ -0.00067
Fit bias	5.1($\rho^0\gamma$)	-0.00110 $+0.00043$	-0.00066 $+0.00025$
	4.5($\rho^+\gamma$)	$+0.00029$ -0.00098	$+0.00100$ -0.00097
	5.4($\omega\gamma$)	-	-0.00089 $+0.00017$
MC stat	0.42($\rho^0\gamma$)	-0.00005 $+0.00022$	-0.00012 $+0.00010$
	0.56($\rho^+\gamma$)	$+0.00027$ -0.00010	$+0.00016$ -0.00016
	0.48($\omega\gamma$)	-	-0.000025 0.00000
$\mathcal{B}(\omega\to\pi^+\pi^-\pi^0)$	0.79	-	-0.00002 0.00000
fitting syst.		+0.002258 - 0.001965	+0.00216 - 0.00183
total		$+0.0026$ -0.0028	$+0.0027$ -0.0029

6.2 Isospin asymmetry

We calculate the isospin asymmetry,

$$\Delta(\rho\gamma) = \frac{\tau_{B^0}}{2\tau_{B^+}} \frac{\mathcal{B}(B^+ \to \rho^+\gamma)}{\mathcal{B}(B^0 \to \rho^0\gamma)} - 1. \tag{47}$$

The result is,

$$\Delta(\rho\gamma) \quad = \quad -0.48\,^{+0.21}_{-0.19}\,^{+0.08}_{-0.09}. \tag{48}$$

Isospin asymmetry is calculated as a simple ratio where both the statistical and systematic errors are calculated using error propagation. In the calculation of the systematic error, systematic error due to the efficiency for photon detection is considered to cancel. Since the error is still very large, the result is in agreement with SM expectations. We do not include an uncertainty of the assumption of the equal number of neutral and charged B pairs.

6.3 Charge Asymmetry of $B^+ \to \rho^+\gamma$

We calculate direct CP asymmetry,

$$A_{CP}(B^+ \to \rho^+\gamma) = \frac{N(\rho^-\gamma) - N(\rho^+\gamma)}{N(\rho^-\gamma) + N(\rho^+\gamma)}, \tag{49}$$

where $N(\rho^-\gamma)$ and $N(\rho^+\gamma)$ are the signal yields for the $B^+ \to \rho^+\gamma$ and $B^- \to \rho^-\gamma$ modes, respectively. The direct CP asymmetry is obtained by the simultaneous 2D-fit to $M_{\rm bc}$-ΔE distribution of B^+ and B^- sample. The $A_{CP}(B^+ \to \rho^+\gamma)$, A_{CP} of the continuum background ($A_{CP}^{q\bar{q}}$), $N_{\rho^+\gamma}$, N_{qq} and the continuum shape parameter ($M_{\rm bc}$ ARGUS shape and ΔE slope) are floated in the fit. The A_{CP} for the other background is fixed to zero in the nominal fit and included in the systematic error. The A_{CP} values are varied according to Table15. Since all measured A_{CP} values are consistent with zero, we take a quadratic sum of the central value and error as 1σ. For other rare B decays, we conservatively vary by ±100% asymmetry. Most of the systematic errors in efficiency are same for B^+ and B^- and cancel in A_{CP}. Asymmetry of charged pion identification is less than 0.1% and thus negligible. We estimate the systematic errors due to the fitting in the same procedure as previously described.

Table 16 lists the deviation of the charge asymmetry from the nominal value in each variation. The total systematic error includes the $A_{CP}(B \to D\pi) = -0.018 \pm 0.011$ as possible detector bias (See Appendix H for detail). (We take the quadratic sum of the deviation and statistical error, $\sqrt{(0.018^2) + (0.011)^2}$.) The result of $A_{CP}^{q\bar{q}}$ is 0.003 ± 0.010, which is consistent with zero. We obtain the result of the direct CP asymmetry

$$A_{CP}(B^+ \to \rho^+\gamma) = -0.11 \pm 0.32 \pm 0.09 \tag{50}$$

Table 15: The list of A_{CP} values used for the systematic study.

mode	A_{CP}	
$B^+ \to K^{*+}\gamma$	-0.010 ± 0.028	HFAG LP07
kid-fake rate	0.0065 ± 0.034	–
$B \to X_s\gamma$	0.004 ± 0.037	HFAG LP07
$B^+ \to \rho^+\pi^0$	0.02 ± 0.11	HFAG LP07
$B^+ \to \rho^+\eta$	0.01 ± 0.16	HFAG LP07
Other rare B decays	± 1.0	

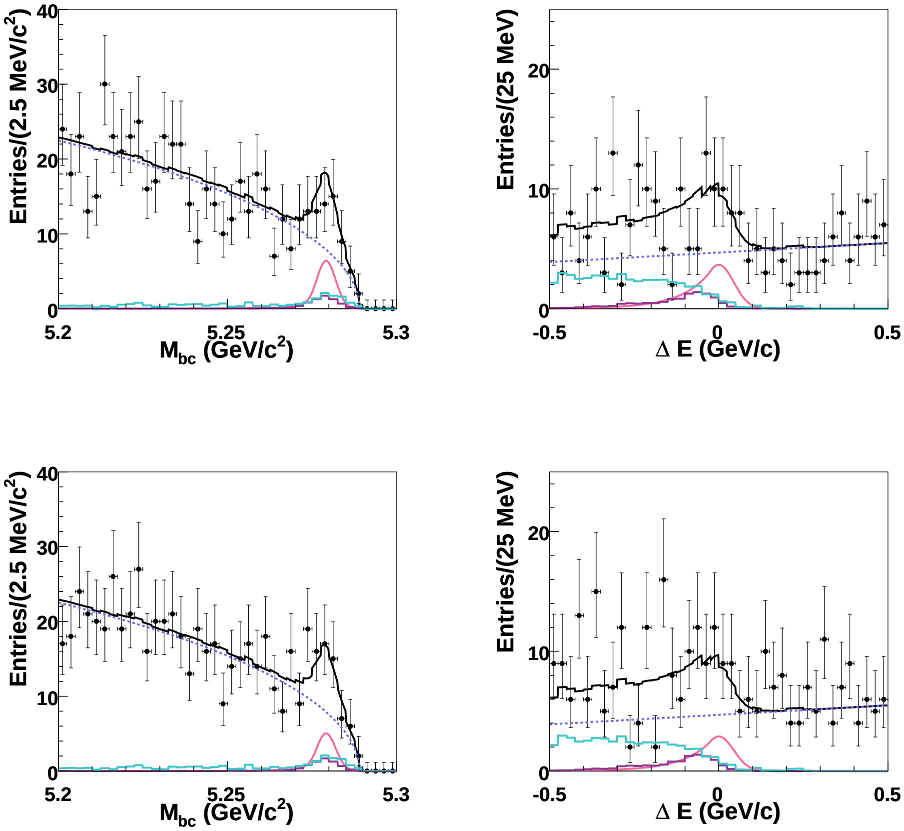

Figure 42: 2D simultaneous fit result for $B^+ \to \rho^+\gamma$. M_{bc}(left),ΔE(right) distributions for $B^+ \to \rho^+\gamma$ with 605 fb^{-1}. Plots are for $B^+ \to \rho^+\gamma$(top) and $B^- \to \rho^-\gamma$(bottom).

Table 16: Summary of the systematic errors for $A_{CP}(B^+ \to \rho^+\gamma)$.

ΔE $\mu - 1\sigma$	-0.00973		
ΔE $\mu + 1\sigma$	$+0.00978$		
ΔE $\sigma - 1\sigma$	$+0.0041$		
ΔE $\sigma + 1\sigma$	-0.0052		
ΔE alternative n, α, μ, σ (1)	-0.00218		
ΔE alternative n, α, μ, σ (2)	-0.00239		
ΔE alternative n, α, μ, σ (3)	-0.00250		
energy-shift -1σ	$+0.01823$		
energy-shift $+1\sigma$	-0.00545		
$K^*\gamma$ PDF ΔE shift -1σ	$+0.00294$		
$K^*\gamma$ PDF ΔE shift $+1\sigma$	-0.00024		
$M_{\rm bc}$ $\mu - 1\sigma$	-0.0129		
$M_{\rm bc}$ $\mu + 1\sigma$	$+0.0126$		
$M_{\rm bc}$ $\sigma - 1\sigma$	$+0.00854$		
$M_{\rm bc}$ $\sigma + 1\sigma$	-0.00839		
$M_{\rm bc}$ alternative α, μ, σ (1)	-0.00118		
$M_{\rm bc}$ alternative α, μ, σ (2)	-0.00231		
$M_{\rm bc}$ alternative α, μ, σ (3)	$+0.00447$		
$K^{*+}\gamma$ -1σ	-0.00006	$A_{CP}(B \to K^{*+}\gamma) - 1\sigma$	$+0.00929$
$K^{*+}\gamma$ $+1\sigma$	-0.00102	$A_{CP}(B \to K^{*+}\gamma) + 1\sigma$	-0.00965
K-id fake rate -1σ	-0.00051	$A_{CP}(K\text{-id}) - 1\sigma$	$+0.0110$
K-id fake rate $+1\sigma$	-0.00004	$A_{CP}(K\text{-id}) + 1\sigma$	-0.0108
$X_s\gamma$ -1σ	-0.00052	$A_{CP}(B \to X_s\gamma) - 1\sigma$	-0.00006
$X_s\gamma$ $+1\sigma$	$+0.00193$	$A_{CP}(B \to X_s\gamma) + 1\sigma$	-0.00299
$V\pi^0$ -1σ	$+0.00115$	$A_{CP}(B \to \rho^+\pi^0) - 1\sigma$	$+0.0327$
$V\pi^0$ $+1\sigma$	$+0.00103$	$A_{CP}(B \to \rho^+\pi^0) + 1\sigma$	-0.0273
$V\eta$ -1σ	-0.00066	$A_{CP}(B \to \rho^+\eta) - 1\sigma$	$+0.0073$
$V\eta$ $+1\sigma$	$+0.00353$	$A_{CP}(B \to \rho^+\eta) + 1\sigma$	-0.0267
rare -1σ	$+0.00042$	$A_{CP}(\text{rare}) - 1\sigma$	-0.0774
rare $+1\sigma$	-0.00056	$A_{CP}(\text{rare}) + 1\sigma$	-0.0741
$b \to c$ -1σ	-0.00056		
$b \to c$ $+1\sigma$	-0.00027		
Total Syst. Error			$+0.089$
			-0.092

7 Discussion and Conclusions

The ratio of branching fractions of $B \to \rho\gamma$ and $B \to K^*\gamma$ (R) is often parametrized as

$$R = \left|\frac{V_{td}}{V_{ts}}\right|^2 \left(\frac{1 - m_\rho^2/m_B^2}{1 - m_{K^*}^2/m_B^2}\right)^3 \frac{1}{\xi^2}[1 + \Delta R], \tag{51}$$

where ξ is due to the form factor ratio and ΔR is relevant to the isospin violation. The detail is described in Appendix I. We extract $|V_{td}/V_{ts}|$ from the ratio of the branching fractions taken from Eq. (46). The statistical error and systematic errors are added in quadrature (denoted as the experimental error) and assumed to follow a Gaussian distribution. For the theory parameters, they are assumed to follow a flat distribution. The result is

$$|V_{td}/V_{ts}| = 0.195\,^{+0.020}_{-0.019} \pm 0.015, \tag{52}$$

where the first and second errors are experimental and theoretical, respectively. The ratios from Eqs. (44) and (45) give following values,

$$|V_{td}/V_{ts}|_{(B^0\to\rho^0\gamma/B^0\to K^{*0}\gamma)} = 0.243\,^{+0.028}_{-0.027} \pm 0.018, \tag{53}$$

$$|V_{td}/V_{ts}|_{(B\to\rho\gamma/B\to K^*\gamma)} = 0.201 \pm 0.021 \pm 0.015, \tag{54}$$

where the first and second errors are experimental and theoretical, respectively. Combining Eq. (46) with Babar results $R^{(\rho/\omega)\gamma} = 0.030 \pm 0.006$ [10], world average is

$$|V_{td}/V_{ts}|_{WA} = 0.197 \pm 0.015 \pm 0.015, \tag{55}$$

These results are agreement with the result extracted from B_d^0/B_s^0 mixing reported by CDF collaboration [59].

$$|V_{td}/V_{ts}|_{\Delta m_d/\Delta m_s} = 0.208\,^{+0.001}_{-0.002}\,^{+0.008}_{-0.006}, \tag{56}$$

where the first and second errors are experimental and theoretical, respectively. We find good agreement between these different physics processes.

The experimental error of Eq. (55) is 7.8% already comparable to the theoretical error 7.6%. In the near future, the experimental uncertainty will be reduced to a level of $\sim 5\%$ by Super B factory. The theoretical uncertainty will likely not be reduced at the same pace because of already very extensive calculations. However, future lattice QCD have possibility of reducing the theoretical errors. Since exclusive measurement is limited by uncertainty of hadronization, inclusive measurement is expected with more data and improvement for particle identification . It is a promising method for a improved $|V_{td}/V_{ts}|$ determination.

Table 17 shows the comparison with previous results [9] and Babar results [10], and Figure 43 shows a comparison of the experimental results and theoretical predictions.

Table 17: Comparison with experimental results of Babar and Belle.

Experiment	Belle [9]	Babar [10]	Belle
$\mathcal{B}(B^+ \to \rho^+\gamma)$	$0.55\,^{+0.42}_{-0.36}\,^{+0.09}_{-0.08}$	$1.10\,^{+0.37}_{-0.33} \pm 0.09$	$0.87\,^{+0.29}_{-0.27}\,^{+0.09}_{-0.11}$
$\mathcal{B}(B^0 \to \rho^0\gamma)$	$1.25\,^{+0.37}_{-0.33}\,^{+0.07}_{-0.06}$	$0.79\,^{+0.22}_{-0.20} \pm 0.06$	$0.78\,^{+0.17}_{-0.16}\,^{+0.09}_{-0.10}$
$\mathcal{B}(B^0 \to \omega\gamma)$	$0.56\,^{+0.34}_{-0.27}\,^{+0.05}_{-0.10}$	$0.40\,^{+0.24}_{-0.20} \pm 0.05$	$0.40\,^{+0.19}_{-0.17} \pm 0.13$
$\mathcal{B}(B \to \rho\gamma)$	–	$1.36\,^{+0.29}_{-0.27} \pm 0.10$	$1.21\,^{+0.24}_{-0.22} \pm 0.12$
$\mathcal{B}(B \to (\rho,\omega)\gamma)$	$1.32\,^{+0.34}_{-0.31}\,^{+0.10}_{-0.09}$	$1.25\,^{+0.25}_{-0.24} \pm 0.09$	$1.14 \pm 0.20\,^{+0.10}_{-0.12}$

We compare the results of this analysis with those of Babar [10]. The theoretical predictions are derived in Refs. [6, 19, 20]. Although the center value of isospin asymmetry $\Delta(\rho\gamma) = -0.48\,^{+0.21}_{-0.19}\,^{+0.08}_{-0.09}$. is large, the deviation from zero is less than 2σ. In the Standard Model, $\Delta(\rho\gamma)$ is in the range from -10% to 20% depending on ϕ_2 value. [6]. The results of branching fraction are good agreement with Babar results. The *CP*-violating asymmetry for $B^+ \to \rho^+\gamma$ is first measured in this analysis. The $A_{CP}(\rho^0\gamma) = -0.44 \pm 0.49 \pm 0.14$ has been measured with time-dependent *CP* violation analysis [60]. Both results are consistent with the Standard Model predictions [Eqs. (10)(11)], but also consistent with no-*CP* asymmetry due to large errors. To confirm the direct *CP* violation at $b \to d\gamma$ process, more data and analysis improvement to obtain higher efficiency are necessary.

As described in Sec. 2.4.2, $\Delta(\rho\gamma)$ and A_{CP} is a probe for new physics. The results of this analysis are compared with the theoretical predictions in Figure 44. We do not find a signature of physics beyond the Standard Model due to low statistic. However, future measurements, super-*B* factory, are expected to reduce statistical uncertainty with ~ 10 times or more larger data samples.

For $\rho\gamma$ modes, systematic error due to $K^*\gamma$ modes are main component as was expected. To reduce the systematic error, improvement for particle identification is necessary. $K^*\gamma$ mode is significant background source because of misidentification of charged kaon as charged pion. Belle ACC will be upgraded to be a ring image Cherenkov counter which has better particle identification and is not much affected by knock-on electron.

In conclusion, we present a new measurement of branching fractions for $B \to \rho\gamma$ and $B \to \omega\gamma$ and the first measurement of the direct *CP*-violating asymmetry for $B^+ \to \rho^+\gamma$ with a 1.7 times larger data sample and an improved analysis procedures compared to out previous analysis. For all signal modes, we obtain 10% higher efficiency using end-cap photons. For $\rho^0\gamma$ mode, 20% higher efficiency and 12% higher significance are obtained by performing 3D fit to $M_{\rm bc}$-ΔE-$M_{K\pi}$. In addition, we include additional variables ($M_{\pi^+\pi^-\pi^0}$, Dalitz probability density) in the likelihood ratio for $B^0 \to \omega\gamma$ analysis, which results in the better significance.

The results are consistent with SM predictions. We improve the experimental precision on $|V_{td}/V_{ts}|$ determined from penguin loops, finding good agreement with the value determined from box diagrams [55, 59].

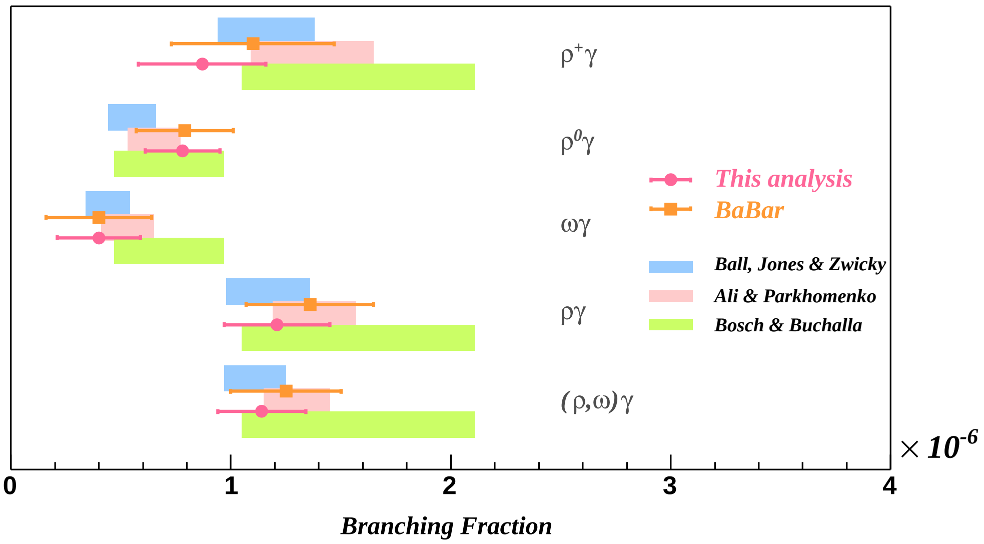

Figure 43: Comparison of experimental results and theoretical predictions. The relation in Eq. (43) is used for $\rho^0\gamma$, $\omega\gamma$, $\rho\gamma$ and $(\rho,\omega)\gamma$ of Bosch & Buchalla.

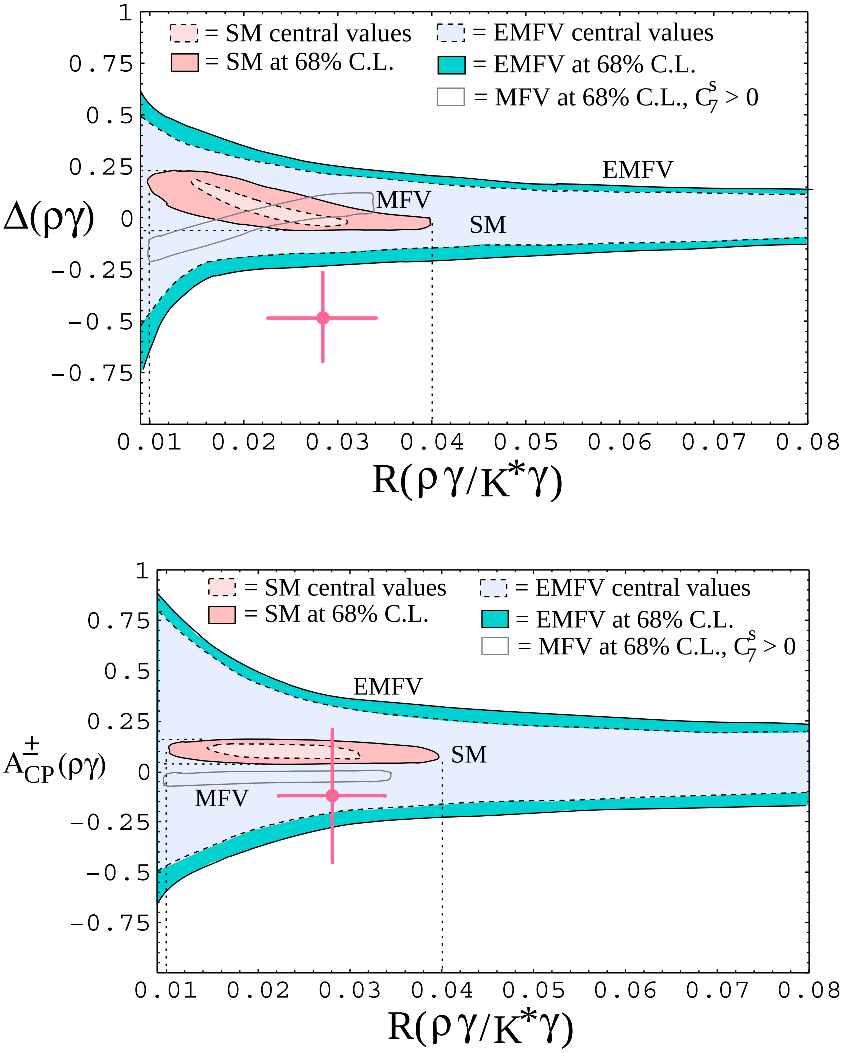

Figure 44: Correlation between $R(\rho\gamma/K^*\gamma)$ and $\Delta(\rho\gamma)$ (isospin asymmetry) (left) or A_{CP} (direct *CP* asymmetry) (right) in the Standard Model and the MFV and EMFV models [30]. Dots are from the results of this analysis.

A KSFW

The KSFW is a Fisher discriminant extended from the Super Fox-Wolfram (SFW) variable using information such as missing mass calculated from the daughter particles of the signal candidates and all the other particles in the event.

A.1 SFW

SFW is devised by modifying the Fox-Wolfram moment [51].The n-th Fox-Wolfram moment is defined in the c.m frame by

$$H_n \equiv \sum_{ij} |p_i||p_j| P_n(\cos\theta_{ij})$$

where P_n is the n-th *Legendre polynomial*, $|p_i|$ and $|p_j|$ are the momenta of the i-th and j-th particles, respectively, and θ_{ij} represents the opening angle between the two momentum vectors. The sum is over all particles in the final state. We divide H_n into three components and categorize the particles to the two type; B signal candidate particles and the remaining particles.

$$\begin{aligned} H_n &= H_n^{ss} + H_n^{so} + H_n^{oo} \\ H_n^{ss} &\equiv \sum_{ij} |p_i||p_j| P_n(\cos\theta_{ij}) \\ H_n^{so} &\equiv \sum_{jk} |p_j||p_k| P_n(\cos\theta_{jk}) \\ H_n^{oo} &\equiv \sum_{kl} |p_k||p_l| P_n(\cos\theta_{kl}) \end{aligned}$$

where i and j iterate over B signal candidates particles (denoted by s for the signal) and the indices k and l iterate over the remaining particles (denoted by o for other) in the event. A Fisher Discriminant[53] can be constructed as

$$SFW \equiv \sum_n \alpha_n \left(\frac{H_n^{so}}{H_0^{so}} \right) + \sum_n \beta_n \left(\frac{H_n^{oo}}{H_0^{oo}} \right)$$

where α_n and β_n are Fisher coefficients. We do not use H_n^{ss} since it is known to have a strong correlation with $M_{\rm bc}$ and ΔE and the separation of the distribution between signal and background is not good because the signal, $\rho\gamma$ and $\omega\gamma$, is two body decay which is jet-like similar to continuum background.

A.2 modified SFW (KSFW)

The modified SFW is so-called KSFW defined as

$$KSFW = \sum_{l=0}^{4} R_l^{so} + \sum_{l=0}^{4} R_l^{oo} + \gamma \sum_{n=1}^{N_t} |(p_t)_n| \tag{57}$$

where N_t is the number of the particles and γ is a Fisher coefficient to be optimized.

We define these terms in the Eq.(57) in tern.

◆ R_l^{so}

We add the missing pseudo-particle as one particle that has the event's missing energy, momentum (p_{miss}) and squared mass (M_{miss}^2) and furthermore divide the remaining particles in the event to three categories; "charged" , "neutral" and "missing".

$$R_l^{so} = \frac{(\alpha_c \cdot H_{charged}^{so})_l + (\alpha_n \cdot H_{neutral}^{so})_l + (\alpha_m \cdot H_{missing}^{so})_l}{E_{beam} - \Delta E}$$

where (α_C) $(C = c, n, m)$ are Fisher coefficients. Here $E_{\text{beam}} - \Delta E = H_0^{so}$. The definition of M_{miss}^2 is

$$M_{miss}^2 = (E_{\Upsilon(4S)} - \sum_{n=1}^{N_t} E_n)^2 - \sum_{n=1}^{N_t} |p_n|^2$$

For signal and other remaining charged particles,

$$(H_{charged}^{so})_l = \begin{cases} \sum_i \sum_j |p_j| P_l(\cos\theta_{ij}) & \text{if } l \text{ is even} \\ \sum_i \sum_j |p_j| Q_i Q_j P_l(\cos\theta_{ij}) & \text{if } l \text{ is odd} \end{cases}$$

where the index i iterates over the particles in the B signal candidates and the index j iterates over all other remaining charged particles. The $Q_{i,j}$ are the charge of the particle i and j.

For signal and other remaining neutral particles,

$$(H_{neutral}^{so})_l = \begin{cases} \sum_i \sum_j |p_j| P_l(\cos\theta_{ij}) & \text{if } l \text{ is even} \\ 0 & \text{if } l \text{ is odd} \end{cases}$$

where the index i iterates over the particles in the B signal candidates and the index j iterates over all other remaining neutral particles.

For signal and missing particles,

$$(H_{missing}^{so})_l = \begin{cases} \sum_i |p_i| P_l(\cos\theta_{iM}) & \text{if } l \text{ is even} \\ 0 & \text{if } l \text{ is odd} \end{cases}$$

where the index i iterates over the particles in the B signal candidates and the θ_{iM} is the opening angle between p_i and p_{miss}.

♦ R^{oo}_l

$$R^{oo}_l = \frac{(\beta \cdot H^{oo})_l}{(E_{\mathrm{beam}} - \Delta E)^2}$$

$$(H^{oo})_l = \begin{cases} \sum_j \sum_k |p_j||p_k|P_l(\cos\theta_{jk}) & \text{if } l \text{ is even} \\ \sum_j \sum_k |p_j||p_k|Q_jQ_kP_l(\cos\theta_{jk}) & \text{if } l \text{ is odd} \end{cases}$$

where the indices j and $k$iterates over all other remaining particles.

♦ $\sum_{n=1}^{N_t} |(p_t)_n|$

$\sum_{n=1}^{N_t} |(p_t)_n|$ is the scaler sum of the transverse momenta (p_t) of all the particles in the signal candidates and all the other remaining particles.

In total, there are 17 parameters in KSFW. Since the separation between signal and continuum background depends on M^2_{miss} value, we divide M^2_{miss} into 7 regions; (-∞, -0.5), (-0.5, 0.3), (0.3, 1.0), (1.0, 2.0), (2.0, 3.5), (3.5, 6.0) and (6.0, +∞) [in unit of (GeV/c^2)^2]. The parameters on KSFW are chosen to provide the optimum separation between $B\overline{B}$ events and continuum background events within the selected M^2_{miss} range. Figure 45 shows the distributions of the discriminant.

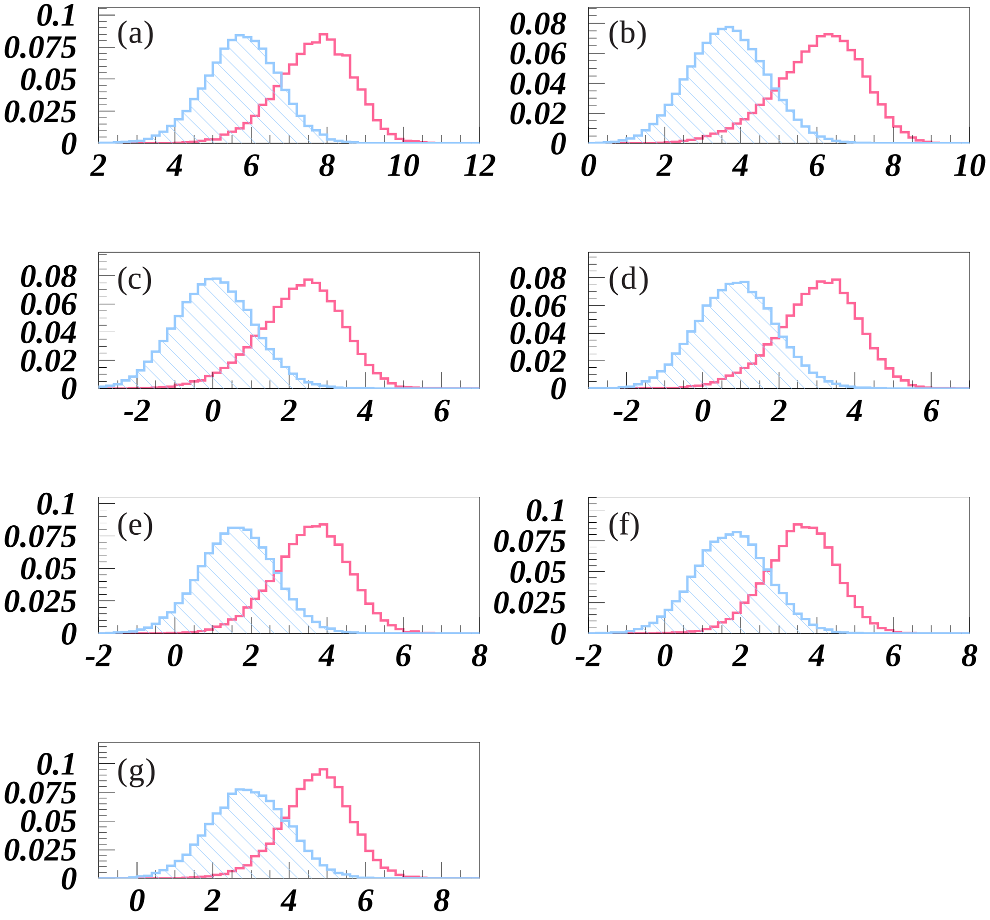

Figure 45: The distributions of the Fisher discriminant obtained from the KSFW for signal and continuum background (hatched) corresponding to the different missing mass regions. (a)$(-\infty, -0.5)$, (b)$(-0.5, 0.3)$, (c)$(0.3, 1.0)$, (d)$(1.0, 2.0)$, (e)$(2.0, 3.5)$, (f)$(3.5, 6.0)$ and (g)$(6.0, +\infty)$ [in unit of $(\mathrm{GeV}/c^2)^2$].

B Omega variables

In the $B^0 \to \omega\gamma$ analysis, we use two additional likelihoods to suppress continuum background. One is constructed from the $\pi^+\pi^-\pi^0$ invariant mass ($M_{\pi^+\pi^-\pi^0}$), and the other is the probability density on the $\pi^+\pi^-\pi^0$ Dalitz plot.

B.1 Invariant mass of ω

The $\pi^+\pi^-\pi^0$ invariant mass distribution of the $B^0 \to \omega\gamma$ signal follows a Breit-Wigner shape with $\Gamma \sim 8.5$ MeV smeared by a detector resolution. On the other hand, the distribution for combinatorial background is a sum of the Breit-Wigner component and a large non-ω component. We form a likelihood $\mathcal{L}_{S(B)}(M_{\pi^+\pi^-\pi^0})$ for signal (background) from the histogram of the invariant mass distribution for the signal (continuum) MC sample. Figure 46 shows the distributions.

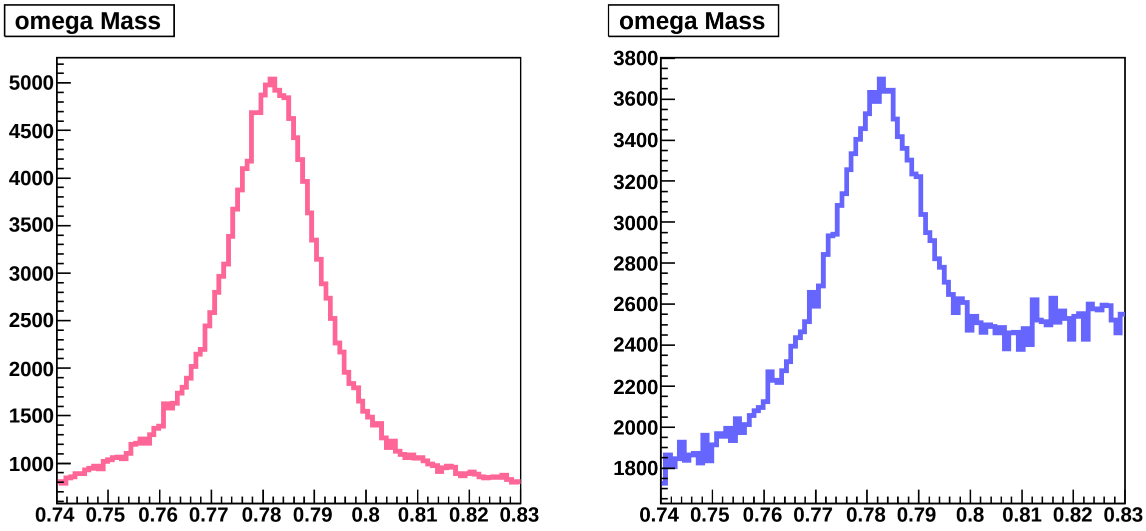

Figure 46: The invariant $\pi^+\pi^-\pi^0$ mass distributions for signal MC (left) and continuum MC (right). Note that the y-axis of the both plots are zero-suppressed; the continuum plot has a much larger non-ω component.

B.2 Dalitz plot of the ω

Other variables are constructed from the Dalitz plot of $\omega \to \pi^+\pi^-\pi^0$ decay. We use the two variables x and y defined as

$$x = \frac{T_- - T_+}{\sqrt{3}Q}, y = \frac{T_0}{Q}, Q = T_+ + T_- + T_0, \tag{58}$$

where T_+, T_- and T_0 are the kinetic energies of three daughter particles π^+, π^- and π^0, respectively.

Figure 47 shows the distribution of x and y for signal and continuum MC events. We calculate likelihoods $\mathcal{L}_{S(B)}$(Dalitz) from two dimensional histograms. The distribution for signal MC events represents the theoretical model of $J^P = 1^-$ particle decaying into tree $J^P = 0^-$ particles [61], which populate at (x, y)=(0,0). On the other hand, distribution of continuum is smeared due to random combination of pions.

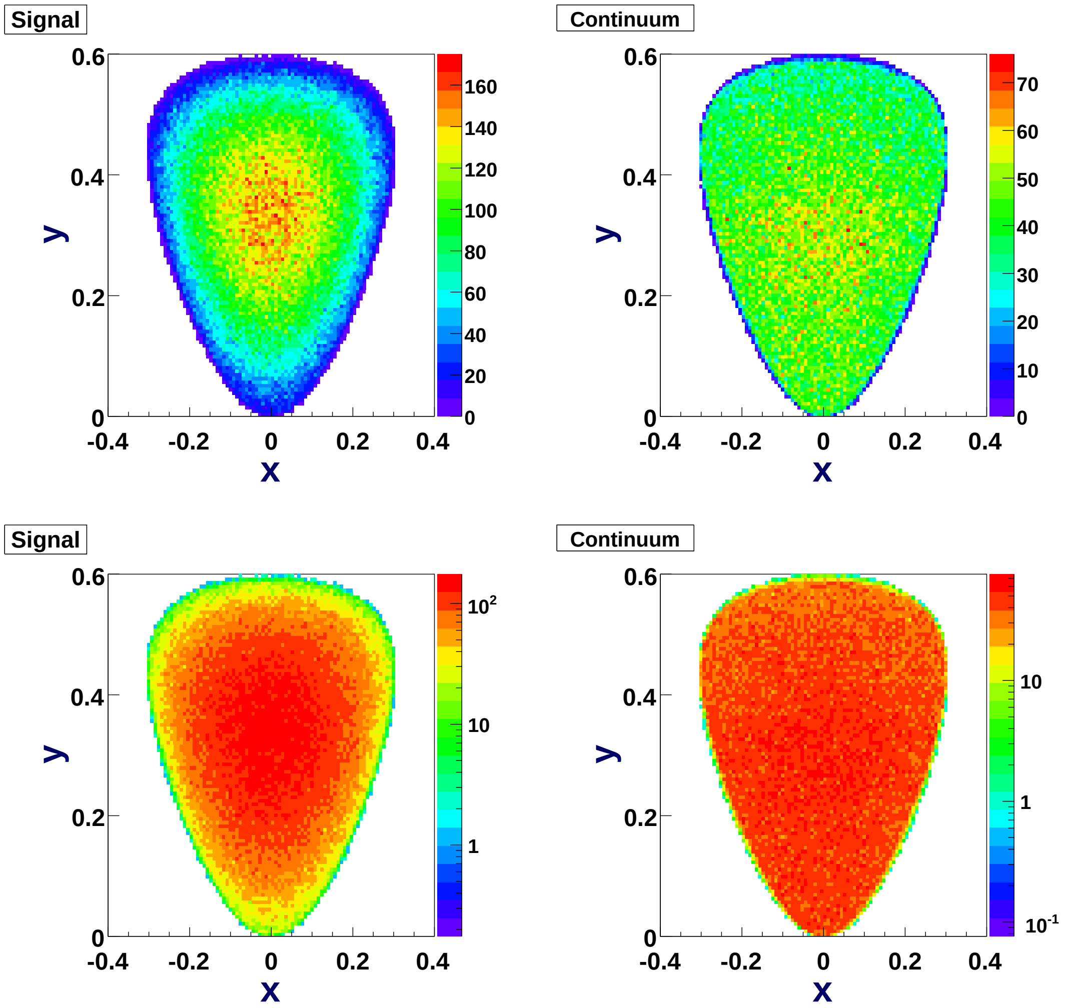

Figure 47: ω Dalitz plot distributions for signal MC (left) and continuum MC (right). Horizontal axis shows x and vertical axis shows y. Color codes are shown in linear (logarithmic) scale in the top (bottom) plots.

B.3 Improvements

We have tested the improvement of the new variables. We assume $\mathcal{B}(B^0 \to \omega\gamma) = 0.45 \times 10^{-6}$ and $\mathcal{R}$ requirements are optimized as description in 4.5 for 700 fb^{-1} data

Table 18: Improvement on $N_S/\sqrt{N_S+N_B}$ by using the $M_{\pi^+\pi^-\pi^0}$ and Dalitz variable.

	signal yield	continuum yield	$N_S/\sqrt{N_S+N_B}$
$\mathcal{R}(\text{KSFW}, \cos\theta^*_B(, \Delta z))$	16.1	32.5	2.31
$\mathcal{R}(\text{KSFW}, \cos\theta^*_B(, \Delta z), M_{\pi^+\pi^-\pi^0}, \text{Dalitz})$	16.3	29.6	2.41

with the signal and continuum components (no B background components). As shown in Table 18, there is a slight improvement.

C Helicity Angle

The θ_{hel} is defined as the angle between the daughter π^+ direction and the B meson direction in the ρ meson rest frame; for $B \to \omega\gamma$ events, θ_{hel} is defined as the angle between the normal to their decay plane and the B meson direction in the ω meson rest frame. In the decay $B \to \rho\gamma$, due to the photon polarization, ρ takes the spin state of $J = 1$ and $J_z = \pm 1$, where the direction of the photon is defined as the z axis in the B rest frame. The orbital angular momentum is $L = 1$ and $L_z = \pm 1$ in the decay $\rho \to \pi\pi$, because π is spinless. The angular momentum wave function ψ is $\psi = Y^1_1 \propto \sin\theta_{hel}$. The angular distribution of the decay is $|\psi|^2 = |Y^1_1|^2 \propto \sin^2\theta_{hel}$. On the other hand, in the decay $B \to \rho\pi^0, \rho\eta$, the helicity angle distribution follows $|Y^1_0|^2 \propto \cos^2\theta_{hel}$. Figure 48 shows the schematic drawing of the helicity angle for $\rho\gamma$ and $\rho\pi^0$, respectively.

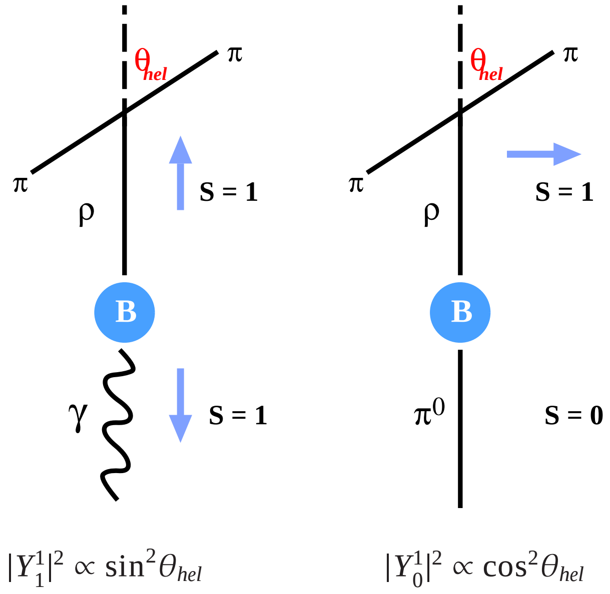

Figure 48: Schematic drawing of the helicity angle.

D Experiment-dependent photon energy shift

We study the effect of experiment-dependent photon energy shift recently reported in the Belle analysis [62]. According to this report, the measured photon energy is significantly shifted from exp. 33 (taken after January 2004 and corresponding to 446 fb^{-1}), causing a ΔE shift of +12 MeV during this period. We analyze $B^0 \to K^{*0}\gamma$ mode with data, dividing the sample into two parts, exp. 7 to 31 and exp 33 to 55. We fit the ΔE distribution with the signal , continuum background and B background components, floating the signal shape parameters (except α and n) We confirm the existence of the shift, with a somewhat different value of -6.7 ± 2.7 MeV. Therefore, we shift the ΔE value by -6.7 MeV in the data of exp 33 or later.

E Signal shape parameters

The procedures to determine the signal shape parameters are different in each mode. We first describe the way to determine ΔE parameters.

For $B^+ \to \rho^+\gamma$ and $B^0 \to \omega\gamma$, we first perform an one-dimensional fit to each of the ΔE distributions of the corresponding MC samples, and obtain (μ,σ,α,n) for each mode. We then fit again to each of the ΔE distribution with a Crystal Ball function with the fixed α and n to the previously determined value in order to obtain the values and errors of μ and σ. We take this procedure because parameters (α, n) are not very stable especially when more fit parameters and background events are included. Table 19 and Table 20 list the parameters of the ΔE and M_{bc} shapes determined with this procedure.

The next step is the calibration of these MC parameters with data using the $B \to K^*\gamma$ control samples. For $B^+ \to \rho^+\gamma$, we adopt the parameters determined from the $B^+ \to K^{*+}\gamma$ control sample except for the α and n parameters of the Crystal Ball function. For this purpose, we perform an two-dimensional (2D) fit to the ΔE and M_{bc} distributions of the $B^+ \to K^{*+}\gamma$ data samples, fixing α and n to the values determined from the $B^+ \to \rho^+\gamma$ MC samples. In the case of $B^0 \to \omega\gamma$, we fit both the data and MC of $B^+ \to K^{*+}\gamma$ with fixed α and n from the $B^0 \to \omega\gamma$ signal MC sample, and take the data/MC difference of μ as an additive correction factor and data/MC ratio of σ as a multiplicable correction factor. These sets of parameters are used in the nominal fit. Then, these are referred to as the "nominal" parameters hereafter.

In addition to these nominal parameters, we prepare other set of shape parameters, which we call "alternative", for the systematic study. We first fit the $K^{*+}\gamma$ data floating μ, σ and α of the ΔE and fixing n to the nominal value. We use thus obtained set of (n,α,μ,σ) as "alternative (1)". Since the values of n for the nominal and alternative (1) are the same, we prepare two more sets where the value of n is changed by $\pm 1\sigma_n$ (σ_n is the error of n). Here, the error of n is taken from the fit of the $K^{*0}\gamma$ data sample, the only sample with which a fit with floated n is successful. With these two new n, we fit the $K^{*+}\gamma$ ($B^0 \to \omega\gamma$ signal MC) to determine μ, σ and α for $B^+ \to \rho^+\gamma$ ($B^0 \to \omega\gamma$). These sets of parameters are denoted by "alternative (2)" and "alternative (3)".

On the other hand, for $B^0 \to \rho^0\gamma$, six signal shape parameters (μ,σ for M_{bc} and

Table 19: Shape parameters of the signal ΔE distributions in each step. A number in a bracket indicates that the corresponding parameter is fixed in the fit.

Sample	n	α	μ (MeV/c^2)	σ (MeV/c^2)	Comments
[ΔE] for $\omega\gamma$					
$\omega\gamma$ MC	$14.13^{+2.19}_{-1.84}$	0.50 ± 0.01	$-5.6^{+0.62}_{-0.82}$	$40.7^{+0.52}_{-0.46}$	two-step fit $\Leftarrow$
$K^{*+}\gamma$ MC	[14.13]	[0.50]	-7.0 ± 0.32	41.8 ± 0.22	(n, α) from $\omega\gamma$ MC
$K^{*+}\gamma$ data	[14.13]	[0.50]	1.4 ± 3.0	42.6 ± 2.1	(n, α) from $\omega\gamma$ MC
$K^{*+}\gamma$ data	[14.13]	$0.59^{+0.09}_{-0.07}$	$-3.4^{+4.8}_{-5.1}$	$46.5^{+4.0}_{-3.7}$	for alternative set (1)
$\omega\gamma$ MC	[14.13 − 2.03]	$0.51^{+0.009}_{-0.008}$	$-6.1^{+0.61}_{-0.66}$	$41.0^{+0.51}_{-0.47}$	for alternative set (2)
$\omega\gamma$ MC	[14.13 + 4.93]	0.28 ± 0.006	$-5.1^{+0.51}_{-0.53}$	$40.4^{+0.41}_{-0.40}$	for alternative set (3)
[ΔE] for $\rho^+\gamma$					
$\rho^+\gamma$ MC	$14.8^{+3.3}_{-2.2}$	$0.52^{+0.01}_{-0.02}$	-11.2 ± 0.3	44.7 ± 0.2	two-step fit $\Leftarrow$
$K^{*+}\gamma$ data	[14.8]	[0.52]	$0.1^{+2.9}_{-3.0}$	$43.7^{+2.2}_{-2.1}$	(n, α) from $\rho^+\gamma$ MC
$K^{*+}\gamma$ data	[14.8]	$0.58^{+0.09}_{-0.07}$	$-3.2^{+4.7}_{-5.2}$	$46.3^{+4.1}_{-3.5}$	for alternative set (1)
$K^{*+}\gamma$ data	[14.8 − 2.03]	$0.59^{+0.09}_{-0.07}$	$-3.5^{+4.8}_{-5.1}$	$46.5^{+4.0}_{-3.7}$	for alternative set (2)
$K^{*+}\gamma$ data	[14.8 + 4.93]	$0.57^{+0.08}_{-0.07}$	$-3.1^{+4.7}_{-5.1}$	$46.3^{+4.0}_{-3.6}$	for alternative set (3)
[ΔE] for $\rho^0\gamma$					
$K^{*0}\gamma$ data	$6.39^{+4.93}_{-2.03}$	$0.65^{+0.09}_{-0.08}$	4.1 ± 2.4	36.9 ± 1.8	all parameters are floated $\Leftarrow$
$K^{*0}\gamma$ data	[6.39 - 2.03]	0.73 ± 0.04	2.8 ± 1.8	37.7 ± 1.5	for alternative set (2)
$K^{*0}\gamma$ data	[6.39 + 4.93]	0.58 ± 0.04	5.4 ± 2.0	36.1 ± 1.6	for alternative set (3)

μ,σ,α,n for ΔE) are determined from the data sample of $B^0 \to K^{*0}\gamma$. To determine the parameters, we perform an 2D fit floating all the six parameters. We do not produce the alternative (1) set for $B^0 \to K^{*0}\gamma$ because α is already floated. The alternative(2)/(3) sets are prepared by redoing the fit with fixed n value shifted by -1/+1 σ.

Nominal shape parameters and their alternative sets for $M_{\rm bc}$ are generated with the same procedure except the following two points. When we vary n to produce alternative(2) or (3) set, we set n to be 1.16 or 5.83. These numbers are from n and its error in the fit to the control $B^+ \to K^{*+}\gamma$ data sample; the lower value corresponds to $n - \Delta n$, while the upper value is $n + 2(\Delta n)'$, where $(\Delta n)'$ is the parabolic error of the fit . The second point is that we do not have alternative sets for $B^0 \to K^{*0}\gamma$ because we use Gaussian for the signal shape.

Table 20: Shape parameters of the signal $M_{\rm bc}$ distributions in each step. A number in a bracket indicates that the corresponding parameter is fixed in the fit.

Sample	n	α	μ (MeV/c^2)	σ (MeV/c^2)	Comments
[$M_{\rm bc}$] for $\omega\gamma$					
$\omega\gamma$ MC	$2.13^{+0.10}_{-0.08}$	$1.64^{+0.02}_{-0.03}$	5279.40 ± 0.02	3.20 ± 0.01	two-step fit $\Leftarrow$
$K^{*+}\gamma$ MC	[2.13]	[1.64]	5278.96 ± 0.02	3.24 ± 0.01	(n, α) from $\omega\gamma$ MC
$K^{*+}\gamma$ data	[2.13]	[1.64]	5279.11 ± 0.14	$2.85^{+0.12}_{-0.11}$	(n, α) from $\omega\gamma$ MC
$K^{*+}\gamma$ data	[2.13]	$1.77^{+0.27}_{-0.20}$	5279.08 ± 0.14	2.88 ± 0.12	for alternative set (1)
$\omega\gamma$ MC	[1.16]	1.97 ± 0.01	5279.33 ± 0.02	3.26 ± 0.01	for alternative set (2)
$\omega\gamma$ MC	[12.0]	1.03 ± 0.01	5279.57 ± 0.02	3.10 ± 0.02	for alternative set (3)
[$M_{\rm bc}$] for $\rho^+\gamma$					
$\rho^+\gamma$ MC	$1.81^{+0.08}_{-0.10}$	$1.57^{+0.04}_{-0.03}$	5278.94 ± 0.02	3.43 ± 0.01	two-step fit $\Leftarrow$
$K^{*+}\gamma$ data	[1.81]	[1.57]	5279.13 ± 0.14	2.82 ± 0.12	(n, α) from $\rho^+\gamma$ MC
$K^{*+}\gamma$ data	[1.81]	$1.85^{+0.26}_{-0.19}$	5279.07 ± 0.14	2.88 ± 0.12	for alternative set (1)
$K^{*+}\gamma$ data	[1.16]	$2.08^{+0.25}_{-0.17}$	5279.06 ± 0.14	$2.89^{+0.12}_{-0.11}$	for alternative set (2)
$K^{*+}\gamma$ data	[6.74]	$1.41^{+0.30}_{-0.20}$	$5279.12^{+0.16}_{-0.15}$	2.84 ± 0.13	for alternative set (3)
[$M_{\rm bc}$] for $\rho^0\gamma$					
$K^{*0}\gamma$ data	—	—	5279.7 ± 0.06	2.63 ± 0.04	

Table 21: Bias study from the 2D PDF in the fit. Input and yield are from an ensemble test for 657×10^6 samples, ϵ bias is ratio of the yield determined from a fit to a large sample to the number of events in the sample, and ϵ corr. is the correction factor to the efficiency due to this bias.

mode	$M_{\rm bc}$ (GeV)	ΔE (GeV)	input	yield	ϵ bias	ϵ corr.
$B^+ \to \rho^+\gamma$	> 5.273	$[-0.1, 0.1]$	49.5	44.8	0.899	0.993
	> 5.27	$[-0.2, 0.1]$	49.5	47.5	0.942	0.982
	> 5.27	$[-0.3, 0.1]$	49.5	49.4	0.964	0.966 $\Leftarrow$
	> 5.20	$[-0.5, 0.5]$	49.5	52.4	1.020	0.963
correction						0.966 ± 0.027
$B^0 \to \omega\gamma$	> 5.273	$[-0.1, 0.1]$	20.6	19.9	0.932	0.965
	> 5.27	$[-0.2, 0.1]$	20.6	20.9	0.962	0.948
	> 5.27	$[-0.3, 0.1]$	20.6	21.1	0.974	0.951 $\Leftarrow$
	> 5.20	$[-0.5, 0.5]$	20.6	22.2	1.001	0.929
correction						0.951 ± 0.022

F Efficiency correction

F.1 Fit bias

F.1.1 2D fit

In order to study a possible bias in the 2D fitting procedure, we performed an ensemble test. We generate 1000 ensembles of simulated experiments that consist of $B^+ \to \rho^+\gamma$ ($B^0 \to \omega\gamma$) signal, $B^+ \to K^{*+}\gamma$ background (for $B^+ \to \rho^+\gamma$) , continuum and other B background events. For each experiment, number of the signal and background events are randomly generated according to a Poisson distribution whose mean is the expected number of events for their components. For each continuum event, a set of ($M_{\rm bc}, \Delta E$) is generated based on the PDF, while other background events are randomly extracted from the MC events.

We then perform a 2D fit for each experiment and extract the signal yield. We have varied the $M_{\rm bc}$ and ΔE windows, and for each of the windows we determine the signal PDF, calculated the efficiency with this PDF and perform an ensemble test. The efficiency from the fit is calculated using 10^4 signal events that pass the selection criteria and 10^5 continuum events generated from the PDF. The results are shown in Table 21. From the results, we decide to take the PDF determined from those determined with -0.3 GeV $< \Delta E < +0.1$ GeV and $M_{\rm bc} > 5.27$ GeV$/c^2$ and take the maximal difference in the correction factor to the efficiency as the systematic error.

Table 22: The fit bias on each M_{bc}-ΔE windows for $\rho^0\gamma$.

mode	M_{bc} (GeV)	ΔE (GeV)	ϵ bias.
$B^0 \to \rho^0\gamma$	> 5.273	$[-0.1, 0.1]$	0.967
	> 5.27	$[-0.2, 0.1]$	0.968
	> 5.27	$[-0.3, 0.1]$	0.968
	> 5.20	$[-0.5, 0.5]$	0.976 ⇐

F.1.2 3D fit

The efficiency is determined by fitting and have a bias depends on the M_{bc}-ΔE windows as shown in Table 22. The efficiency for the $\rho^0\gamma$ is determined with $|\Delta E| < 0.5$ GeV and $M_{\mathrm{bc}} > 5.20$ GeV/c^2. then, fit bias is 0.976.

For $\rho^+\gamma$ and $\omega\gamma$, the signal PDF is determined by signal MC. We then decide the correction factor to the efficiency as described in F.1.1.

In the $\rho^0\gamma$ case, the signal PDF is determined by the fitting to $K^{*0}\gamma$ data sample. To estimate the bias, we performed ensemble test in the same condition using the sample that consist of $K^{*0}\gamma$ signal MC and continuum MC event. For each continuum event, a set of $(M_{\mathrm{bc}}, \Delta E, M_{K\pi})$ is generated based on the PDF for continuum background, while other background events are randomly extracted from the MC events. We find the signal yield $N_{\rho^0\gamma} = 77.3$ for the input number 80.3 and the ratio is $77.3/80.3 = 0.9626$. The correction factor ($\epsilon_{cor.}$) is $\frac{0.976}{0.9626} = 1.014$.

For 3D fit to $B^0 \to \rho^0\gamma$, the fitting systematic error comes from

- M_{bc}-ΔE window, (See Table 22)
- difference between $K^{*0}\gamma$ and $\rho^0\gamma$, (This Section)
- Correlation of M_{bc}-ΔE and $M_{K\pi}$,

To estimate the systematic error from correlation between M_{bc}-ΔE and $M_{K\pi}$, we performed Ensemble test for the continuum event using MC. This test gives $N_{\rho^0\gamma} = 81.3 \pm 0.5$ for 80.3 signal event input. It seems the correlation between M_{bc}-ΔE and $M_{K\pi}$ is small. We take the maximal difference in the correction factor to the efficiency as the systematic error and obtain $\epsilon_{cor.} = 1.014 \pm 0.049$.

Table 23: Summary of corrections on the particle identification efficiencies.

SVD1		
Mode	corr. per track	total corr.
$B^+ \to K^{*+}\gamma$ fake	0.9820 ± 0.0708	0.9820 ± 0.0708
$B^0 \to K^{*0}\gamma$ fake	0.9568 ± 0.0717	0.9568 ± 0.0717
$B^+ \to K^{*+}\gamma$	1.0095 ± 0.0076 (K)	1.0095 ± 0.0076
$B^0 \to K^{*0}\gamma$	1.0105 ± 0.0076 (K)	
	0.9626 ± 0.0048 (π)	0.9727 ± 0.013
$B^+ \to \rho^+\gamma$	0.9481 ± 0.0048 (π)	0.9481 ± 0.0048
$B^0 \to \rho^0\gamma$	0.9489 ± 0.0048 (π)	0.9004 ± 0.0090
$B^0 \to \omega\gamma$	0.9633 ± 0.0053 (π)	0.9279 ± 0.0093
SVD2		
Mode	corr. per track	total corr.
$B^+ \to K^{*+}\gamma$ fake	1.0141 ± 0.0585	1.0141 ± 0.0585
$B^0 \to K^{*0}\gamma$ fake	0.9988 ± 0.0619	0.9988 ± 0.0619
$B^+ \to K^{*+}\gamma$	1.0013 ± 0.0068 (K)	1.0013 ± 0.0068
$B^0 \to K^{*0}\gamma$	1.0030 ± 0.0068 (K)	
	0.9539 ± 0.0046 (π)	0.95676 ± 0.0013
$B^+ \to \rho^+\gamma$	0.9389 ± 0.0045 (π)	0.9389 ± 0.0045
$B^0 \to \rho^0\gamma$	0.9393 ± 0.0045 (π)	0.88228 ± 0.0088
$B^0 \to \omega\gamma$	0.9515 ± 0.0054 (π)	0.90535 ± 0.0091

F.2 PID Efficiency

PID likelihood is based on MC samples using CDC, ACC and TOF information [63]. We use $D^{*+} \to D^0\pi^+(D^0 \to K^-\pi^+)$ decay for calibration of PID. The characteristic slow π^+ from the D^{*+} decay allows these decays to be selected with a good S/N ratio without relying on PID. We measure efficiency and mis-identification probability (fake rate) of kaon and pion and compare these results to MC expectation. We make a table of efficiency and fake rate for bins in momentum and pola angles in the laboratory system for data and MC samples. Then, a table of correction factors (ratio of data and MC efficiencies) is made. The correction factor is calculated according to the table for each charged track. We obtained total correction factor as product of these. The systematic error of PID efficiency is included in total systematic error.

Table23 shows the summary table of corrections on the PID efficiencies in this analysis.

G Efficiency Systematic

G.1 Tracking

The tracking efficiency is assessed comparing the number of partially and fully reconstructed D^* decays [64].

Partial reconstruction of the D^* meson The track finding efficiency for a given track can be determined whenever the track is unambiguously determined by other constraints. This is for instance the case in decays which can be reconstructed partially, using conservations laws to compensate for the non-usage of a given track. Three constraints are needed to compensate for three coordinates of the momentum (the mass of the missing particle is supposed to be known).

The used decay chain is $D^* \to \pi_{slow} D^0$, $D^0 \to \pi^+\pi^- K^0_S$ and $K^0_S \to \pi^+\pi^-$ where one of the pions from the K^0_S is ignored. The D^*, D^0 and K^0_S masses are the three needed constraints allowing to recover its momentum. The long lifetime of the K^0_S additionally allows to determine its direction of flight using the K^0_S and D decay vertex positions. Practically, we use this direction, the D^0 and the K^0_S masses to determine the momentum of the missing pion, while the D^* mass requirement is used to extract the signal-to-background (S/B) ratio. Note that in order to extract a meaningful track finding efficiency , we restrict to K^0_S decaying inside of the first SVD layer. In partial reconstruction, we can obtain the recovered 4-momentum of the missing pion. The momentum is required to point the acceptable region of the detector.

For every recovered track, we try to look for a track compatible with the recovered momentum. First we select the track which is closest in momentum space to the recovered momentum. If there is no such a track (which is very rare), the lost pion is considered to be not reconstructed. Then the K^0_S vertex position and all masses are recalculated using this track. Then we compare the partially reconstructed D^* mass with the fully reconstructed D^* mass. The total pion finding efficiency(ϵ_{Found}) is defined as

$$\epsilon_{Found} = \epsilon_{Track} \times \epsilon_{Cut} \tag{59}$$

where ϵ_{Track} and ϵ_{Cut} are the efficiency of the track finding and the selection cuts, respectively.

The track finding efficiency is given by the fraction of signal events which are found. From the distribution of the partially reconstructed D^* mass, we extract the number of events in the signal window S_{All} and fits the number of background events B_{fit}. The B_{fit} is calculated as the integral of the background fit to the partially reconstructed D^* mass.

The number of found events S_{Found} in the signal window is given by the distribution of the fully reconstructed D^*. The fraction ϵ^B_{Fit} of background events which are found is assumed to be constant over the whole mass range. The ϵ^B_{Fit} is calculated as the ratio between the number of all events and the number of found events with sideband of D^* mass.

We can then calculate the ratio of the number of found signal events and the total number of signal events:

$$\epsilon_{Found} = \frac{S_{found} - \epsilon^B_{Fit} B_{fit}}{S_{All} - B_{fit}} \tag{60}$$

We obtain the track finding efficiency ϵ_{Track} and then estimate systematic error from difference between data and MC.

$$r \equiv \frac{\epsilon^{Data}_{Track}}{\epsilon^{MC}_{Track}} - 1 = \frac{\epsilon^{Data}_{Found}}{\epsilon^{MC}_{Found}} \times \frac{\epsilon^{Data}_{Cut}}{\epsilon^{MC}_{Cut}} \qquad \left(r_{Cut} \equiv \frac{\epsilon^{Data}_{Cut}}{\epsilon^{MC}_{Cut}} \right) \tag{61}$$

$$r = \frac{83.84\% \pm 0.60}{84.16 \pm 0.35} \pm 0.20\% - 1 = (-0.35 \pm 0.82(\text{stat.}) \pm 0.20(\text{syst.}))\% \tag{62}$$

where the error includes the systematic error due to the r_{Cut}.

We thus assume that the track finding efficiencies are the same in data and MC, and provide a conservative error on this assumption.

$$\text{error} = (-0.35 \oplus 0.82 \oplus 0.20 = 0.91)\% \tag{63}$$

G.2 π^0 Detection Efficiency

We study the relative π^0 reconstruction efficiency between data and MC using $\eta \to \gamma\gamma$ and $\eta \to 3\pi^0$ decays [65]. The efficiency ratio of data and MC is obtained from

$$\frac{\epsilon_{data}(2\pi^0)}{\epsilon_{MC}(2\pi^0)} = \frac{N_{data}(\eta \to 3\pi^0)/N_{MC}(\eta \to 3\pi^0)}{N_{data}(\eta \to \gamma\gamma)/N_{MC}(\eta \to \gamma\gamma)} \tag{64}$$

where N is the signal yield. We assume $\epsilon_{data}(\pi^0 \to \gamma\gamma)/\epsilon_{MC}(\pi^0 \to \gamma\gamma) = \epsilon_{data}(\eta \to \gamma\gamma)/\epsilon_{MC}(\eta \to \gamma\gamma)$.

The single π^0 efficiency ratio can be determined by

$$\frac{\epsilon^{single}_{data}}{\epsilon^{single}_{MC}} = \sqrt{\frac{\epsilon_{data}(2\pi^0)}{\epsilon_{MC}(2\pi^0)}} \tag{65}$$

To obtain the signal yield, we perform a fit on the reconstructed η mass distribution from $\eta \to 3\pi^0$ and $\eta \to \gamma\gamma$. The photon energy is required to be greater than 50 MeV and the η's momentum is required to be greater than 2 GeV in the lab frame.

We calculate efficiency for MC and data sample and find the systematic error as

$$\delta(\epsilon^{single}_{data}/\epsilon^{single}_{MC}) = 4.6\% \tag{66}$$

G.3 Systematic error on the photon efficiency

The systematic error on the photon detection efficiency is estimated in Ref. [66]. However, this study only considered photons in the barrel region. Because we include endcap photons for the primary photon candidates in this analysis, we perform additional study to estimate a systematic error for the endcap photons.

We compare the yield ratio of the events with an endcap photon to those with a barrel photon between data and MC using the $B^0 \to K^{*0}\gamma$ control sample. Figure 49 shows the M_{bc} and ΔE distributions of data and MC for $B^0 \to K^{*0}\gamma$ with the high energy

Table 24: Comparison of the candidates with the barrel and endcap photon between 357 fb^{-1} data and MC.

	$B^+ \to \rho^+\gamma$		$B^0 \to \rho^0\gamma$		$B^0 \to \omega\gamma$	
	barrel	endcap	barrel	endcap	barrel	endcap
Data	179	19	75	9	27	3
MC	197.9	20.7	106.6	8.8	32.1	3.8

photon in the barrel and endcap regions. The MC distributions is a mixture of the signal $B^0 \to K^{*0}\gamma$ MC sample of 4×10^5 events and continuum events. Here, continuum events are generated from the PDFs with the normalization scaled to the S/N of the data fit.

We perform a 2D fit to obtain the signal yields in each sample. The fit is performed with the signal, continuum, $B \to X_s\gamma$ and rare B decay components for data samples, and with the signal and continuum components for MC samples. Normalization and shape parameters for the signal and continuum components are floated except α and n of the signal ΔE PDF. We obtain 2393 ± 52 and 223 ± 16, respectively for the barrel and endcap region for data, and 40595 ± 213 and 3358 ± 63 for MC.

We then compare $f = y_{\mathrm{data}}/(y_{\mathrm{MC}} \times \eta_{\mathrm{PID}})$ between barrel and endcap, where y_{data} and y_{MC} are the signal yields for data and MC, and η_{PID} is a PID correction factor. Using $\eta_{\mathrm{PID}}^{\mathrm{barrel}} = 0.957$ and $\eta_{\mathrm{PID}}^{\mathrm{endcap}} = 0.949$ calculated from MC and PID correction tables described in Appendix F.2, we obtain $f^{(\mathrm{barrel})} = (6.16 \pm 0.14) \times 10^{-2}$ and $f^{(\mathrm{endcap})} = (6.69 \pm 0.49) \times 10^{-2}$, resulting $f^{(\mathrm{endcap})}/f^{(\mathrm{barrel})} = 1.086 \pm 0.084$.

Because the photon detection efficiency in the barrel region between data and MC agrees within error, we consider the discrepancy as an additional systematic error in the endcap photon detection. Taking a quadratic sum of the deviation from unity and the error, the systematic error of the endcap photon detection is calculated to be 12.0%. Considering that 8.5% of all photons are found in the endcap, the overall effect to the photon efficiency is 1.0%. Then, the total photon detection systematic efficiency is calculated to be 2.4% including the 2.2% error from Ref. [66].

For reference, we count the candidates in the signal region with endcap and barrel photon with the 357 fb^{-1} dataset, and make a comparison with the MC expectations for the sum of the signal and backgrounds as given in Table 24.

G.4 Systematic error study using $B \to D\pi$

The systematic error on the combined efficiency for the π^0/η veto condition and the flavor-tagging dependent likelihood ratio criteria is evaluated using $B \to D\pi$ modes. We use $B^0 \to D^-\pi^+$ with $D^- \to K^+\pi^-\pi^-$ to study the systematic error for $B^0 \to \rho^0\gamma$, $B^+ \to \overline{D}^0\pi^+$ with $\overline{D}^0 \to K^+\pi^-$ for $B^+ \to \rho^+\gamma$, and $B^+ \to \overline{D}^0\pi^+$ with $\overline{D}^0 \to K_s\omega$ for $B^0 \to \omega\gamma$. We select D^+ and D^0 in the invariant mass range between 1.86 and 1.88 GeV/c^2; other selection criteria are similar to the $B \to \rho\gamma$, $B \to \omega\gamma$ analysis except for the $\cos\theta_{\mathrm{hel}}$ selection. We analyze the data and MC events taken from the full-reconstruction

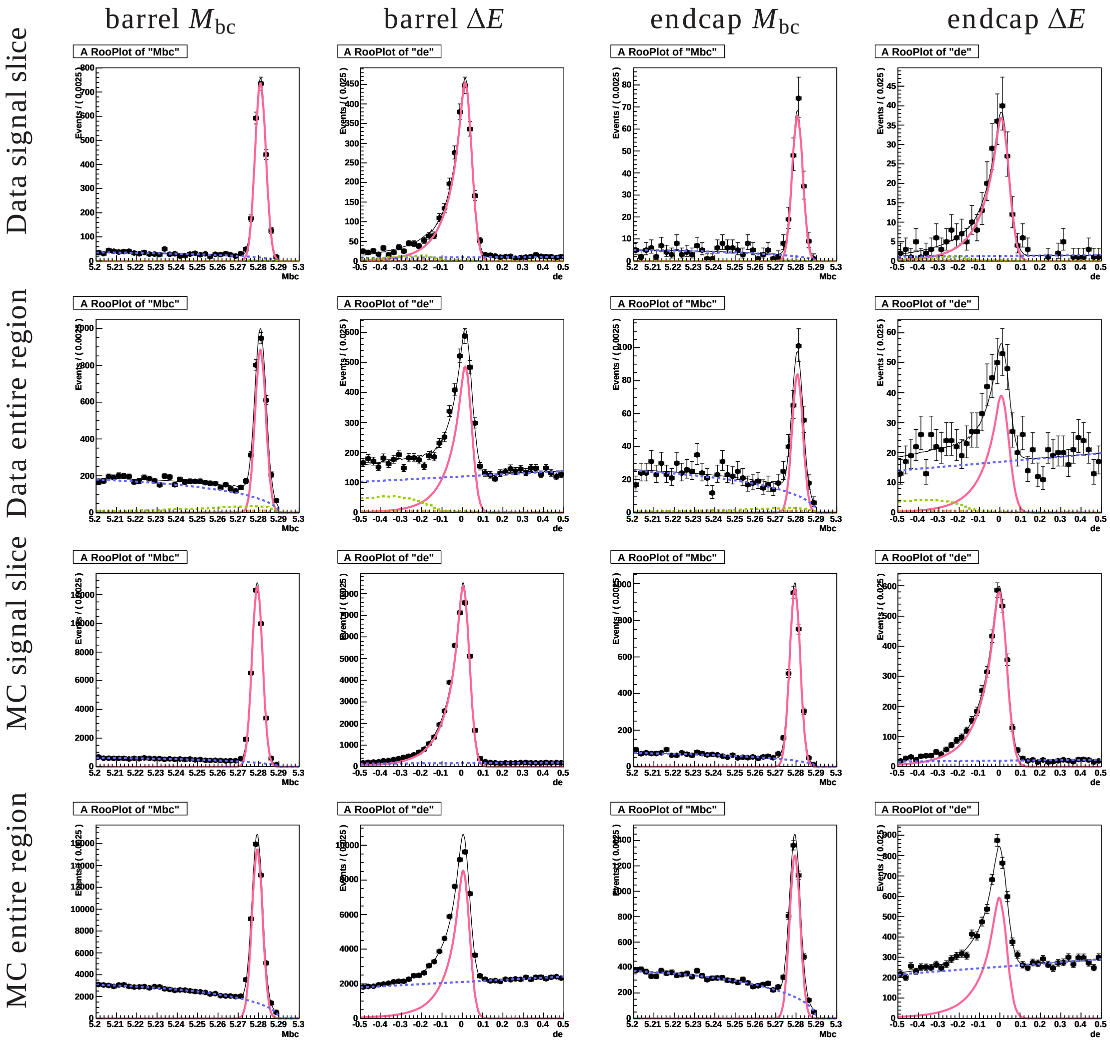

Figure 49: Fit results on the $B^0 \to K^{*0}\gamma$ control sample for the endcap photon efficiency study. Figures are arranged from the top to bottom for the signal region of data, entire slice of data, signal region of MC, and the entire slice of data; from left to right for the $M_{\rm bc}$ of the barrel events, ΔE of the barrel events, $M_{\rm bc}$ of the endcap events, and ΔE of the endcap events. Curves are the fit results. (black solid for total, red solid for signal, blue dotted for continuum, and yellow-green for rare B decays.)

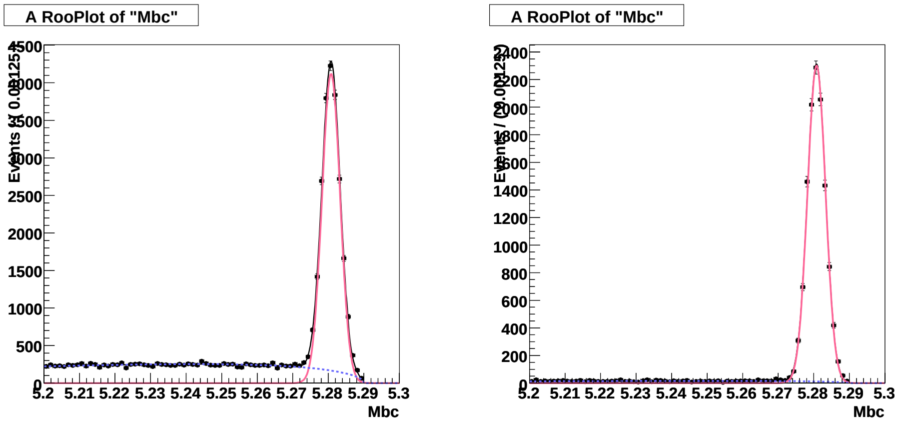

Figure 50: M_{bc} distributions of the $\overline{B}^0 \to D^+\pi^-$ data sample for the systematic study of $B^0 \to \rho^0\gamma$. The left (right) plot shows the distribution without (with) the $q \cdot r$ dependent likelihood ratio and the π^0/η veto criteria.

sample[4] and extract the signal yields from M_{bc} fits for the events with and without the set of requirements to calculate efficiencies. When we apply the π^0/η veto condition to $B \to D\pi$ samples, we calculate the π^0 or η probability regarding the primary pion as a high energy photon (chargeless massless particle).

In the calculation of KSFW, we set the USE_FINALSTATE_FOR_SIG option to 1. This is an option whether to use the final state particles (in the $B^+ \to \rho^+\omega$ case, use $\pi^+\gamma\gamma\pi^+\pi^-\gamma\gamma$) or not (use ρ^+ and ω directly). This option seems to cause a mode-dependent shift in the KSFW distribution. Therefore, for the $B \to D\pi$ samples, we use the same coefficients of Fisher discriminants for KSFW as those in $B^0 \to \rho^0\gamma$, $B^- \to \rho^-\gamma$ and $B^0 \to \omega\gamma$, but recalculate the likelihood distributions $\mathcal{L}_{S(B)}$(KSFW). We use the full-reconstruction sample from generic $B\overline{B}$ MC and continuum MC, respectively for $\mathcal{L}_S$(KSFW) and $\mathcal{L}_B$(KSFW).

We fit the M_{bc} distribution to calculate the signal yield. Figure 50 shows the M_{bc} distributions for data for $B^- \to D^0\pi^-$ with and without the π^0/η veto condition and r-dependent likelihood ratio criteria. The result is summarized in Table 25.

H Systematic error using $B \to D\pi$ for the A_{CP} $B^+ \to \rho^+\gamma$

For the CP asymmetry systematic error, we performed the simultaneous fit to M_{bc} floating the parameters of $A_{CP}(B^+ \to D^0\pi^+)$ as a control sample. We treat the fast pion as the photon in $B^+ \to \rho^+\gamma$. The total systematic error includes the $A_{CP}(B^+ \to D^0\pi^+)$ as possible detector bias. The essential A_{CP} in $B^+ \to D^0\pi^+$ is small [48]. The result $A_{CP}(B^+ \to D^0\pi^+) = -0.018 \pm 0.011$ is obtained. The quadratic sum of the deviation and the statistical error is included in the total systematic error for the $A_{CP}(B^+ \to \rho^+\gamma)$.

---

[4] A sample where one of B-meson pair is fully reconstructed, which is used for analysis of the other B decays (full-reconstruction tag method).

Table 25: Summary of the $D\pi$ systematic study. Cut efficiencies for the $B \to \rho\gamma$, $B \to \omega\gamma$ signal MC are also listed for reference.

	$B^0 \to \rho^0\gamma$	$B^+ \to \rho^+\gamma$	$B^0 \to \omega\gamma$
$D\pi$ data yield before the cut	$(2.99 \pm 0.02) \times 10^4$	$(1.41 \pm 0.01) \times 10^4$	$(0.79 \pm 0.03) \times 10^3$
$D\pi$ data yield after the cut	$(1.57 \pm 0.01) \times 10^4$	$(0.41 \pm 0.01) \times 10^4$	$(0.23 \pm 0.02) \times 10^3$
$D\pi$ MC yield before the cut	$(3.77 \pm 0.02) \times 10^4$	$(1.77 \pm 0.01) \times 10^4$	$(3.25 \pm 0.06) \times 10^3$
$D\pi$ MC yield after the cut	$(2.01 \pm 0.01) \times 10^4$	$(0.53 \pm 0.01) \times 10^4$	$(1.01 \pm 0.03) \times 10^3$
Cut eff. for $D\pi$ data (%)	52.5 ± 0.29	29.5 ± 0.38	29.0 ± 1.62
Cut eff. for $D\pi$ MC (%)	53.5 ± 0.26	30.1 ± 0.34	30.9 ± 0.81
Cut eff. for signal MC (%)	51	35	43
Data/MC ratio	0.982 ± 0.007	0.980 ± 0.017	0.939 ± 0.058
Systematic error (%)	2.3	3.1	8.4

Figure 51 shows the M_{bc} distributions of data for $B \to D\pi$ with the plus charge B^+ and the minus charge B^- .

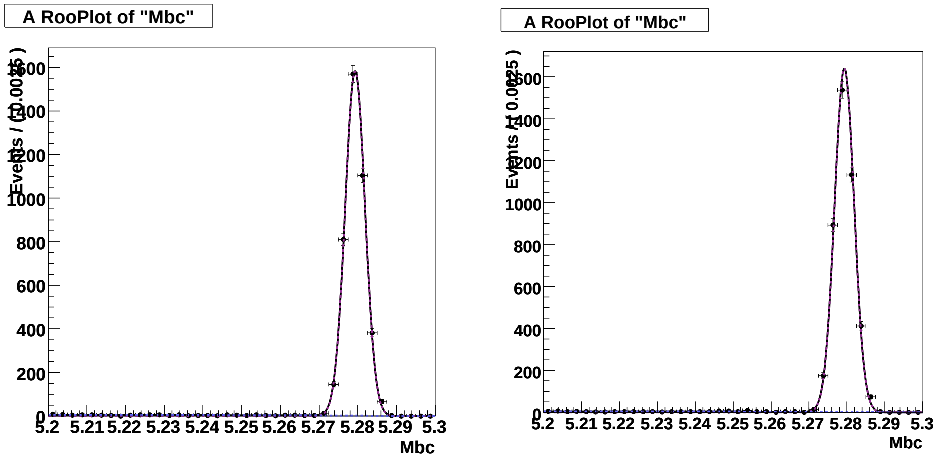

Figure 51: M_{bc} distributions of the $B^+ \to D^0\pi^+$ data sample for systematic study of $A_{CP}(B^+ \to \rho^+\gamma)$. The left(right) plot shows the distribution of the $B^{+(-)} \to D^0\pi^{+(-)}$.

I Constraint on $|V_{td}/V_{ts}|$

The ratio of branching fraction (R) is often parametrized as

$$R = \left|\frac{V_{td}}{V_{ts}}\right|^2 \left(\frac{1 - m_\rho^2/m_B^2}{1 - m_{K^*}^2/m_B^2}\right)^3 \frac{1}{\xi^2}[1 + \Delta R], \tag{67}$$

where ξ is due to the form factor ratio and ΔR is relevant to the isospin violation. It has been discussed in Ref. [6] that ΔR is not a simple number, but rather a complicated function of other CKM matrix elements. Here, instead of using Eq. 67, we use a numerical evaluation given in Ref. [6],

$$R = \left|\frac{V_{td}}{V_{ts}}\right|^2 [0.75 \pm 0.11(\xi) \pm 0.03(a_7^{u,c}, \phi_3, R_b)]. \tag{68}$$

where the first error is due to the form factor and second is due to the CKM elements and other short distance corrections. The form factor correction factor is

$$\xi = 1.17 \pm 0.09. \tag{69}$$

The isospin breaking term is derived in Ref. [6] to be

$$\begin{aligned} 1 + \Delta R \quad &= \quad \left|\frac{a_{7L}^c(\rho)}{a_{7L}^c(K^*)}\right|^2 \left(1 + \mathrm{Re}(\delta a_\pm + \delta a_0)\left[\frac{R_b^2 - R_b \cos\phi_3}{1 - 2R_b\cos\phi_3 + R_b^2}\right]\right. \\ &\quad \left. + \frac{1}{2}(|\delta a_0|^2 + |\delta a_\pm|^2)\left[\frac{R_b^2}{1 - 2R_b\cos\phi_3 + R_b^2}\right]\right) \end{aligned} \tag{70}$$

where

$$R_b = \left(1 + \frac{\lambda^2}{2}\right)\frac{1}{\lambda}\left|\frac{V_{ub}}{V_{cb}}\right|. \tag{71}$$

(For the definition of other symbols, please refer to Ref. [6].) The evaluation is based on a slightly old world averages,

$$|V_{ub}/V_{cb}| = 0.106 \pm 0.008 \quad \text{(from HFAG)[55]} \tag{72}$$

$$\phi_3 = (71 \pm 16)^\circ \quad \text{(from UTfit)[58]} \tag{73}$$

which gives

$$\begin{aligned} \frac{R_b^2 - R_b\cos\phi_3}{1 - 2R_b\cos\phi_3 + R_b^2} &= 0.07 \pm 0.12, \\ \frac{R_b^2}{1 - 2R_b\cos\phi_3 + R_b^2} &= 0.23 \pm 0.07. \end{aligned} \tag{74}$$

We extract $|V_{td}/V_{ts}|$ from Eq. (68) and the ratio of the branching fractions taken from Eq. (46). The statistical error and systematic errors are added in quadrature (denoted as the experimental error) and assumed to follow a Gaussian distribution. For the theory parameters, we take quadratic sum of errors of Eq. (68) and propagate the error in calculation. The result is

$$|V_{td}/V_{ts}| = 0.195\,^{+0.020}_{-0.019} \pm 0.015, \tag{75}$$

where the first and second errors are experimental and theoretical, respectively. The ratios from Eqs. (44) and (45) give following values,

$$|V_{td}/V_{ts}|_{(B^0\to\rho^0\gamma/B^0\to K^{*0}\gamma)} = 0.243\,^{+0.028}_{-0.027} \pm 0.018, \tag{76}$$
$$|V_{td}/V_{ts}|_{(B\to\rho\gamma/B\to K^{*}\gamma)} = 0.201 \pm 0.021 \pm 0.015, \tag{77}$$

where the first and second errors are experimental and theoretical, respectively.

References

[1] M. Kobayashi and T. Maskawa, Prog. Theor. Phys. **49**, 652 (1973); N. Cabibbo, Phys. Rev. Lett. **10**, 531 (1963).

[2] L. Wolfenstein, Phys. Rev. Lett. **51**, 1945 (1983).

[3] M. Misiak *et al.*, Phys. Rev. Lett. **98**, 022002 (2007), For other NNLO calculations, see e.g., T. Becher, M. Neubert, Phys. Rev. Lett. **98**, 022003 (2007), J.R. Andersen, E. Gardi, JHEP 0701:029 (2007).

[4] Belle Collaboration, K. Abe *et al.*, arXiv:0804.1580[hep-ex].

[5] Heavy Flavor Averaging Group, winter 2008 results, (http://www.slac.stanford.edu/xorg/hfag/).

[6] P. Ball, G.W. Jones, and R. Zwicky, J. High Energy Phys. 04 (2006) 046; P. Ball, G.W. Jones, and R. Zwicky, Phys. Rev. D **75**, 054004 (2007).

[7] A. Ali and A. Parkhomenko, Eur. Phys. J. C **23**, 89 (2002).

[8] T. Hurth, E. Lunghi, W. Porod, Nucl. Phys. B **704**, 56 (2005).

[9] Belle Collaboration, D. Mohapatra *et al.*, Phys. Rev. Lett. **96**, 221601 (2006).

[10] Babar Collaboration, B. Aubert *et al.*, Phys. Rev. Lett. **98**, 151802 (2007).

[11] M. Beneke, G. Buchalla, M. Neubert and C.T. Sachrajda, Phys. Rev. Lett. **83**, 1914 (1999); Nucl. Phys. B **591**, 313 (2000).

[12] M. Beneke and T. Feldmann, Nucl. Phys. B **592**, 3 (2001).

[13] M. Beneke, T. Feldmann and D. Seidel, Eur. Phys. J. C **41**, 173 (2005).

[14] P. Ball and V.M. Braun, Phys. Rev. D **58**, 094016 (1998).

[15] P. Ball and E. Kou, J. High Energy Phys. 04 (2003) 029.

[16] P. Ball and R. Zwicky, Phys. Lett. B **642**, 478 (2006).

[17] Y.Y. Keum, M. Matsumori and A.I. Sanda, Phys. Rev. D **72**, 014013 (2005).

[18] C.D. Lu, M. Matsumori, A.I. Sanda and M.Z. Yang, Phys. Rev. D **72**, 094005 (2005); [Erratum-ibid, D **73**, 039902 (2006)].

[19] A. Ali and A. Parkhomenko, (2006), hep-ph/0610149.

[20] S. Bosch and G. Buchalla, Nucl. Phys. B **621**, 459 (2002); See updated calculations in S. Bosch and G. Buchalla, JHEP, 051:035, (2005).

[21] B. Garinstein and D. Pirjol, Phys. Rev. D **62**, 093002 (2000).

[22] Z.-J. Xiao and C. Zhuang, Eur. Phys. J. C **33**, 349 (2004).

[23] X.D. Lu, M. Matsumori, A.I. Sanda and M.Z. Yang, Phys. Rev. D **72**, 094005 (2005). [Erratum-ibid. D **73**, 039902 (2006)] [arXiv:hep-ph/0508300].

[24] Y.D. Yang, Eur. Phys. J. C **36**, 97 (2004).

[25] G. Lu, R. Wang and Y.D. Yang, Eur. Phys. J. C **34**, 291 (2004).

[26] Babar Collaboration, B. Aubert *et al.*, Phys. Rev. D **72**, 091103 (2005).

[27] Babar Collaboration, B. Aubert *et al.*, Phys. Rev. D **70**, 091104 (2004).

[28] M. Ciuchini, G. Degrassi, P. Gambino, Nucl. Phys. B **534**, 3 (1998).

[29] A. Ali, E. Lunghi, Eur. Phys. J. C **21**, 683 (2001).

[30] A. Ali, E. Lunghi, Eur. Phys. J. C **26**, 195 (2002).

[31] S. Kurokawa and E. Kikutani, Nucl. Instrum. Meth. A **499**, 1 (2003), and other papers included in this Volume.

[32] Belle Collaboration, A. Abashian *et al.*, Nucl. Instrum. Meth. A **479**, 117 (2002).

[33] E. Nygard, P. Aspell, P. Jarron, P. Weilhammer, K. Yoshioka, Nucl. Instrum. Meth. A **301**, 506 (1991); O. Toker, S. Masciocchi, E. Nygard, A. Rudge, P. Weilhammer, Nucl. Instrum. Meth. A **340**, 572 (1994).

[34] M. Yokoyama *et al.*, IEEE Trans.Nucl.Sci.**48**,440,(2001).

[35] Y. Ushiroda *et al.*, Nucl. Instrum. Meth. A **511**, 6 (2003); Belle SVD2 Group, Z. Natkaniec *et al.*, Nucl. Instrum. Meth. A **560**, 1 (2006).

[36] H. Hirano *et al.*, Nucl. Instrum. Meth. A **455**, 294 (2000).

[37] T. Iijima *et al.*, Nucl. Instrum. Meth. A **453**, 321 (2000).

[38] T. Iijima *et al.*, Nucl. Instrum. Meth. A **379**, 457 (1996).

[39] H. Kichimi *et al.*, Nucl. Instrum. Meth. A **453**, 315 (2000).

[40] K. Miyabayashi *et al.*, Nucl. Instrum. Meth. A **494**, 298 (2002).

[41] A. Abashian *et al.*, Nucl. Instrum. Meth. A **491**, 69 (2002).

[42] K. Abe *et al.*, Nucl. Instrum. Meth. A **455**, 397 (2000).

[43] K.C. Peng *et al.*, Nucl. Instrum. Meth. A **427**, 524 (1999).

[44] Y. Makita *et al.*, Adv. Cryog. Eng **37**,401 (1992); Adv. Cryog. Eng **43A**,221 (1998).

[45] Belle Collaboration, Belle Technical Design Report, KEK Preprint 95-1 (1995).

[46] Y. Ushiroda *et al.*, Nucl. Instrum. Meth. A **438**, 460 (1999).

[47] S.Y. Suzuki, M. Yamauchi, M. Nakao, R. Itoh and H. Fujii, Nucl. Instrum. Meth. A **453**, 440 (2000).

[48] W.-M. Yao *et al.*, J. Phys. G **33**, 1 (2006).

[49] H.-U. Bengtsson, Computer Physics Commun. **31** (1984) 323;
H.-U. Bengtsson and G. Ingelman, Computer Physics Commun. **34** (1985) 251;
H.-U. Bengtsson and T. Sjöstrand, Computer Physics Commun. **46** (1987) 43;
T. Sjöstrand, Computer Physics Commun. **82** (1994) 74.

[50] A.L. Kagan and M. Neubert, Eur. Phys. J. C **7**, 5 (1999).

[51] G.C. Fox and S. Wolfram, Phys. Rev. Lett. **41**, 1581 (1978).

[52] Belle Collaboration, S.H. Lee *et al.*, Phys. Rev. Lett. **91**, 261801 (2003).

[53] Belle Collaboration, K. Abe *et al.*, Phys. Lett. B **511**, 151 (2001).

[54] H. Kakuno *et al.*, Nucl. Instrum. Meth. A **533**, 516 (2004).

[55] E. Barberio *et al.*, arXiv:0704.3575, Heavy Flavor Averaging Group, winter 2006 results,
(http://www.slac.stanford.edu/xorg/hfag/).

[56] Crystal Ball Collaboration, J. E. Gaiser *et al.*, Phys. Rev. D **34**, 711 (1986).

[57] ARGUS Collaboration, H. Albrecht *et al.*, Phys. Lett. B **241**, 278 (1990).

[58] UTfit Collaboration, M. Bona *et al.*, arXiv:0707.0636 [hep-ph].

[59] CDF - Run II Collaboration, A, Abulenia *et al.*, Phys. Rev. Lett. **97**, 062003 (2006).

[60] Y. Ushiroda, K. Sumisawa, N. Taniguchi *et al.*. (The Belle collaboration), Phys. Rev. Lett. **100**, 021602 (2008).

[61] M.L. Stevenson, L.W. Alvarez, B.C. Maglic, and A.H. Rosenfeld. Phys. Rev. **125**, 687 (1962).

[62] Y. Ushiroda, Belle Note 946, "Time-Dependent *CP* Asymmetry in $B^0 \to K_S^0\pi^0$ transitions".

[63] `http://belle.kek.jp/group/pid_joint`.

[64] P. Koppenburg, Belle Note 621, "A Measurement of the Track Finding Efficiency Using Partially Reconstructed D* Decays," (2003).

[65] S. W. Lin, P. Chang and H. C. Hwang, Belle Note 645, "Update of π^0 Systematics Using Inclusive η (78/fb)," (2003).

[66] H-W. Kim, Belle Note 499, "Study of High Energy Photon Detection Efficiency Using Radiative Bhabha," (2002).